Single Molecule Localization Microscopy reveals DNA compaction and nascent RNA structure in vivo.

Àlvaro Castells García

TESI DOCTORAL UPF / 2019

Thesis supervisor

Dr. Maria Pia Cosma

Gene Regulation, Stem Cells and Cancer Department

CENTER FOR GENOMIC REGULATION (CRG)
BARCELONA

To my parents. To Esther.

ACKNOWLEDGEMENTS

The acknowledgements should always be written in a hurry a few hours before printing the thesis. It is part of the charm. Today is one of the biggest milestones of a long, long journey. So many people, so many experiences. It has been one hell of a rollercoaster, with some of the most fulfilling and the hardest moments of my life.

I want to thank my supervisor, Pia Cosma, for her support and for giving me the possibility to do my PhD project in super-resolution. She accepted me in the lab, encouraged me in the RNA project and believed in me. Thanks for all the opportunities, the patience and the trust.

Thanks to all the Cosm@s, past and present. The lab has changed enormously since I entered, but every person here has been part of my life for the last four years, sharing experiences, good and bad.

Among the people in the lab, I have to give special thanks to Vicky. I think no two people can be more different than her and me, but regardless of that she has been a constant source of feedback, help, inspiration and encouragement during my thesis. She is one of the most intelligent, hardworking people I have had the pleasure to work with. I feel I owe her a great deal about all that I have learnt as a scientist during my PhD. Many thanks too to Chiara, she was a lifesaver when the project was adrift, and her contagious optimism helped me enormously in the last months.

From the now extinct AFIB group, I want to thanks Melike and Jason, for the enormous amount of technical knowledge they passed onto me, and for the enormous amounts of hours trying fluorophores while listening to power metal.

Thanks to the “Coffee brigade”. Pauli, Jose Luis and Javier. All the people that have had the time to unwind a little bit on the middle of the day, without whom the life at the CRG would have been way more uneventful and dull. You were the sliver of light

on many hard days. Thanks specially to Javier for listening to all my ramblings and introducing me to the ACEA. Thanks to you I discovered a hobby I didn't know I needed. Thanks as well to all the people of the ACEA for their warmth and kindness.

Thanks to Pol and Pauli for the trips, the beers and the support.

Thanks to Hikaru and German, the first roommates with whom this adventure began. It is a pity you had to go away and stop our "Tupper club".

I want to give special thanks to Esther. She has always been with me, every step of the way. She has been supporting, understanding and my support pillar when I needed her. I have shared with you my struggle, my frustration and my joys. I would not have been able to do this without you.

And finally, thanks from the bottom of my heart to Olga and Cristobal, my parents. They have always helped and supported me, encouraged my interest, and I wouldn't be who I am today without them. They are the best parents one could hope for.

THESIS ABSTRACT

Chromatin organization and gene expression are interdependent. Previously, our group showed that nucleosomes form groups, termed clutches, whose size correlates with cell state.

In this thesis, we carried out 3D, 2-color super-resolution microscopy to image core histones, DNA and RNA at nanoscale resolution. We identified the “clutch DNA” as the DNA whose compaction is dependent on the clutch. Moreover, we studied how the epigenetic state of the clutch alters the radius of the clutch DNA. We also identified nanodomains of nascent RNA, how they fall within the clutch DNA radius, and how their RNA density is inversely correlated to clutch size.

These results provide novel insights into chromatin organization at the nanoscale level and show how the clutches affect DNA packaging and transcriptional activity.

RESUMEN DE LA TESIS

La organización de la cromatina y la expresión génica son interdependientes. Previamente, nuestro grupo mostró que los nucleosomas forman grupos llamados "*clutches*", cuyo tamaño está correlacionado con el estado celular.

En esta tesis, se llevó a cabo microscopía de súper resolución en 3D y dos colores para poder obtener imágenes de histonas, ADN y ARN a una resolución nanoscópica. Se identificó el "*clutch DNA*" como aquel ADN cuya compactación es dependiente del "*clutch*". Además, se estudió como el estado epigenético de los "clutches" altera el radio del "clutch DNA". Se identificaron también nanodominios de ARN naciente, cuál es su ubicación dentro del radio del "clutch DNA", y como la densidad de ARN está inversamente correlacionada con el tamaño del "clutch".

Estos resultados proporcionan nuevas perspectivas en la organización de la cromatina a escala nanométrica, y muestran como los clutches afectan tanto el empaquetamiento de ADN como la actividad transcripcional.

RESUM DE LA TESI

L'organització de la cromatina i l'expressió gènica són interdependents. Prèviament, el nostre grup va mostrar que els nucleosomes estan formats per grups anomenats "clutches", la mida dels quals està correlacionada amb l'estat cel.lular.

En aquesta tesis, es dugué a terme microscopía de super resolució en 3D i dos colors per poder obtindre imatges d'histones, ADN i ARN en una resolució nanoscòpica. S'identificà el "clutch" DNA" com aquell ADN la compactació del qual és dependent del "clutch". A més a més, s'estudià com l'estat epigenètic dels "clutches" altera el radi del "clutch DNA".

S'identificaren també nanodominis d'ARN naixent, quina és la seva ubicació dins del radi del "clutch DNA", i com la densitat de ARN està inversament correlacionada amb el tamany del "clutch".

Aquests resultats proporcionen noves perspectives en l'organització de la cromatina a escala nanomètrica, i mostren com els "clutches" afecten tant l'empaquetament de l'ADN com l'activitat transcripcional.

PREFACE: IMAGING THE NUCLEUS

The history of biology is the history of observing life and its components. A great share of the processes of life occurs at a scale that cannot be observed by the naked eye. As such, the eagerness to gain new knowledge about these processes goes in hand with the need to develop new techniques and methods to do so.

Microscopy has been one fundamental method in the arsenal of the biologists since its inception in the XVII century. In the last century, new developments such as immunochemistry and confocal imaging have allowed us to image single cells with a clarity and specificity previously undreamed of.

Even then, light microscopy has always had an intrinsically physical limit, as determined in the Nyquist-Shannon sampling theorem: "when sampling a signal, the sampling frequency must be greater than twice the band width of the input signal in order to be able to reconstruct the original from the sampled version". There is a limit in the resolution at which an image can be obtained, independently from the quality of the elements of our optical system. Due to the range of wavelengths commonly used for light microscopy, the resolution limit is usually rounded to 200 nm.

Nevertheless, through the last decade new methods that are able to surmount this optical resolution limit have been developed. These methods, albeit really different in their various approaches, receive the placeholder name of “Super-Resolution Microscopy”, or “nanoscopy”.

Although the targets of the application of these new techniques have been many and varied, we are particularly interested in applying them to unveil the processes occurring in the cell

nucleus, especially those related with nuclear architecture and genome physical distribution.

The nucleus is considered to be the first cell organelle described. In 1719, Leeuwenhoek observed a “lumen” in red blood cells of salmon. Since it became clear that it hosted the genetic material, the way its organization determines its function has been one of the big questions of biology. In this project, we have used new imaging techniques to obtain more information about the structure and distribution of the genetic material in the nucleus.

Table of Contents

PART I: INTRODUCTION

1. NEW DEVELOPMENTS IN MICROSCOPY

In the last decades, two big developments have improved the quality and versatility of the microscopy techniques. One of this has been the immunochemistry (Coons and Kaplan, 1950). This endowed the researchers with potentially limitless capability of specifically labelling their species of interest.

The second one was confocal microscopy. Laser confocal scanning microscopy, by using a spatial pinhole to block out-of-focus light, drastically reduced the noise of the images, improved the sensibility of microscopy, and allowed for reconstruction of three-dimensional structures by means of acquiring serial two-dimensional images at know z-steps.

However, regardless of the quality and flexibility of the system, there is a physical limit to the capability of visualization of structures with microscopy. This so-called “resolution limit” stems from the phenomenon of light diffraction when passing through the finite lens of a microscope **(Figure 1)**. When applying the Nyquist-Shannon sampling theorem (Shannon and Weaver, 1949) to the case of light microscopy, we find that the resolving power of an optical microscope can be approximated to:

$$Resolving\ power = \frac{\lambda}{2NA}$$

Being λ the wavelength of the light source in nanometres and NA the optical aperture of the objective. Based on this, two objects at a distance of less than 200 nm cannot be resolved when illuminated with a wavelength of 400 nm (far blue). As such, when illuminated with a laser on the other side of the light spectrum, 647 nm (far red), the resolution power is approximately 320 nm.

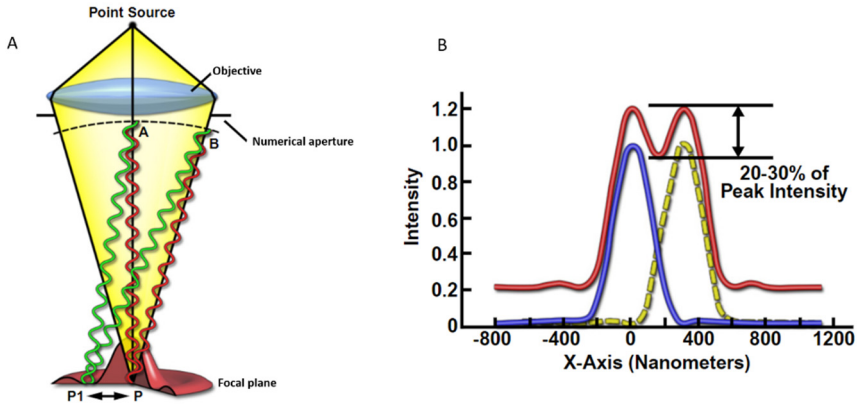

Figure 1. Resolution limit of optical microscopy. **(A)** Resolution limit is imposed by wavelength and objective aperture. Given a point of light P, a different point will not be possible to resolve until it is further away from the P1 point, being this a minimum of intensity of P produced by the destructive interference of two wavefronts arriving one-half wavelength out of phase. **(B)** Graphical representation of the Rayleigh Criterion of Lateral Axial Resolution. In order for two sources of light to be resolved, the distance between the points should be separated at least 200 nm apart. Adapted from (Silfies and Schwartz) - Nikon Instruments.

Most biological structures, such as proteins, DNA, and cytoskeletal element, are smaller than these distances. As such, new technologies need to be developed to image them.

One of the first technologies to appear was the electron microscopy technique. This is based on using a beam of accelerated electrons as an illumination source. Due to the inherently smaller wavelength of the electron, the resolution power is increased. Nevertheless, this microscopy introduces the problem of heavy fixation procedures that can shrink the biological material and introduce artefacts, obscuring the high-resolution details. Furthermore, in the case of the nucleus, different structures can have different affinity to the contrast agents used, creating artefactual electron-dense and mass-

depleted regions. Some stains such as osmium tetroxide, lead salts or uranium acetate react poorly with DNA or are not selective for it (Hanaichi et al., 1986; Huxley and Zubay, 1961; Watson, 1958). Osmium ammine binds DNA but the treatment required destroys native chromatin structure (Olins et al., 1989).

The introduction of cryo-EM partially solved these problems. Cryo-EM is based on the difference in phase contrast between molecules and the vitreous ice in which the sample is embedded. The vitreous ice reduces the alteration of the chromatin structure, as the environment in which it is embedded is still aqueous. Nevertheless, the contrast of DNA against vitreous ice is somewhat poor (Bouchet-Marquis et al., 2006), and it remains challenging to identify chromatin structure and 3D organization in large volumes. Finally, until recently (Ou et al., 2017), it was only possible to visualize chromatin in vitro, outside of its nuclear environment.

Although great advances have been made in the field of EMT, there still remains a problem of contrast and specificity. Fluorescence microscopy allows us to label with high specificity a plethora of different species of interest and this versatility is lost in EMT. Lastly, unlike light imaging, electron microscopy does not allow for live cell imaging.

As such, several techniques have been developed in the recent years to overcome the resolution limit of live cell microscopy.

1.1 Super-Resolution Microscopy

The diffraction limit has been overcome in light microscopy by the development of the so-called “Super Resolution

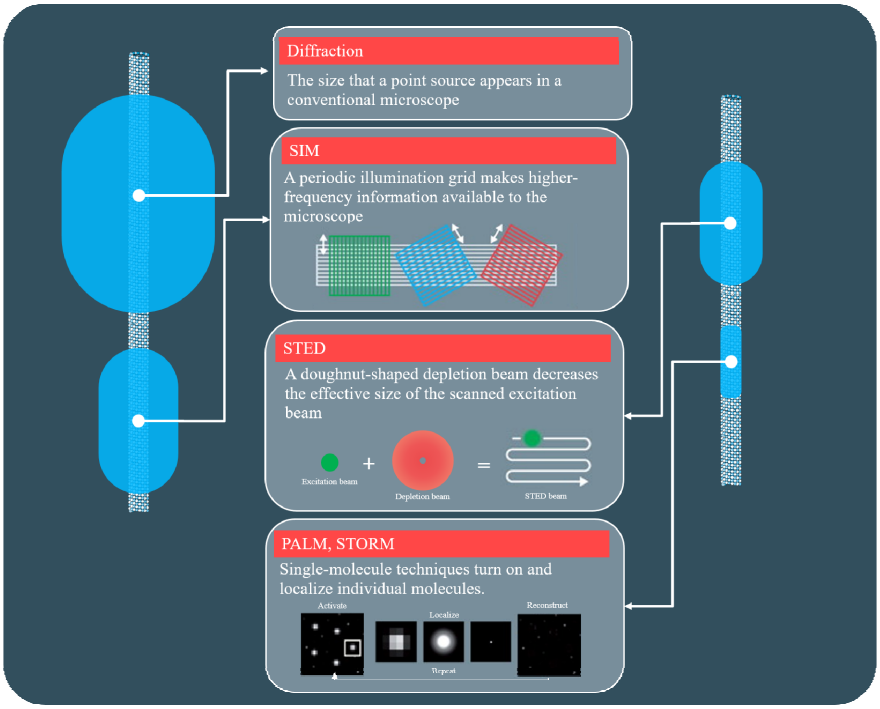

Figure 2. Scheme of the principle of different super-resolution techniques. Several techniques can be used to improve the resolution power of conventional microscopy. SIM is based on the illumination of the sample with sinusoidal stripped patterns. In STED, a depletion laser brings the fluorophores to a ground state and an excitation laser images the fluorophores in a region smaller than the resolution limit. Finally, Single Molecule Localization Microscopy techniques (PALM, STORM…) are based on the localization of the centroid of single molecules locally isolated. Adapted from (Galbraith and Galbraith, 2011)

Microscopy Techniques". This achievement merited the Nobel prize of Chemistry in 2014. Super-Resolution microscopy, also known as nanoscopy, is an umbrella term that comprises several techniques based on different principles. Since its inception, new techniques have steadily been developed **(Figure 2).**

The first of these techniques to be developed was the Stimulated Emission Depletion (STED) (Klar and Hell, 1999; Klar et al., 2000).

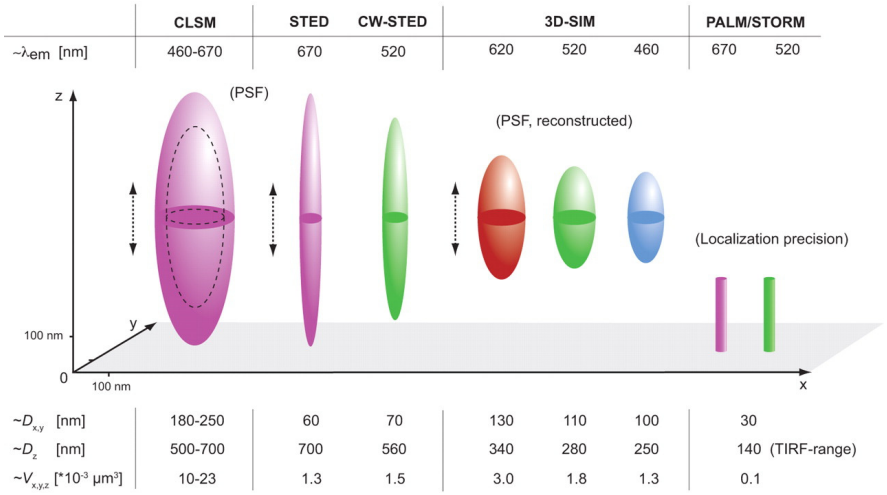

Figure 3. Comparison of the lateral and axial resolution power of each technique, and its variation with different wavelengths. CLSM: Confocal Laser Scanning Microscopy STED: Stimulated Emission Depletion, 3D-SIM: 3D Structured Illumination microscopy, PALM: Photo-Activated Localization Microscopy, STORM: STochastical Optical Reconstruction Microsocpy. PSF: Point Spread Function. Adapted from (Schermelleh et al., 2010)

STED is based on the use of two different lasers. One, ring-shaped, called “depletion beam” brings the fluorophores to a ground state. The other excites the fluorophores situated in the centre of the ring. As this ring has a sub-diffraction limit size, it allows to resolve structures beyond the diffraction limit. STED displays 50-70 nm lateral resolution and 500-700 nm axial resolution **(Figure 3)**.

Another widely used super resolution technique is called Structured Illumination microscopy (SIM) (Gustafsson, 2000; Heintzmann and Cremer, 1999). It is based on the illumination of the sample with sinusoidal stripped patterns of high spatial frequency. This is achieved by the use of a physical optical grating. Due to the presence of the grating, Moiré fringes arise and are recorded by the microscope. This strip-shaped interference pattern is recorded multiple times with changing positions of the grating.

1990	Two-photon microscopy	(Denk et al., 1990)
1991	Near –field scanning optical microscopy (NSOM)	(Betzig et al., 1991)
1992	4Pi microscopy	(Hell and Stelzer, 1992)
1994	Stimulated emission depletion (STED) microscopy	(Hell and Wichmann, 1994)
2000	Structured illumination microscopy (SIM)	(Gustafsson, 2000)
2004	Selective plane illumination microscopy (SPIM)	(Huisken et al., 2004)
2006	Photoactivated localization microscopy (PALM) Stochastic optical reconstruction microscopy (STORM) Fluorescence photoactivation localization (FPALM) Points accumulation for imaging in nanoscale topography (PAINT)	(Betzig et al., 2006) (Rust et al., 2006) (Hess et al., 2006) (Sharonov and Hochstrasser, 2006)
2008	Direct STORM (dSTORM) Ground state depletion followed by individual molecule return (GSDIM) Blink microscopy Spectral precision distance microscopy (SPDM)	(Heilemann et al., 2008) (Folling et al., 2008) (Heilemann et al., 2008; Lemmer et al., 2008)
2009	Super-resolution optical fluctuation imaging (SOFI) Quantum dot triexcitation imaging (QDTI) Reversible photobleaching microscopy (RPM)	(Dertinger et al., 2009) (Hennig et al., 2008) (Baddeley et al., 2009)
2014	DNA and exchange PAINT	(Jungmann et al., 2014)
2015	Oligopaint	(Beliveau et al., 2014)
2017	Oligostorm	(Beliveau et al., 2017)

Table 1: Timeline of invention of different Super-resolution fluorescence techniques

Via the use of cross-correlation and minimization algorithms, the original experimental parameters are reconstructed and a super-resolved image can be rendered. This method has been further improved by the introduction of 3D-SIM (Gustafsson et al., 2008; Schermelleh et al., 2008), in which the excitation light is modulated in 3D, which increases the resolution limit along the z-axis, achieving a resolution power of 100 nm laterally and 250 nm axially **(Figure 3).**

Finally, there are several techniques that are not based on structuring the pattern of illumination of the lasers, but on the localization of single, individual fluorophores. These are called Single Molecule Localization Microscopy techniques (SMLM). As the present work is focussed on SMLM techniques these will be described with more detail in the next section.

1.2 Single-Molecule Localization Microscopy

All the single molecule localization microscopy techniques are based on using different strategies to register the fluorescence coming from a subset of well isolated fluorophores of the sample at a given time **(Figure 4A).**

Due to the phenomenon of the diffraction of light, the signal of a single fluorophore is bigger than the fluorophore itself, generating a point spread function (PSF), i.e. the distribution of light coming from a single fluorophore. The PSF normally takes the form of a two-dimensional Gaussian function. If the PSFs of all fluorophores present on a sample are detected simultaneously the PSFs will overlap and the position of each PSF cannot be determined. If instead only a subset of sparse PSF are detected, the centroid of these functions can be calculated, acquiring in that way the position of the fluorophore with very high precision in x and y (Annibale et al., 2012; Thompson et al., 2002; Yildiz et al., 2004). Commonly, the x, y

information belonging to the centroid of an identified PSF is known as a **localization.**

The localization precision of a PSF depends on a number of factors such as the background signal, the properties of the camera and the optics used. The localization precision of a Gaussian-shaped PSF has been formalized as:

$$\Delta X^2 = \frac{\sigma^2 + \frac{a^2}{12}}{N}(1 - 4\tau + \sqrt{\frac{2\tau}{1+4\tau}}),$$

Being $\tau = \frac{2\pi b(\sigma 2 + a2/12)}{N\ a2}$, N the number of signal photons, σ the standard deviation of the PSF, a the pixel size and b the background per pixel.

With a high signal to noise ratio and bright, isolated fluorophores, 20 nm of lateral resolution can be achieved, i.e. one order of magnitude higher resolution than diffraction limited microscopy.

One of the seminal works in this field was the one by Moerner's Lab (Moerner and Kador, 1989) in which they were able to identify single fluorophores in a dense medium.

But this only, although a powerful tool, is not enough to break the diffraction limit. In biological samples the signal is very dense, and a normal fluorescence image integrates the information from a large quantity of fluorophores emitting at the same time. As such, it is necessary to develop methods in which a single fluorophore can be isolated and reliably identified.

What finally allowed to actively control the density of signal in any desired biological sample was the discovery of photoswitchable fluorophores (Bates et al., 2005; Heilemann et al., 2005; Patterson and Lippincott-Schwartz, 2002).

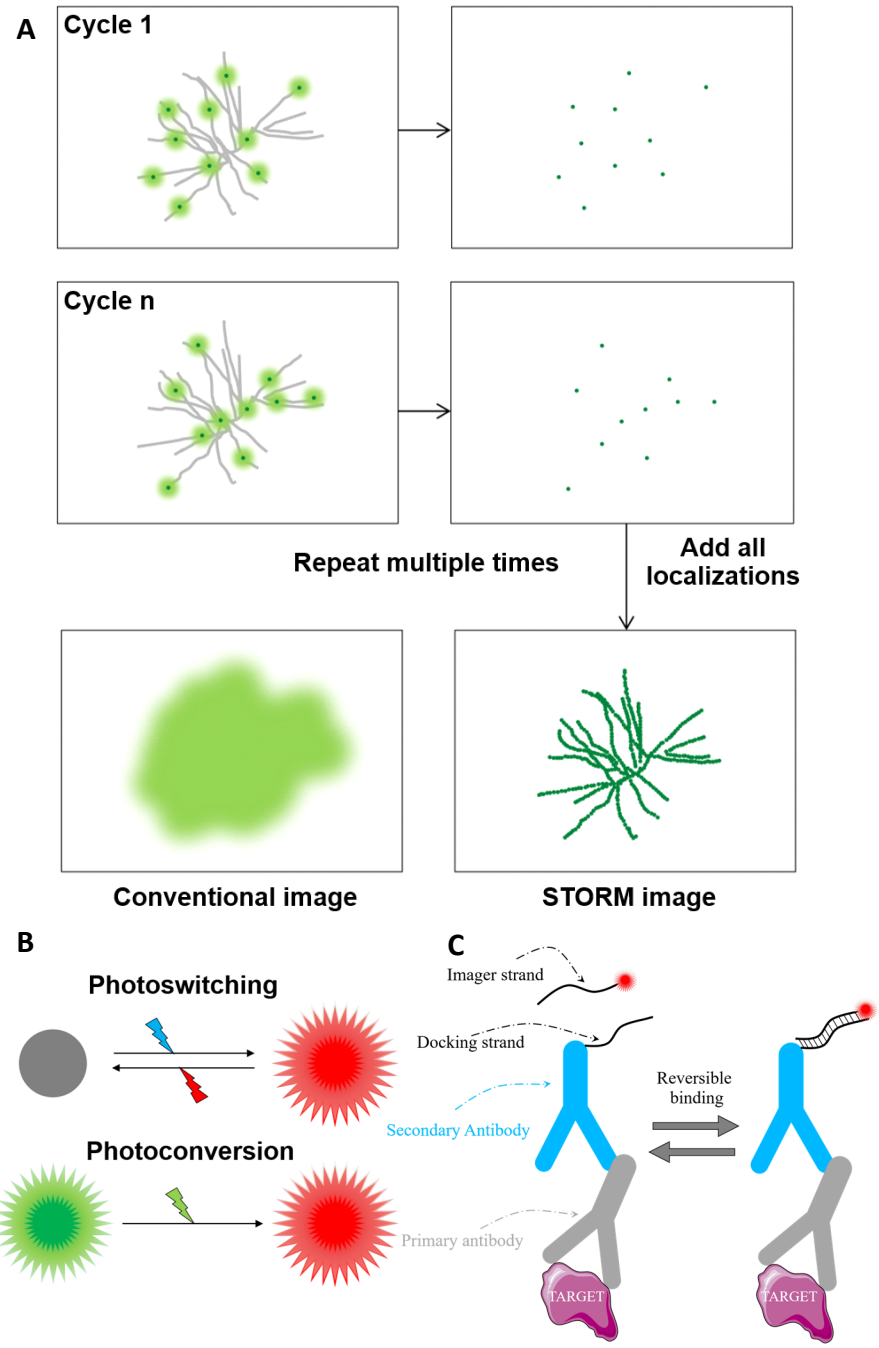

Figure 4. Principles of SMLM. (A) If a protein is labelled with photoswitchable fluorophores, the centroids of the PFSs coming from individual fluorophores can be detected and a super-resolved image can be obtained. The same sub-difraction structure cannot be

seen when using conventional microscopy. Adapted from (Oddone et al., 2014). **(B)** Principle of photoswitching and photoconversion. **(C)** Principle of PAINT microscopy, based on the transient binding and unbinding between two strands of DNA, and the accumulation of photons derived of the immobilization of the strand linked to a fluorophore.

In order to sample only a subset of fluorophores in any given frame, SMLM techniques make use of photoswitchable or photoconvertible dyes or proteins **(Figure 4B)**. Photoswitchable dyes are capable of reversibly transitioning from a bright to a dark state while photoconvertible proteins can change between two different emissions wavelengths. Under certain regimes of high illumination power density, basic or neutral pH and reductive environment, most dyes switch to a reversible dark state. Only a small subset of fluorophores will be “on”, emitting photons, at any particular moment. As such, the centroid position of PSF of spatially isolated fluorophores can be defined with high precision.

Although the process of photoswitching and photoconversion is stochastical, if the sampling of the image is long enough, we can potentially obtain PSFs belonging to all the fluorescent molecules in our sample.

Throughout the years, a myriad of related SLML techniques have been developed. In the next sections the most relevant methods to this work will be described putting emphasis on their respective advantages and peculiarities.

1.2.1 STochastical Optical Reconstruction Microscopy (STORM)

Developed in 2006 (Rust et al., 2006), combines the single molecule localization and fluorophore photoswitching concepts in order to obtain PSFs from individual fluorophores.

Among the photoswitchable fluorophores used for STORM, Alexa647 is the one most commonly used, as it presents a good signal to noise ratio, high number of detected photons per cycle, high extinction quoficient (high percentage of survival fraction) and high number of switching cycles. Other dyes have been used for two colour applications, as we will address later, but Alexa647 remains the gold standard.

Photoswitchable dyes are often paired with a second fluorophore in the same antibody, such as Alexa405, Cy2, Alexa488 or Cy3. These dyes are called “activator” fluorophores, as their presence allows to increase the photoswitching efficiency of the “reporter” fluorophore when illuminating with the correspondent activator excitation laser.

The activator-reporter pair strategy can be also applied to obtain two colour images (Bates et al., 2012; Bates et al., 2007), as we will address in Chapter 1.4.

1.2.2 Photo-Activated Localization Microscopy (PALM)

PALM microscopy is based on a similar principle to that of STORM, but instead of using organic dyes, it relies on fluorescent proteins. One such type are the photoswitchable proteins, such as PA-GFP and PA-mCherry (Patterson and Lippincott-Schwartz, 2002; Subach et al., 2009).

Other proteins used for PALM are photoconvertible, changing emission from one wavelength to another. In this category are two of the most widely used proteins for PALM: Dendra2 and mEOS2. Both of them are modified GFP proteins that change from green to red emission when excited with UV illumination.

(Coltharp et al., 2012; McKinney et al., 2009; Wiedenmann et al., 2004; Zhang et al., 2012).

PALM is used to perform SMLM in both live and fixed cells. One caveat is that the high laser power used, together with the low wavelength nature of the photoactivation/photoconversion laser used can be toxic for the cell. Furthermore, when imaging structures sensitive to UV-light damage, such as the nucleus, this phototoxic effect can be increased (Strack, 2015; Wäldchen et al., 2015). Another caveat is that, as we will discuss in Chapter 1.6, SMLM images need a large number of consecutive frames of acquisition to be able to resolve the structure. If we are imaging highly transient structures, or proteins/complexes that have a really high diffusing coefficient inside the cell, it will be hard to obtain a clear picture of the cellular structure of interest.

1.2.3 Point Accumulation for Imaging in Nanoscale Topography (PAINT)

PAINT technology (Jungmann et al., 2010; Schnitzbauer et al., 2017) is based on the use of chemical binding kinetics to mimic photoblinking **(Figure 4C)**. In PAINT, two strands of DNA that transiently bind to each other are used. One, called “docking strand”, is tethered to the secondary antibody. The other, named “imager stand”, is covalently linked to a fluorescent dye and is provided as free diffusing molecule in the imaging buffer. By adjusting the length and sequence of the DNA strands, the kinetics of binding between the imager strand and the docking strand can be finely adjusted.

During the image acquisition regime, the imaging strand will be freely diffusing in a liquid media. As such, the amount of photons that will be captured at each pixel of the camera will

be low, as the strand, due to the free movement, will not stay at a particular point for more than a few milliseconds and hence will not produce PSF-like signals. Conversely, when the imaging strand transiently binds to a docking strand, it is immobilized from tens to hundreds of milliseconds. As such, the photons accumulate, producing a PSF, and allowing for the sub-diffraction limit localization.

Jungmann and colleagues demonstrated this approach (Jungmann et al., 2010) resolving structures in DNA origami, designed non-arbitrary self-folding DNA structures at a nanoscale structure (Zadegan and Norton, 2012). Since then, DNA PAINT has been also adapted to the imaging of biological structures.

The fact that the acquisition of the PSF is not dependent on the use of fluorophores with particular physical properties makes DNA-PAINT a versatile technology compatible to acquire images in any wavelength without *a priori* detrimental effect.

1.3 3D SMLM data

When we perform SMLM techniques, we have a lateral resolution of 20 nm, but we do not receive precise information about the z position of the molecules. Although STORM can be performed with Epifluorescence Illumination regime, it is normally coupled with a TIRF module, in order to improve the signal to noise ratio. As a TIRF illumination regime can only illuminate by definition the surface of the cell, a common method to improve the signal to noise ratio when imaging proteins inside the cell is to use HILo illumination regime (Tokunaga et al., 2008). In it, the use of an inclined beam increased around 8-fold the signal to noise ratio. This allows

us to obtain localizations in a z projection of around 1.5-2 μm of thickness.

In order to obtain z information, the most commonly used technique is based on the inclusion of an astigmatic lens in the path between the fluorophore and the camera **(Figure 5A)**. The astigmatic lens introduces a deformation on the image dependent on its position in z. When acquiring PSFs, they will appear as circular when in focus, as elongated in x when below focus and elongated in y when above focus. When comparing the PSF shape to a previously acquired calibration curve **(Figure 5B)**, we can obtain the z-position of the localization with a 50 nm precision.

Other methods involve the use of a biplane module, which decouples the image by a known z distance in two different fields. The difference in brightness between the same molecule obtained in two fields can give us information about its z position based on a previously acquired calibration curve.

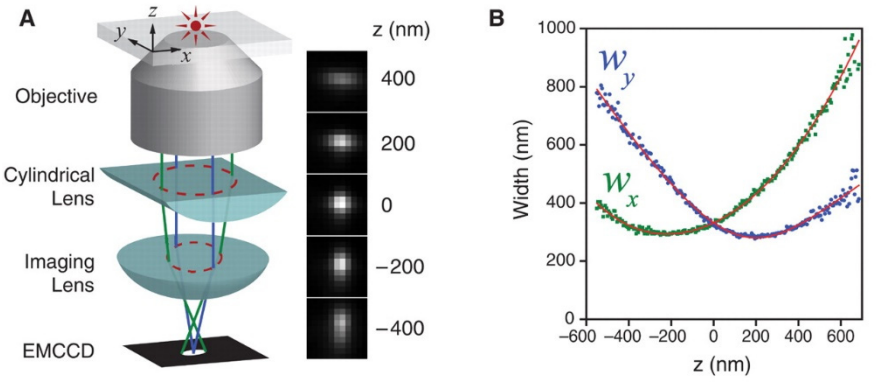

Figure 5. 3D SMLM data is obtained using an astigmatic lens. **(A)** When an astigmatic lens is in the path of the image acquisition, the PSFs are deformed in x or y according to their relative position to the focal plane. **(B)** Using immobilized beads, a calibration curve can be acquired, which allows obtaining a z position for each spot with ~50 nm resolution. Adapted from (Huang et al., 2008).

Certain developments have made possible the acquisition of SMLM data using confocal systems (Schueder et al., 2017) but it is still not a widely used technology.

1.4 Obtaining multi-color images with super-resolution microscopy

Due to the long imaging time and the need for specific fluorophores, co-imaging several species using SMLM is not a trivial matter. Several approaches can be taken in order to achieve this. The most straightforward solution is to use, in the same manner as with normal microscopy, two different STORM-compatible dyes with different emission wavelength, and recording one colour after the other **(Figure 6A).** This gives the problem that not all fluorophores are optimal for STORM microscopy and not all fluorophores have the same optimal buffer conditions, needing an optimization and compromise for obtaining the highest amount of localizations possible in the two colours. Also, the use of two different fluorophores introduces chromatic aberration, requiring appropriate correction. Finally, the mechanical set-up tends to drift with time, and this drift needs to be accounted for and corrected.

One possible solution for the drift problem is to intermingle the two wavelengths, acquiring a certain amount of frames in one wavelength and alternating with the other, or using a beam splitter and acquiring the two colours simultaneously in two halves of the camera field / two different cameras. This last approach introduces the problem of the need to correctly align the two different images fields in post-processing. Nevertheless, this strategy has been used in several studies (Georgieva et al., 2016; Xu et al., 2018).

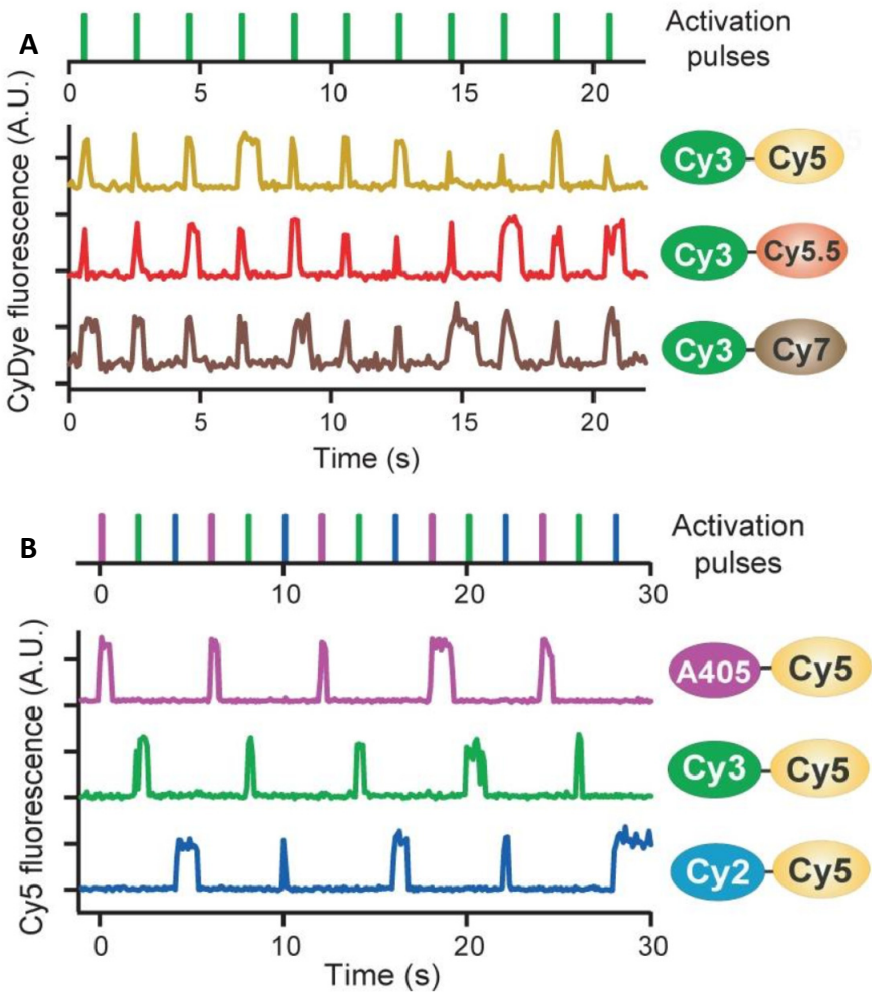

Figure 6. Strategies for dual colour image acquisition in STORM microscopy. **(A)** Different spectrally separated fluorophores can be used to obtain images in different channels **(B)** The same reporter dye can be used if coupled with different activator pairs. That way the localizations obtained after each activation pulse will be specific for that particular activator-reporter pair. Adapted from (Bates et al., 2007)

Another possible strategy is to use two different pairs of activator-reporter dyes on the labelled antibodies **(Figure 6B)**. The reporter dye (usually Alexa647) will be the same in the two antibodies, but it will be coupled to different dyes, excited with different wavelengths, usually A405 and Cy3. When acquiring

dual colour images using the same reporter, the usual procedure is to intersperse one frame of activator excitation (e.g.: 405) with 3 frames of reporter excitation; followed by one frame of the other activator (e.g.: 560) and three frames of reporter excitation again. The localizations belonging to the reporter frame immediately after the exposition frame are assigned to the corresponding activator-emissor pair. The localizations of the other two reporter frames are used to calculate the amount of crosstalk from one colour to the other.

One final strategy, largely unexplored, is combining different compatible SMLM approaches based on different principles. In this work, **we have developed a method of combining STORM imaging with PAINT imaging to obtain simultaneous dual color 3D super-resolved images using spectrally separated dyes.** We have also designed a post-acquisition protocol in order to correctly obtain localizations and align them with nanometric precision for the two colours.

1.5 Applications of SMLM microscopy

STORM microscopy fundamentally allows us to resolve structures inside the cell with a previously unachieved resolution. Structures in the cell include elements of the cytoskeleton such as actin (Xu et al., 2013) and microtubules (Bates et al., 2007) but also not fully defined structures like macro-molecular complexes (Sigal et al., 2015) or the distribution of chromatin inside the nucleus (Ricci et al., 2015). The information that can be extracted from STORM imaging is intrinsically tied to the type of structures that need to be resolved.

Some of the most relevant published works carried out using STORM microscopy have been done imaging *regular and spatially separated structures*. We can identify these structures

as self-similar regular fibres or macro-molecular complexes **(Figure 7A).** Under this condition, we can take advantage of the spatial separation between the structures to easily identify them separately and to filter the inherent noise of any biological sample. Some of the first papers where this technology has been used were the ones that resolved actin rings in neuronal axons (Xu et al., 2013).

A very interesting application derived from the identical nature of the structures analysed is that the images obtained can be averaged to refine and define the structure to resolution limits below those obtained by one simple image. Averaging a high number of images can produce a composite image that “fills” the information lacking from one separate image due to inherent technical limitations (labelling efficiency, stochastic blinking…). It is worth noting that in this case, before doing the averaging is necessary to align the structure spatially. One such example is the reconstruction of the nuclear pore complex by (Szymborska et al., 2013) .

Not all the structures are regular tough, and STORM also allows us to identify *non-identical but well-isolated structures* **(Figure 7B).** In this case, we can obtain data regarding the variation of the structures, and its population distribution. The biological meaning behind this variation could be attributed to variations of the cell homeostasis (eg: drug treatment or differentiation) or to heterogeneity in cell populations. As the structures are isolated, it is still possible to distinguish between them without the need for complex computational operations, but special care has to be placed not to attribute biological meaning to changes that can be due to labelling or experimental variability. To this category belongs for example the imaging of hoxB locus in mouse embryonic stem cells (Beliveau et al., 2015) or the imaging of the T-loop formation in telomeres (Doksani et al., 2013).

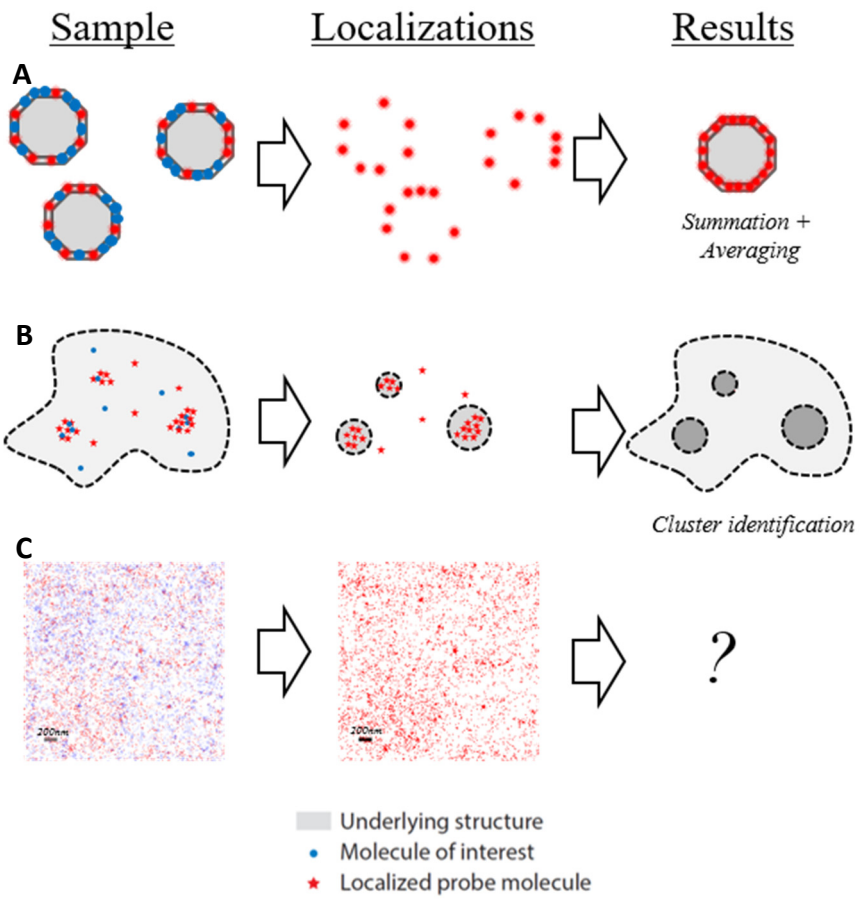

Figure 7. Applications of STORM microscopy. (A) Imaging of regular and spatially separated structures. **(B)** Imaging of non-identical but well-isolated structures **(C)** Imaging of non-identical, densely packed structures. An experimental sub-set of DNA SMLM data has been used.

Finally, one of the hardest structure types to visualize with STORM are *non-identical, densely packed structures* **(Figure 7C)**. In this case, extra steps have to be taken into account to identify the structures, separating them one from the other in a reliable manner. It is also the situation in which the highest labelling density is needed, as it is difficult to distinguish if any difference in parameters between labelled structures in the

same sample condition is due to undersampling or due to biological variation.

Furthermore, the potential high fluorophore density means that special care has to be placed to avoid simultaneous blinking of neighbouring fluorophores. Too many localizations per frame can cause dense features to appear artifactually empty due to this reason. Once the images have been obtained, complex computational analysis methods have to be used to segment the image and find any feature such as filaments, clusters or distribution differences.

One such densely packed, irregularly distributed, but strikingly interesting structure is the chromatin, and the packing of both DNA and histones in the nucleus, which is our focus in this thesis. This work began with the publication of a revolutionary paper in which the structure of nucleosomes was described using Super-Resolution microscopy (Ricci et al., 2015).

1.6 Caveats of SMLM

Due to the particular characteristics of Single Molecule Localization Microscopy, a series of caveats inherent to the system arise.

As it is necessary to acquire tens to hundreds of thousands frames for a single image, the system has a lower throughput than other microscopy techniques. Acquiring an image can take from several minutes to one hour in certain cases, which makes obtaining a significant number of cells a time-consuming endeavour.

Stemming from that, the long acquisition times can produce a drift in the field being acquired. This results in a “blurred” image, akin to a moving picture with a camera. Various

systems have been designed to solve this problem, from the use of the information on the image being obtained (Geisler et al., 2012; Mlodzianoski et al., 2011; Wang et al., 2014) to the use of external fiduciary beads (Lee et al., 2012) in order to determine the vector of drift during the image acquisition.

PAINT imaging, although versatile, has a longer acquisition time, as the transient binding of the imaging strand and posterior photon accumulation normally last 100 to 300 ms (Blumhardt et al., 2018; Schnitzbauer et al., 2017).

Another important caveat is the need for fluorophores with ideal photo-physical properties for STORM imaging. The consensus on the field is that Alexa647 is the best performing dye for STORM. Although photo-physical properties of other dyes and their compatibility with STORM have been documented (Dempsey et al., 2011), they behave inherently worse than A647. As we have discussed before, if we are imaging a non-regular, non-isolated structure, high localization precision and labelling density is needed. In this work, we present a comparison of behaviour of different STORM-compatible dyes and its viability for labelling chromatin. We demonstrate that none of the chosen dyes has a good enough performance to reliably be able to reconstruct chromatin images from which we can extract changes on chromatin distribution.

As such new SMLM microscopy methods have to be developed. In this work, we have combined STORM microscopy in the far-red channel with PAINT microscopy in the red channel, and we have designed a method in order to solve the different requirements for buffer and exposure time, in order to visualize both DNA/RNA and chromatin simultaneously in super-resolution.

2. CHROMATIN AND THE DNA

The DNA is structured in several macromolecular chains that add up to 6.468×10^9 bp for humans. If we linearized that, we would obtain a fibre of approximately 2 meters. The average diameter of a human nucleus ranges from 10 to 20 μm. It stands to reason that the organization of this complex macromolecule in such space is not a trivial matter.

One of the first distinctions of organization of the DNA inside the nucleus was the definition of euchromatin versus heterochromatin. Heterochromatin is classically defined as a densely packed, transcriptionally inactive region of the DNA in the nucleus. In contrast, euchromatin is a less densely packed, transcriptionally active state of the DNA. The difference in density between the two categories of chromatin already hinted to the structure and distribution of the DNA in the two regions being fundamentally different.

2.1 The nucleosome

Organization of the DNA occurs at several orders of magnitude. At the smallest level, DNA is wrapped around an octamer of histones, forming the nucleosome. The nucleosome structure was solved at 2.8Å using X-ray crystallography (Luger et al., 1997). It was found that the DNA wraps 1.65 times on a left-handed orientation around histones. The union of DNA to histones confers (in the form of electromagnetic interactions) the energy to pack the DNA in a much smaller volume.

Between each pair of nucleosomes lies a non-histone associated strand of DNA, called “linker” DNA. The size of a nucleosome is of ~11 nm in diameter with a lateral side of ~5.5

nm. Due to its size, this structure is outside of the resolution power of conventional light microscopy.

Nucleosomes are not only a structural protein. As we will discuss in this introduction, a nucleosome is also a functional unit, and the ways it packs the DNA and interacts with other nucleosomes are inherently tied to the biological processes of the cell.

2.1.1 The histones

Eight histone proteins form the core octamer of a nucleosome. Histones are highly conserved proteins, divided in five types: H1, H2A, H2B, H3 and H4 **(Figure 8A).** It was described (Kornberg, 1974) that two dimers of H2A/H2B and two dimers of H3/H4 assemble, forming two tetramers. These tetramers interact with each other in the presence of DNA forming an octamer. Histone proteins are positively charged, which allows them to interact with the negatively charged DNA forming non-covalent bonds.

The histone H1 does not form part of the nucleosome core. Instead, it interacts with DNA at the entry and exit points of the nucleosome, wrapping around an extra 20 base pairs of DNA (P Hergeth and Schneider, 2015). In this way, it neutralizes the remaining negative charges, facilitating the folding of DNA (Finch and Klug, 1976).

Through the linker histone H1, the 10 nm fibre further compacts into higher order structures (Thoma et al., 1979). Although highly conserved, the histone octamer is not an invariable unit. There are different ways in which the DNA packing can be finely tuned by histones.

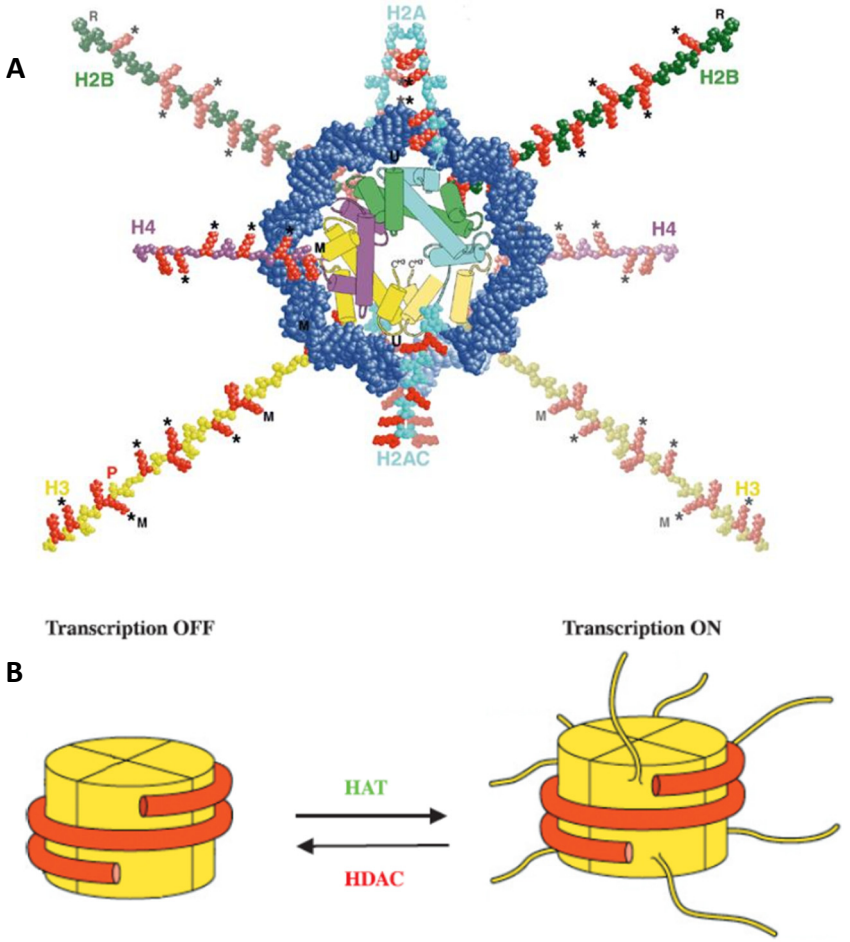

Figure 8. Post-translational modification and its effects on DNA-Histone interaction. (A) Histone tails and protein core are viewed along with the DNA interacting with them. The N-tails are viewed as extended polypeptide chains to show approximately their relative size. The α-helical histone fold is colored according to the histone proteins. H2A=cyan, H2B=green, H3=yellow, H4=magenta. Modifiable residues in the N-tails are colored in red. Sites of acetylation (*) methylation (M), phosphorylation (P) rybosylation (R) and ubiquitination (U) are indicated (Wolffe and Hayes, 1999). **(B)** Effect of acetylation mediated by Histone Acetyl Transferases (HAT). The neutralization of the positive charges alters the histone-DNA interaction and facilitates transcription. This effect is reversed by Histone Deacetylases (HDAC).

2.1.2 Chromatin regulation by histones

Histones are encoded by multiple genes encoding for a variety of histone variants. Variants mainly differ at the levels of the N-terminal region (Henikoff et al., 2004) making them differentially sensitive to post-translational modifications or slightly structurally different. Some histone variants are preferentially associated with particular regions of the genome or with particular developmental stages (Buschbeck and Hake, 2017; Chen et al., 2013). The distribution and representation of histone variants can change among cell types and can respond to specific stimuli as DNA damage (Chen and Jin, 2017).

Post-translational modifications (PMT) of histones are one of the most important mechanisms of epigenetic regulation. The core histones, and in particular H3 and H4, have N-terminal protein tails extending away from the nucleosomes. These tails can be covalently modified at different residues (Bannister and Kouzarides, 2011; Rothbart and Strahl, 2014). More than 60 residues can be modified on these histones, tails can be methylated, acetylated, phosphorylated, or ubiquitinated, among other modifications. The combination of these different modifications has been defined as “histone code” (Jenuwein and Allis, 2001). These modifications play a vital role in regulating cell processes such as cell cycle control, replication or transcription.

For example, histone modifications at enhancers and promoters, favour DNA accessibility to transcription factors and transcription machinery (Li et al., 2007).

Similarly, PMTs directly influence chromatin high order folding as they change the physical properties of the fibre, affecting the structure of the chromatin. Some modifications are

inherently tied to the formation of heterochromatin or euchromatic regions.

Regarding heterochromatin, some modifications such as H3K9me3 (Nakayama et al., 2001) are permanent signals for heterochromatin formation. Others such as H3K27me3 indicate transient, temporary signals for chromatin compaction in developmentally regulated regions (Kuzmichev et al., 2002; Simon and Kingston, 2013; Wiles and Selker, 2017).

Regarding euchromatin, acetylation has been generally associated with open chromatin (Roth et al., 2001) **(Figure 8B)**. Open chromatin makes the promoter of the genes more accessible to transcription factors, increasing gene expression. Consequently, acetylation such as H3K9ac or H3K27ac is normally associated to enhancers and promoters of active genes.

Specifically, lysine acetylation neutralizes lysine positive charges. This neutralization results in a reduction of the electrostatic attraction between the histone tails and the negatively charged DNA. It has thus been postulated (Eberharter and Becker, 2002; Verdone et al., 2005) that histone acetylation results in a more “open” chromatin fiber with the DNA more loosely attached to the nucleosomes. In addition, all-atom molecular dynamics simulations suggested that acetylation can disrupt inter-nucleosome interactions leading to unfolding and de-compaction of the chromatin fiber (Collepardo-Guevara et al., 2015). This chromatin opening leads to an increased accessibility of the transcription factors and RNA Polymerase II holoenzyme and therefore to transcriptional activation (Eberharter and Becker, 2002; Verdone et al., 2005). While previous work using *in vitro* reconstituted chromatin and all-atom molecular dynamics simulations led to a molecular model of acetylation-induced

chromatin fiber decompaction, how acetylation impacts chromatin structure *in vivo* is less clear.

2.2 Chromatin-folding: higher order chromatin structures and the 30-nm fiber

The classic model of chromatin organization established that the 10 nm fiber formed a regular 30 nm structure in “native” mitotic chromosome. This structure was named the “solenoid”. Although this structure was observed in isolated chromatin, soon proof against its presence began to arise.

In 1986 Dubochet observed vitrified sections of mammalian mitotic cells using cryo-EM. They could not identify any 30 nm-sized regular structure. They postulated the chromosome structured as an aggregation of 10-nm fibers (Dubochet et al., 2009; McDowall et al., 1986).

Using synchrotron X-ray scattering (SAXS) (Nishino et al., 2012) only 11 and 6 nm peaks were found in HeLa mitotic chromosomes. They concluded previously observed 30 nm peak was due to ribosome contamination on the chromosome surface. This was again proved in interphase nuclei (Joti et al., 2012; Maeshima et al., 2014).

Since then, other proofs have appeared suggesting that the chromatin nanoscale organization is much more rich, variable and heterogeneous than the 30 nm fiber **(Figure 9)**. In-situ analysis of cryo-electron microscopy did not support the existence of 30-nm chromatin fibers in mitotic chromosomes (Eltsov et al., 2008). In addition, the development of ChromEMT (Ou et al., 2017) allowed for 3D chromatin structure visualization in interphase mitotic cells.

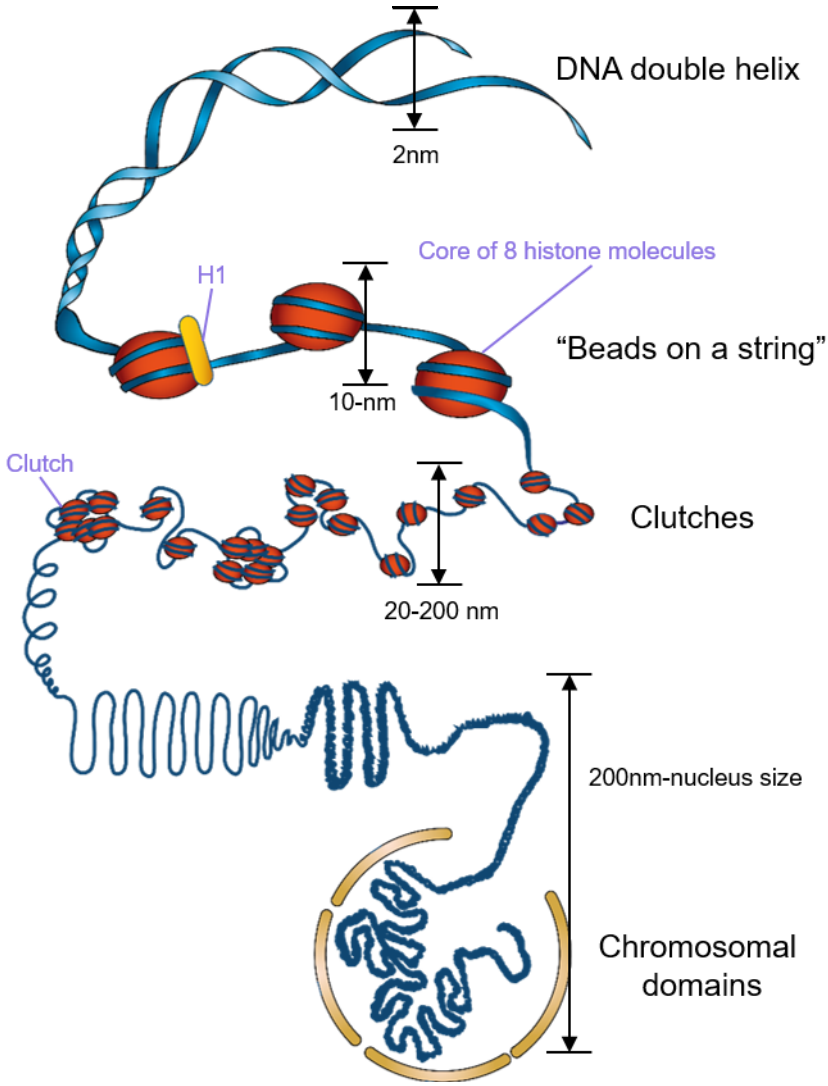

Figure 9. Chromatin structures at different orders of magnitude. The DNA double helix (2 nm) wraps around the histones, forming the 10 nm "beads on a string" fiber. The histones, in turn organize in discrete nanodomains, termed clutches, with linker, histone depleted DNA between them. Some clutches are aggregated in islands. All the DNA belonging to a chromosome is situated in a Chromosome Territory in the nucleus of interphase somatic cells.

These results show the chromatin as a flexible and disorganized granular chain, in which the 30 nm fiber was not found. Furthermore, the data suggests that the assembly of 3D domains with different concentration is what determines DNA accessibility and transcriptional activity, and not higher order folding.

Maeshima postulated that the chromatin is irregularly folded in “chromatin liquid drops” of closed chromatin with transcription occurring at the surface of the drops. The difference between euchromatin and heterochromatin would be in this way much more flexible, with nucleosome fibers constantly moving and rearranging (Maeshima et al., 2010). As such, the emerging picture suggests that chromatin is organized in 10 nm fibers with heterogeneous, variable levels of compaction, dependent on the epigenetic state of the nucleosomes.

In addition to electron microscopy and SAXS, Super Resolution microscopy was also used to resolve the DNA folding and chromatin structure in the nucleus.

2.3 Chromatin domains: higher order of genome organization

The idea of the chromosomes being organized in separate, discrete regions of the nucleus in interphase nuclei appeared more than a century ago (Boveri, 1909; Rabl, 1885), but it was only in 2010 when it was finally established and extended as a model (Cremer and Cremer, 2010).

These regions were named Chromosome Territories, and nowadays they are considered to be one of the major features of nuclear architecture.

Recent studies have drastically improved our knowledge about the internal structure of the chromosome territories. It has been suggested that each chromosome is comprised of many distinct chromatin domains, referred as topologically associated domains (Dixon et al., 2012; Jackson and Pombo, 1998; Nora et al., 2012). These are defined as regions of the chromosomes that physically interact with each other and are isolated from other regions **(Figure 10)**. Due to its conservation in cell types, they have been considered a basic feature of chromosome organization (Cremer and Cremer, 2010; Dekker and Mirny, 2016; Sexton and Cavalli, 2015).

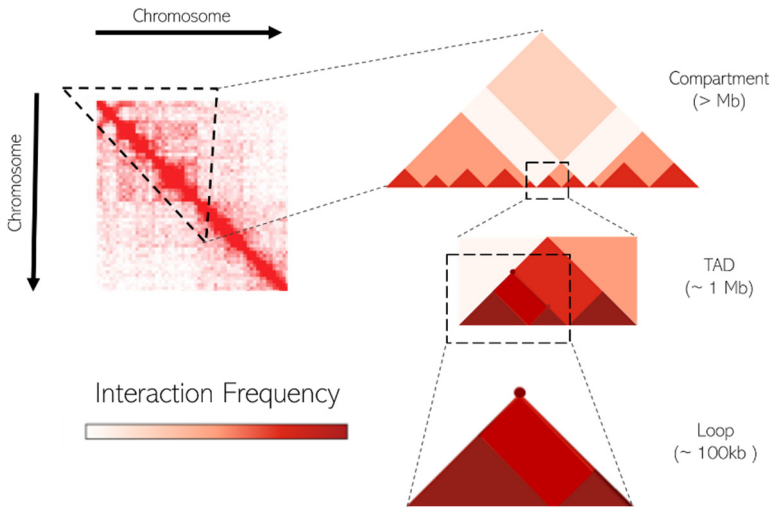

Figure 10. Genomic organization along the chromosome. Levels of 3D genomic organization analysed from low resolution (left) to high resolution (bottom right) by Hi-C contact maps. The degree of darkness of the red areas is directly proportional to the interaction frequency of the corresponding genomic sequences.

The fact that the genome is structured in interacting domains was discovered thanks to the Chromosome Conformation Capture techniques, which allow to study the spatial organization of the genome at high-resolution, measuring the

contacts between different regions of the genome (Dekker et al., 2002).

Hi-C is one highly efficient type of these techniques, widely used nowadays (Lieberman-Aiden et al., 2009), allowing the idenitication of interactions across the whole genome.

Using Hi-C, it was observed that the whole genome could be split into two spatial compartments, labeleld “A” and “B”. Chromatin domains from the “A” compartment tend to associate between them. Chromatin domains of the “B” compartment tend to associate with other B-compartment associated regions (Lieberman-Aiden et al., 2009).

Altough these techniques are highly powerful, they have one severe limitation, and that is that they only allow the study of a cell population. As such, the variability within the population, which could be biollogically meaningful, gets lost (Liu et al., 2018).

By contrast, super-resolution microscopy allows us to inquire about the organization of the chromatin on a cell-by-cell basis.

2.4 Imaging nucleosomes in vivo using Super-Resolution imaging

As we have mentioned before, the chromatin structure of the cells cannot be resolved with conventional optical microscopy techniques. Consequently, X-ray scattering or cryo-EM techniques have been used to investigate chromatin organization until the advent of SMLM opened up new exciting possibilities.

One of the first works exploiting the potential of SMLM to interrogate chromatin was that of (Ricci et al., 2015). In this paper it was shown that the nucleosome structure *in vivo* is formed by clusters of nucleosomes, termed “clutches” of variable size. Also, it was reported that the median size of the nucleosome clutches was dependent on cell type and tied to the pluripotent state of the cell.

At the same time, these clutches were reported to be often grouped with other nearby clutches, in regions termed “islands”. For that, images of H2B, one of the least variable units of the nucleosomes were taken using 2D-single color STORM imaging **(Figure 11A).** These cluster nanodomains reflect the organization of the chromatin fibers and are not of uniform size. In order to obtain quantitative data of the size and number of localizations for nanodomain, a clustering algorithm was developed **(Figure 11B).**

Using this clustering algorithm, the population of clutches could be observed. It was seen that, upon chromatin hyperacetylation using Trychostatin A (TSA), a HDAC inhibitor, the population of the clusters skewed towards a lower median clutch size **(Figure 11C)**. Chromatin was not only organized in discrete nanodomains, but this organization changed dynamically according to the epigenetic state of the cell.

To study the relation between the epigenetic state of the cell and the arrangement of chromatin, images of chromatin were obtained in several cell types, ranging from more to less differentiated. Human fibroblasts (hFB) were also treated with TSA in order to increase histone acetylation and thus to alter the epigenetic state of the nucleus. The results showed that the median clutch size was characteristic of cell type. Differentiated cells had a higher median clutch size with respect to pluripotent cells which, showed a smaller median clutch size **(Figure 11C, Figure 12A,B)**.

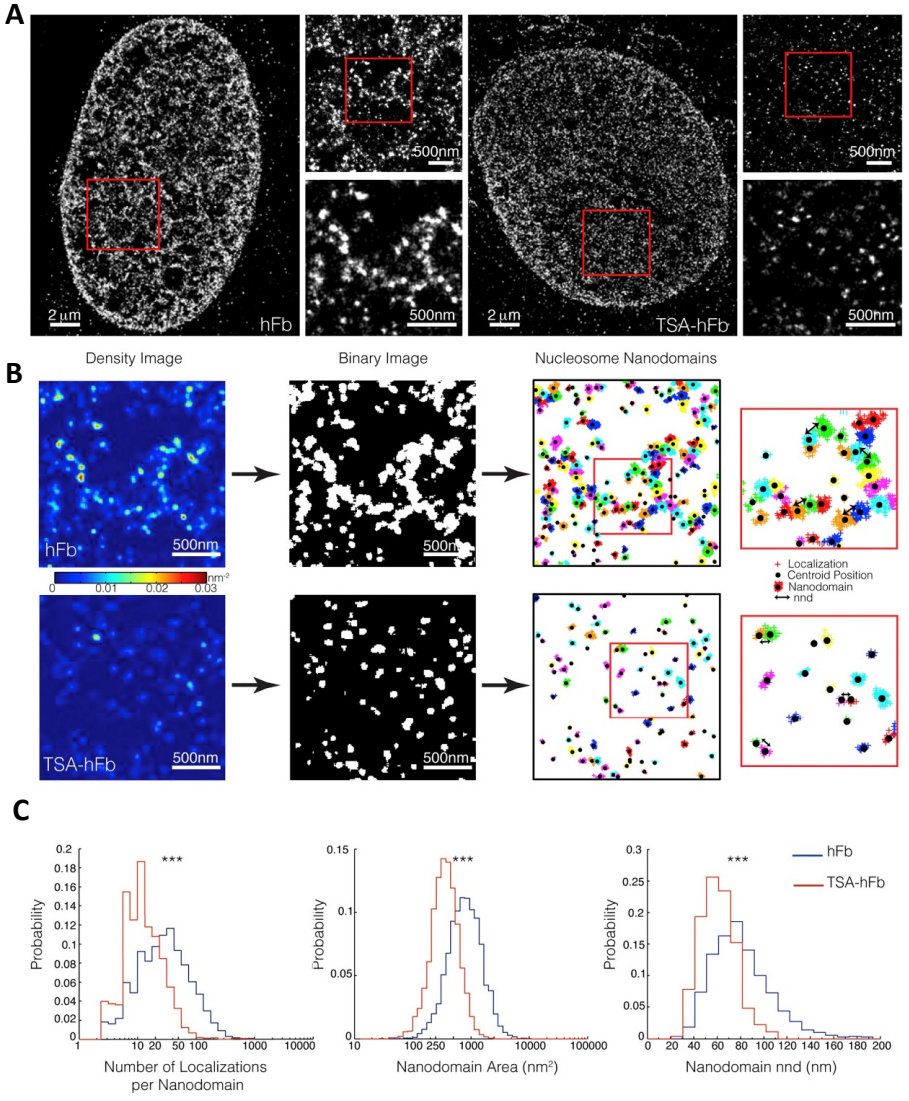

Figure 11. Nucleosomes Are Arranged in Discrete Nanodomains in Interphase Nuclei of Human Somatic Cells. (A) Representative Storm images H2B in human fibroblast (hFB) nucleus, in untreated and hyperacetylated (TSA treated) condition. When hyperacetylated, the clusters are qualitatively smaller. **(B)** Scheme of nucleosome cluster analysis for normal and TSA-hFB cells. **(C)** Nucleosome cluster population distribution in normal and TSA-hFB cells. Control cells have a population of clusters significantly bigger and denser. Adapted from (Ricci et al., 2015).

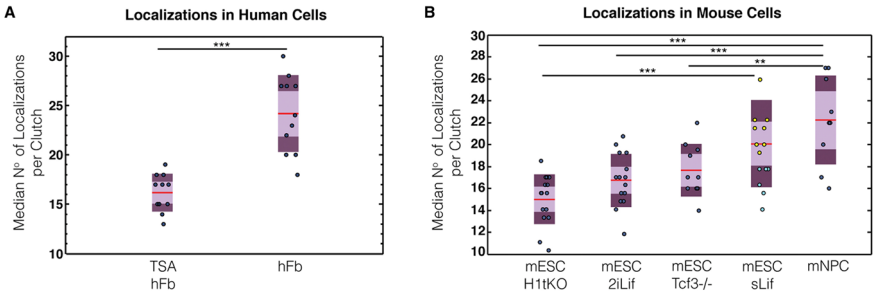

Figure 12. Number of localizations per clutch correlates with cellular state. **(A)** Box plot showing the median number of localizations per clutch in human fibroblast treated with TSA compared with control. **(B)** Box plot showing the median number of localizations per clutch in different mouse cell types. The grade of pluripotency inversely correlates to the median number of localizations per clutch.

Furthermore, when co-imaging H2B with H1, it was found that larger nucleosome clutches showed increased co-localization of H2B with H1, indicating that large clutches likely included heterochromatin. This was further confirmed by showing that large clutches were included in centromeric regions.

Using this data, computer simulations of nucleosome occupancy were performed. According to the simulations and the imaging results, it has been shown that the organization of the chromatin in discrete, spatially separated clutches implies the presence of nucleosome-depleted regions in the chromatin fiber.

This could be explained by two different models **(Figure 13)**. The first would explain the presence of this nucleosome depleted regions by variations in the linker DNA length. Differences in base pair distance between nucleosomes due to nucleosome sliding would create these depleted regions. Alternatively, the nucleosomes could be outright removed from the DNA fibre, understandably creating depleted regions. Both models were able to reproduce *in silico* the results obtained in the super-resolution images.

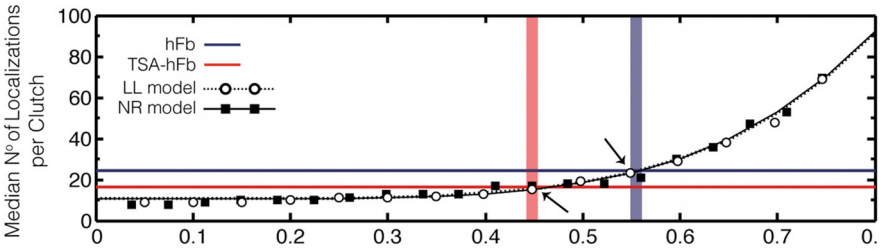

Figure 13. Computer simulation of nucleosome occupancy. Simulations of nucleosome occupancy based on the linker length alteration model (white circles) and the nucleosome repositioning model (black squares) Intersect with experimental data (red bar for TSA-hFB, blue bar for hFB) for calculation of nucleosome occupancy.

This study cemented the organization of the chromatin in clutches of varying size and density, interspaced by nucleosome-depleted regions, whose size and density are correlated with cell pluripotency.

Since then, several studies have shown the chromatin using SMLM and super-resolution microscopy. Protocols have been developed for STED (Mitchell-Jordan et al., 2012) and SIM microscopy (Kraus et al., 2017), but they still remain unable to achieve the resolution of SMLM based techniques.

Other studies (Fang et al., 2018) which imaged DNA in single chromosomes arrived to similar conclusions regarding the organization of chromatin. They found that the DNA was structured in dispersed fibers, well-defined nanodomains (corresponding to clutches) and groups of nanodomains (correspoding to islands).

Recent work showed a correlation between the size of chromatin domains, epigenetic modifications of these domains and DNA packing density within the domains (Xu et al., 2018). For example, regions with silencing epigenetic marks had larger domains and higher DNA packing density than regions

with activating epigenetic marks. However, whether smaller clutches pack less DNA simply because they contain fewer nucleosomes (i.e. lower nucleosome occupancy) or whether the epigenetic modifications of the nucleosomes within a clutch impacts its DNA packing density is unclear.

To that effect, we aimed to finely study what is the effect of epigenetic modifications on the N-tails (particularly, acetylation) in the chromatin nanodomains (clutches) and how this affects its capability to pack DNA.

3.-TRANSCRIPTION AND ITS RELATION TO NUCLEAR ARCHITECTURE

Transcription is the mechanism by which cells read or express the genetic information of the genes. From one gene several copies of the sequence can be synthetized in the form of RNA. Each RNA molecule, in turn, can be used to synthetize several copies of the protein. Due to this double step of regulation, If needed, the cell can quickly synthetize a large amount of copies of protein from only one copy of a gene (generally, two). As each gene is transcribed and traduced with different efficiency, and this efficiency can be regulated, the cell can change the expression of any given gene according to different conditions, ranging from a large amount of production to a total repression of the gene.

RNA TYPE	FUNCTION
mRNA	Messenger RNA. Codify proteins
tRNA	Transfer RNA. Adaptors between mRNA and aminoacides in protein synthesis
rRNA	Ribosomal RNA. Part of the basic ribosomal structure. Catalize protein synthesis
snRNA	Small Nuclear RNA. Have a direct role in different cellular processes, such as splicing
snoRNA	Small Nucleolar RNA. Processing and chemical modification of rRNA
scaRNA	Small Cajal RNA. Modification and processing of snoRNA and snRNA
miRNA	microRNA. Gene expression regulation
siRNA	Small Interference RNA. Inhibit gene expression trough direct selective degradation of Mrna
ncRNA	Non Coding RNA. Diverse cell processes, such as telomere synthesis, X chromosome inactivation or protein transport.

Table 2: Main types of nuclear RNAs synthetized by the cells

The RNA is a single strand molecule, generated as a complementary to a DNA molecule. It is way smaller than the DNA, but much more variable. As we have said before, a molecule of DNA can have several millions of base pairs. A RNA molecule, in turn, can range from tens to thousands of bases. There are several types of RNAs, classified according to their function and the enzyme which synthetises them.

The range and variety of RNA transcribed by the cell is enormous. In average, in a nucleus, the most abundant RNA is the rRNA, which is confined in the nucleolus. Less expressed is the mRNA, which codifies the cellular proteins, and can be potentially synthetized in any part of the nucleus.

3.1 RNApol is the family of proteins which synthetize RNA

Eukaryotes have several types of polymerases. The main ones are RNApol I, II and III. They are structurally similar, but synthetize different RNA types.

RNApol I	rRNAs 5.8S, 18S and 28S
RNApol II	All codificant genes, snoRNAs,miRNAs, siRNAs and some snRNAs
RNApol III	tRNAs, rRNA 5S, some snRNAs and other small RNAs

Table 3: Nuclear RNA Pol in eukaryotes and the RNA that they transcribe

Nuclear RNA Polymerases share 5 subunits, and are highly similar to archeal polymerases (Langer et al., 1995; Zillig et al., 1978). We will center on RNA Polymerase II (Pol II), as it is the one responsible for the transcription of all the coding genes. Pol II in humans is formed by 12 subunits that interact between them to perform the transcription (Bernecky et al., 2016;

Cramer et al., 2000; Cramer et al., 2001). Although it has more subunits and complexity than the prokaryote polymerase, the DNA binding domain is very conserved, sharing basic structure and mechanism. This indicates that the basic features of the enzyme appeared before the divergence between prokaryotes and eukaryotes.

In the subunit RPB1 the carboxy terminal domain (CTD) can be found. This domain is composed of a 25-52 heptapeptide repeats (YSPTSPS). This CTD can undergo post-translation modifications in a similar way to those of the histone N-tails. Its main modifications are phosphorylation in the second (Ser2) and fifth (Ser5) serine of this heptapeptide. The name does not refer to the position of the Serine in the aminoacid sequence but to its position in the heptapeptide repeat. Trough phosphorylation of the CTD, this interacts differentially with several proteins that regulate the transcription process.

Although the process of transcription is similar between the different domains of life, the main differences between eukaryotic transcription and the others are:

1.-Eukariotic RNA pol needs several additional factors in order to transcribe genes, as the Pol II alone does not have capability to recognize the promoter. The RNApol together with its general transcription factors form the RNA polymerase II holoenzyme

2.-As we have addressed before, in eukaryotic cells the DNA is differentially packed around the histone octamers. The transcription process has to be able to solve this problem in order to successfully transcribe the genes.

3.2 Pol II mediated transcription.

The transcription process is composed of several sequential steps (**Figure 14**):

Recruitment and Pre-initiation complex formation: Before Pol II can bind to the DNA, several factors have to be recruited to the transcription initiation side. These factors act by altering the chromatin structure, or directly interacting with the transcription machinery.

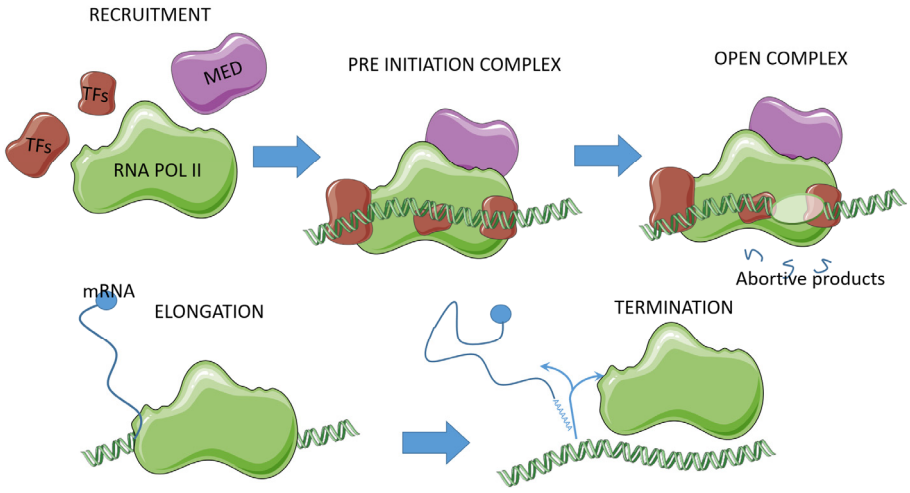

Figure 14. Scheme of the process of RNA transcription. Pol II, the Mediator complex and the Transcription Factors are recruited to the DNA, were they form the Pre Initiation Complex. They mediate the opening of the DNA and the production of the first RNA abortive products. Pol II transcribes the RNA until the gene is finished, at which point it terminates transcriptions and disassembles from the DNA fibre.

These general transcription factors constitute an interacting group of proteins called TFII (Transcription Factors for polymerase II), and once assembled together with Pol II they form the Pre-initiation complex (PIC).

The first steps towards assembly of the PIC are the recognition of the promoters by the transcription machinery. Eukaryotes have several consensus sequences found near promoters, which will direct the binding of units of the transcription machinery and its directionality. No element is essential, but most promoters contain at least one of them. The most widely known are i) the TATA box or Goldberg-Hogness box, recognized by the TBP; ii) the BRE element, recognized by TFIIB; iii) the Downstream Promoter Element, recognized by TFIID; and the Initiator Element, also recognized by TFIID (Smale and Kadonaga, 2003) .

On top of all the different subunits of Pol II and the basal transcription factors, other elements play a role for a successful initiation of transcription. One of these is the mediator, a multi-protein complex that interacts with both transcription factors and the RNA pol holoenzyme in the PIC to stabilize and initiate transcription.

Finally, several chromatin-remodelling factors, together with histone modifiers must also be recruited in order to overcome the organization of the DNA around the nucleosomes.

Once the PIC has been recruited, 11-15bp of DNA near the docking site open up, with the template strand positioning itself in the active site of Pol II, forming the Open Complex. The transcription begins with the synthesis of multiple short RNAs (3-10 bases)(Holstege et al., 1997; Luse and Jacob, 1987). These are called abortive products. Once it begins the proper synthesis of RNA, the Polymerase stops interacting with the core promoter elements.

In this phase, the CTD, which was recruited in an initial, unphosphorylated state, becomes highly phosphorylated in ser5 by the TFIIH-associated kinase CDK7, which will help

recruit enzymes to cap the 5'end of the transcript (Egloff and Murphy, 2008) (**Figure 14**).

It is worth mentioning than in higher eukaryotes there is an intermediate step separating initiation and the next phase of transcription, that of signal integration. Pol II is then transiently paused near the promoter region before elongation starts (Jonkers and Lis, 2015) .

Elongation: Once the polymerase has been released, it advances through the DNA synthetizing the single strand RNA. During this elongation process it progressively loses its Ser5 phosphorylation and accumulates ser2 phosphorylation (**Figure 15**). This phosphorylation is mediated by the CDdk9 subunit of the positive transcription elongation factor b complex. Ser2 plays a role in avoiding elongation block and in recruiting factors, which increase its processivity. It also plays a role in splicing and polyadenylation (Bowman and Kelly, 2014; Hirose and Manley, 1998; Jonkers and Lis, 2015; Zhou et al., 2012)

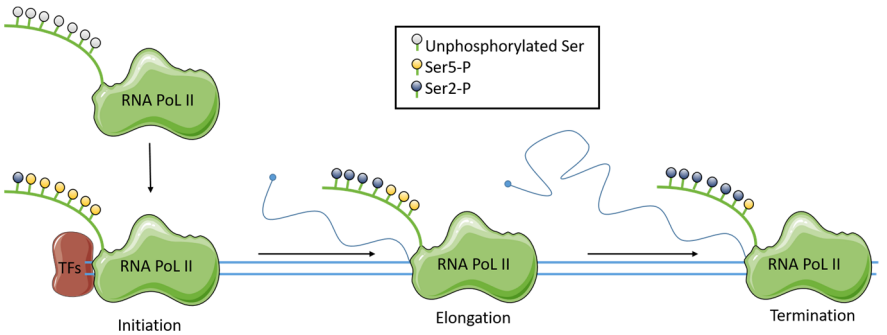

Figure 15. Pol II transcription phases correlate with distinct patterns of CTD phosphorylation. The phosphorylation status of the CTD heptapeptide repeats changes as Pol II transcribes the gene. Hypophosphorylated Pol II is recruited into the pre-initiation complex. There CDK7 phosphorylates Ser5 during initiation. During elongation, CDK9 phosphorylates ser2 as Ser5 becomes progressively dephosphorylated. Each phosphorylation represents a heptad repeat, with the general phosphorylation pattern indicated.

Interestingly, the advance of Pol II introduces supercoiling in the DNA helix. As Pol II transcribes, positive supercoiling is produced in the direction of advancement, leaving negative supercoiling behind. The positive super-coiling can stall the polymerase. As such, TOP1, a topoisomerase bound to the front part of Pol II, can relax the positive supercoiling (Brill et al., 1987; Champoux, 2001). It has been seen that Pol II stimulates TOP1 activity by mediation of the ser2 phosphorylated CTD (Baranello et al., 2016).

Termination: It has been seen that transcription trough poly(A) regions reduces the rate of Pol II elongation, causing even pausing of the Pol II. In poly(A)-dependant termination in humans, the AAUAAA signal sequence is recognised in the RNA by the human cleavage and polyadenylation specificity factor (CPSF), bound to the Pol II body. The cleavage stimulatory factor, bound to the CTD tail, interacts with CPSF and dislodges it from the Pol II, allowing it to cleave and release the transcribed RNA.

The action of CPSF would generate an unprotected 5'-end, that would be recognized by the 5'-3' exoribonuclease (XRN2) degrading the rest of the RNA product until reaching the Pol II and dislodging it from the DNA, in which has been called the "torpedo model".

3.3 Transcription and its relation to chromatin folding and structure

As we have mentioned before, transcription is a process that does not happen in naked DNA in the eukaryotic genome. The DNA is associated with histones and the histones are, in turn, associated in clutches. The transcription process is inherently tied to the chromatin structure. There is an interdependent

relation between transcription and DNA structure, in which one influences the other, and vice versa.

Transcription is dependent on chromatin structure. The heterochromatic regions are highly folded, electrondense DNA regions. In it, the nature of the nucleosome interactions and the particular histone N-tail modifications results in low transcriptional rate.

Conversely, euchromatic regions are more permissible to the binding of transcription factors and the Pol II complex. Survey of the bound transcription factors showed that, except for a few transcription factors, which are bound to either facultative or constitutive heterochromatin, the majority of transcription factors bind almost exclusively to open chromatin (Thurman et al., 2012). As such, transcription is highly dependent on the chromatin state of the cell.

Given this, it would be easy to think of transcription as being contingent on the pre-existing chromatin organization, which would direct which genes are engaged in transcription activity and which remain silenced and not transcribed. But the Pol II is not a passive player. Transcriptional activity plays a role in chromatin organization and folding at multiple levels.

As we have discussed before, the advancement of transcription alters the local chromatin characteristics through multiple mechanisms. Pol II is responsible for the recruiting of numerous chromatin remodelling complexes, such as those of the SWI/SNF family.

First of all, the Pol II cannot simply advance along the DNA when this is interacting tightly with the histones. It has been seen that the process of elongation displaces H2A-H2B dimers from the nucleosome, allowing the passage of Pol II (Kireeva

et al., 2002; Kulaeva et al., 2009). Furthermore, in higher eukaryotes, the H3-H4 tetramer is substituted by the variant H3.3-H4, which facilitates the elongation (Sarai et al., 2013).

In addition to histone exchange, the elongating Pol II has been shown to interact with different chromatin remodellers. As such, the passage of Pol II causes the deposition of numerous post-translational modifications in the nucleosomes. Histone acetylation complexes are recruited by the elongating Pol II to acetylate nucleosomes (Ginsburg et al., 2009; Govind et al., 2007; Wittschieben et al., 1999)

The phosphorylated CTD also can recruit complexes in charge of chromatin silencing in order to facilitate the repression of transcription. The Set2 complex co-transcriptionally methylates the H3k36, and Rpd3S deacetylase removes acetylation marks added during transcription (Keogh et al., 2005).

Another, drastically different mechanism by which transcription alters the chromatin is the introduction of negative supercoiling. Because topoisomerase TOP1, bound to the front part of Pol II, is able to relax positive supercoiling, transcription generates a net negative supercoiling (Baranello et al., 2016) behind it. This negative supercoiling thus starts at the level of actively transcribed sequences and tends to propagate as a flux along the chromatin fibre (Hanafi and Bossi, 2000; So et al., 2011). This negative supercoiling has been linked to a more open chromatin conformation, facilitating the access of DNA-binding transcription factors and polymerases (Gerasimova et al., 2016; Ma and Wang, 2014).

We have described how the Pol II can influence chromatin structure at a local level, that of its coding sequence. This process mainly affect individual nucleosomes along the coding

region. It would seem then that Pol II would be a player in the small-scale organization of chromatin, but not responsible of the higher-order chromatin organization. But recent studies have been strengthening the link between Pol II activity and nuclear architecture.

It has been suggested but not yet proved (Stigler et al., 2016) that Pol II is responsible for the translocation of the cohesin ring, thus being the motor for higher order chromatin compartmentalization **(Figure 16)**. A method by which transcription is responsible for cohesin translocation has been proposed (Racko et al., 2018). As we have described previously, the advance of Pol II introduces negative supercoiling in the genome. This negative supercoiling could generate the torsional tension necessary to push cohesin.

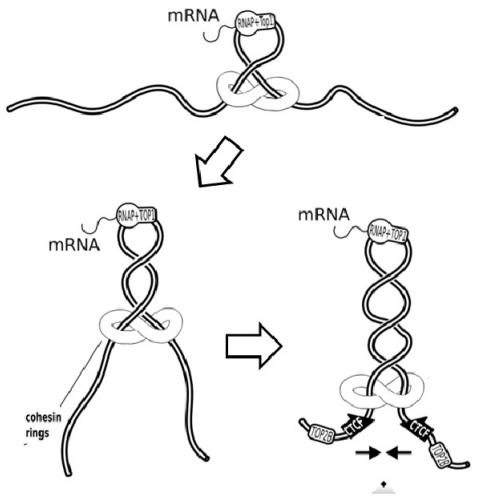

Figure 16. **RNA polymerase drives the organization of nuclear architecture.** Transcribing Pol II in association with TOP1 induces formation of negative supercoils. When cohesin is loaded, the growing supercoiling is responsible for loop formation. Thus, transcription is inherently tied to chromatin architecture. Adapted from (Racko et al., 2018)

If we address whole genome organization, it has been shown that transcription also plays an important role at even higher orders of chromatin folding. Transcription inhibition produces a partial loss of compartmental domains in *D.melanogaster* (Rowley et al., 2017). In fact, it has been observed that, during Drosophila development only the active genes form part of the compartments, and that the formation of new domains is linked to the activation of gene transcription (Hug et al., 2017). But transcription also affects the whole genome architecture in mammals, being necessary for domain formation in mouse embryos (Du et al., 2017; Ke et al., 2017).

.

In conclusion, as we have discussed, transcription has been revealed as both dependent of and responsible for chromatin architecture, becoming an important player in the spatial distribution of the genome inside the cell nucleus.

3.4-Physical distribution of transcription and RNA

We have talked about transcription as an isolated process, but the process of RNA transcription occurs in a tridimensional environment, with hundreds to thousands of genes producing RNA at the same time **(Figure 17A)**.

Traditionally, transcription has been visualized as the polymerase tracking along the DNA. The compelling "christmas tree" images **(Figure 17B,C)** (Miller and Beatty, 1969) show the polymerases tracking along the DNA. But these images are visualized in highly transcribed regions, after treatment with a hypertonic buffer, and are highly selected.

In vivo, there has been substantial evidence that the polymerases remain fixed and clustered with other polymerases, and it is the DNA what moves along, passing by this region **(Figure 17D)**. This region of higher density

aggregation of RNA polymerases and transcription factors is called a transcription factory, and it is defined as “a region where more than two polymerases are transcribing more than one gene” (Papantonis and Cook, 2013). This type of structures increase the efficiency of the transcription process. All the necessary elements of the holoenzyme, together with the transcription factors co-localize in a locus, which allows for faster transcription (Papantonis and Cook, 2011).

Several pieces of evidence have shown the presence of transcription factories. In first experiments, after addition of BrUTP to HeLa and human fibroblasts, and posterior immunolabeling, focal sites of RNA transcription could be seen **(Figure 17A)** (Jackson et al., 1993; Wansink et al., 1993). 3C conformation capture also added evidence to the existence of fixed RNApol (Gavrilov et al., 2010). Finally, simulations using Hi-C data propose the model of transcription being immobilized in different regions, and this transcription factories being a player in organization of nuclear architecture **(Figure 16, 17D)**. (Cook and Marenduzzo, 2018)

The number of transcription factories is not a constant. It can vary according to cell type, as seen when detecting transcription factories by immunofluorescence of active Pol II in mouse. In cultured embryonic fibroblasts ~1500 transcription factories could be seen, while in other cell types the number of transcription factories varied from ~100 to ~300 (Osborne et al., 2004). Also, different techniques used give wildly different numbers. When measuring transcription factories in HeLa cells, the number obtained varies drastically: 300-500 factories were shown by conventional fluorescence microscopy (Jackson et al., 1993), while upwards to 2100 factories were seen with the use of confocal microscopy (Iborra et al., 1996). In contrast, more than 8000 factories of Pol II were seen by cryosectioning (Pombo et al., 1999).

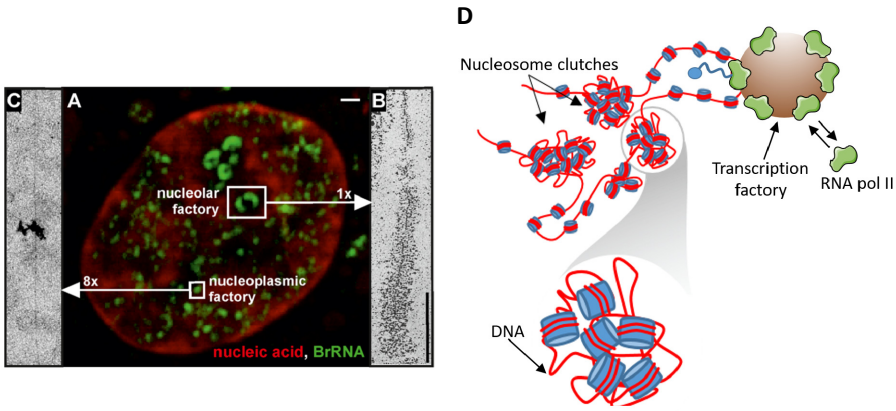

Figure 17. Active transcription sites on the nucleus. **(A)** Active transcription sites imaged with confocal microscopy. HeLa cells incorporated BrUTP, which was then immunolabelled. The DNA was stained with TOTO-3. Bar: 1µm. Adapted from (Cook, 1999) **(B)** "Christmas tree" structure of RNA transcription of rRNA, obtained with electron microscopy after stripping and spreading the DNA. **(C)** Stripping and spreading of a nucleoplasmic factory. Adapted from (Jackson et al., 1998) **(D)** Scheme of RNA transcription inside the nucleus.

This variation can be attributed to the dense, nuclear environment and the fact that transcription factories measurement show them to be sub-diffraction limited structures, measuring in Hela cells in the range of 40-170 nm (Eskiw et al., 2008). The use of super-resolution microscopy could shed light on the number and distribution of transcription factories in the cell. Even then, an aggregation of active Pol II would not necessarily mean that this is an active factory. There should be a combination with labelling of actively transcribed RNA in order to gain more information about the number, size, distribution and state of transcription factories, and its relation between its size and its transcriptional activity.

These transcriptional factories are not static. It has been reported that Pol II average residence time in the nucleus is about 20 min (Kimura et al., 2002). It has also been measured that the mean interaction time between RNA and RNApol is of 517 ± 103 s, corresponding to an elongation speed of 0.4 ± 0.08 kb min^{-1} (Darzacq et al., 2007). It is worth mentioning that these studies have shown that the rate of elongation is not constant, but an aggregate of a slower and a faster component, and that the polymerase has a chance of transiently stalling during the process. If we aim to study the nascent transcriptome, we should be able to specifically label the RNA being transcribed in a pulse of 10-20 min.

Super-resolution microscopy allows us to inquire about the distribution of the transcriptome, how it is organized in the nucleus, and how this distribution shapes in turn the distribution of chromatin. Taking advantage of this, we will also inquire about the distribution of Pol II, and what is the relation between the clusters of active Pol II and its transcriptional activity. For that, we will label specifically the nascent RNA, examine its distribution and structure in the nucleus, and combine this labelling with our developed dual-color labelling method to co-image the nascent RNA with active Pol II and chromatin.

PART II: Results

4.-COMBINED PAINT AND STORM SUPER-RESOLUTION MICROSCOPY ALLOWS VISUALIZATION OF TWO COLOR 3D DATA OF THE NUCLEUS AT THE NANOSCALE LEVEL

4.1-Labelling DNA

The main aim of this project was to investigate the nuclear distribution of both DNA and nucleosomes, the interplay between these two and how this shapes chromatin folding. In order to visualize DNA at a nanometric-scale, a method that ensures unbiased, uniform labelling of the DNA should be used. The labelling should not alter the chromatin conformation such as BrdU. Finally, a fluorophore capable of photoswitching or photoblinking should be employed.

These requirements discarded the usual DNA intercalators such as DAPI and Hoestch, as they are not capable of photoblinking. Some DNA stains such as picogreen have been reported to be SMLM compatible (Benke and Manley, 2012), but its results on terms of number of localizations and image quality are poor.

As such, we decided to use click chemistry in order to label the DNA. Click chemistry is an umbrella term coined by Barry Sharpless to describe reactions which are “modular, wide in scope, give very high yields, and generate only inoffensive (non-toxic) byproducts” (Hein et al., 2008; Kolb et al., 2001). The most well-known reaction, and the one we have used in this project is the Huisgen copper(I)-catalyzed azide-alkyne 1,3-dipolar cycloaddition (CuAAC). In this reaction, an azide group and an ethynyl group are covalently linked in a reaction catalysed by copper.

In our particular context, we use an ethynyl-modified deoxy-nucleotide, ethynyl-2’-deoxycytidine (EdC) (Qu et al., 2011),

which we link to an azide modified STORM-compatible fluorophores (Alexa647-azide). EdU (Ethynyl-2'-deoxyuridine) has also been used for this purpose, but it has been shown to be more toxic to the cell (Qu et al., 2011).

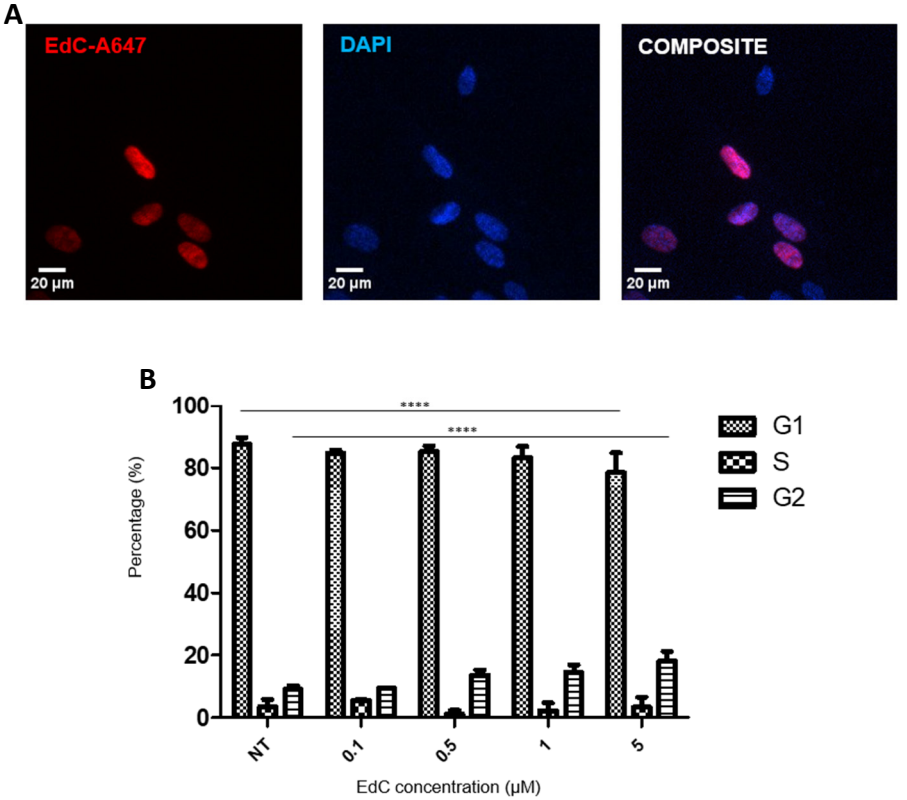

Figure 18. Effect of EdC labeling on cells. (A) Representative wide-field image of EdC treated click-labelled cells. (left) positive EdC-A647 labelled cells; (center) nuclear DAPI staining; (right) composite. **(B).** Percentage of cells in G1, S and G2 phase of the cell cycle after labeling with different concentrations of EdC. NT refers to Not Treated. Cells were sorted by flow cytometry after staining the DNA using Propidium Iodide. The quantification was done using the commercial program ModFit LT (Allen, 1990), for unbiased quantification of cell cycle phase populations. 87.5% of cells were in G1 in the absence of labeling (NT) and 78.4% of cells were in G1 after labeling with 5 µM of EdC. Stars indicate statistical significance according to an unpaired two way Anova with Bonferroni multiple comparison test against not treated $p<0.0001$. N=3 biological replicates and N=2-3 technical replicates per experiment.

EdC was provided at high concentration (5 µM) and for long enough time period (4 days) to ensure dense DNA labelling and enable visualization of global DNA organization. 67 ± 10% of cells were positive for EdC after this treatment **(Figure 18A)** and EdC labeling had minimal impact on cell cycle at the concentration and incubation time used (**Figure 18B**).

In order to visually check that all the DNA was being labelled, as well that we were not introducing artifacts by our labelling method, we labelled the cells with both Alexa-647 and DAPI **(Figure 19).**

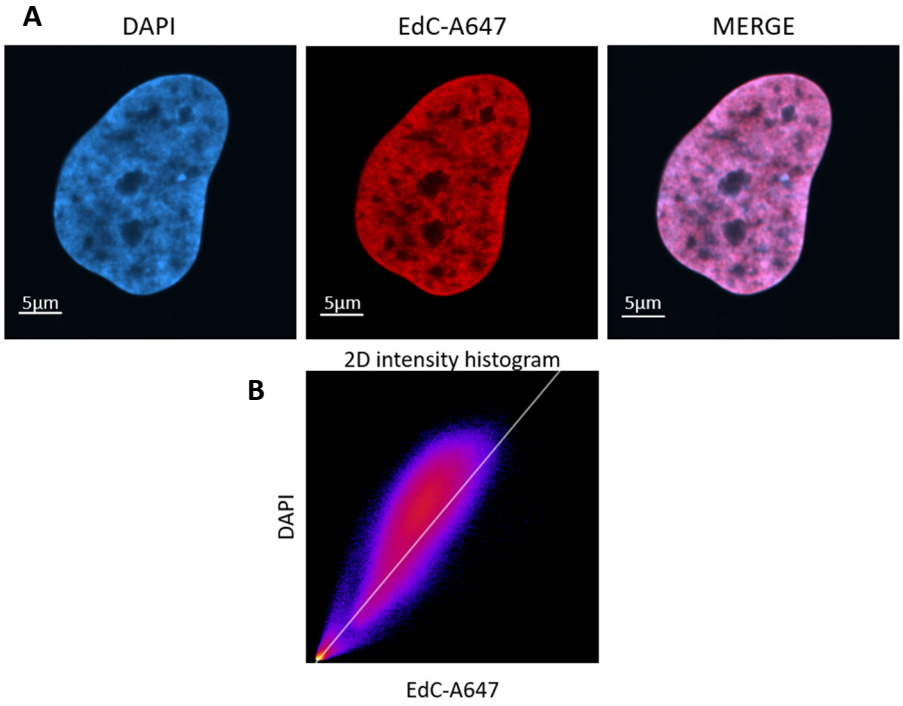

Figure 19. Click labelling allows visualization of the nuclear DNA. (A) Representative confocal microscopy image of nuclear labeling with DAPI **(left)** versus nuclear labeling with EdC followed by click chemistry **(center)** in the same cell and the overlay of the two labels **(right). (B)** 2D intensity histogram of EdC-A647 signal versus DAPI signal. Color code represents frequency of intensities. Pearson's R Value:0.98

Confocal imaging showed that EdC was uniformly incorporated into the genomic DNA **(Figure 19A)**. Overlapping analysis showed a 0.98 Pearson's R value between the signals (**Figure 19B**)

4.2 Dye alternatives to Alexa 647 are incapable of reliably reporting nucleosome structure

Previously, we showed that nucleosomes are organized in heterogeneous groups, which we termed nucleosome clutches, and demonstrated that nucleosome clutch size decreased in TSA-treated human fibroblasts (Ricci et al., 2015). To gain further quantitative insight into how the DNA is compacted by multiple nucleosomes present within an individual clutch, we aimed to carry out two-color super-resolution imaging of DNA and histone H2B to simultaneously visualize remodelling of nucleosome clutches together with their associated DNA.

As we have mentioned in Chapter 1.4, achieving multi-color SMLM is not trivial, as the requirements for the fluorophores are much more restrictive than in conventional microscopy.

Due to the fact that click chemistry covalently links an azide-modified fluorophore to the DNA, we could not use pairs of activator-reporter dyes in order to obtain dual color images, as there would be no way to distinguish the specific localizations coming from the DNA.

This, coupled with the fact that the click chemistry offers a limited choice for reliable super-resolution compatible fluorophores (mainly AlexaFluor647), makes us having to think of a different strategy in order to achieve dual color imaging. For that, we aimed to identify a second fluorophore with a different emission wavelength to carry out the

immunofluorescence labelling of histones. To this end, we first tested a wide range of fluorophores previously reported to be compatible with super-resolution microscopy (Dempsey et al., 2011) **(Table 4)**. We compared the histone clutch structure to those obtained by the best-performing dye AlexaFluor647 **(Figure 20A).**

Dye	Alexa 647	Cy3B	Alexa 568	Atto 488	Alexa 750
Excitation Maximum (nm)	650	559	578	501	749
Emission Maximum (nm)	665	570	603	523	775
Extinction (M−1cm−1)	239000	130000	91300	90000	240000
Quantum Yield	0.33	0.67	0.69	0.8	0.12
Detected Photons Per Cycle	3823	1365	2826	1341	437
Equilibrium Duty Cycle	0.0005	0.0003	0.00058	0.00065	0.00006
Survival Fraction (400 s)	0.83	1	0.58	0.98	0.36
#Switching Cycles (Mean)	14	8	7	11	1.5

Table 4. **Photophysical and switching capabilities of selected dyes**. The switching capabilities are reported in the presence of GLOX and 10μm MEA. Adapted from Dempsey et al., 2011.

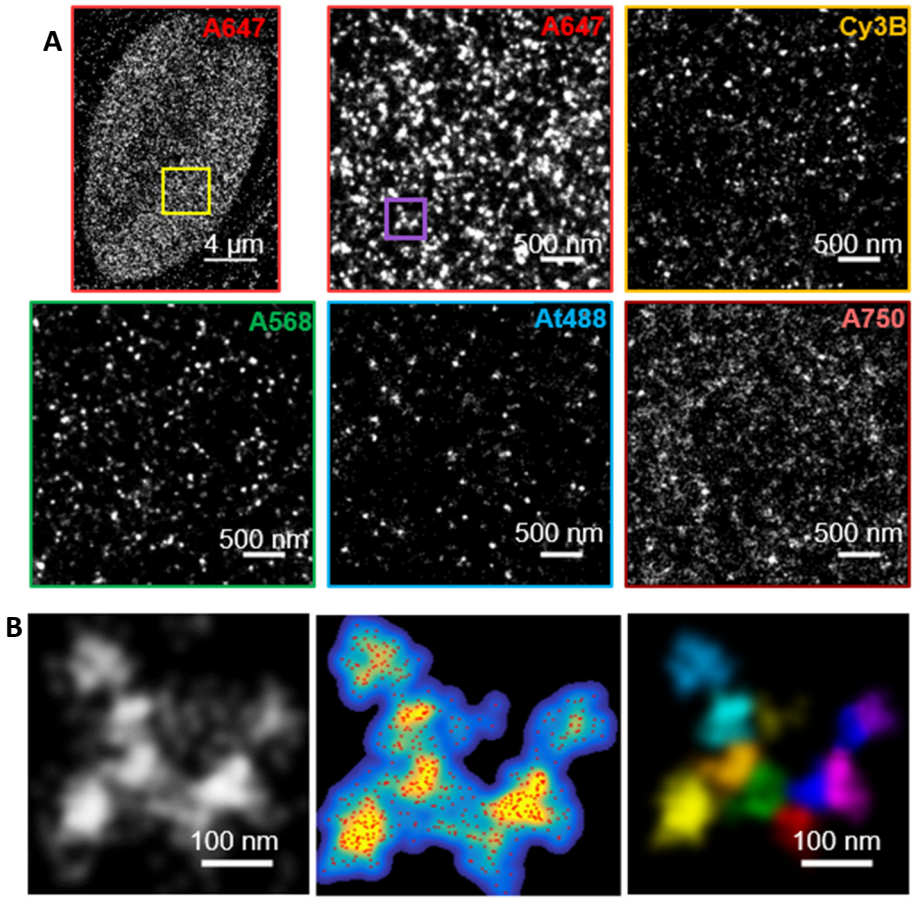

Figure 20. 2D super-resolution imaging of H2B with alternative super-resolution compatible dyes. (A) Representative 2D super-resolution images of the histone H2B obtained using fluorophores AlexaFluor647 (zoom up of the region inside the yellow square), Cy3B, AlexaFluor568, Atto488 or AlexaFluor750. **(B)** (left) Zoom up of the region inside the purple square, (middle) Gaussian-based rendering of the same region as a density image from low (cyan) to high (yellow) density and the super-resolution localizations (red), (right) Result of the cluster analysis, each cluster identified using the cluster analysis is color-coded with a different color. In some cases, colors repeat such that distinct clusters may by chance have the same color. We refer to the group of clusters that are in close proximity as “islands” of clusters.

As it can be observed in **(Figure 20A)**, when labelling H2B with Alexa 647, we obtained an image with high density of signal in which the localizations are grouped in clusters, termed “clutches”. Detailed analysis of these data showed that most fluorophores gave rise to sparse appearance of the clutches in the rendered images compared to those obtained by AlexaFluor647 **(Figure 20A)**.

Nucleosome clutches in STORM images of AlexaFluor647 typically cluster together, with multiple clutches in close spatial proximity of one another (**Figure 20B**), likely corresponding to the higher order folding of the chromatin fibre. We refer to these nucleosome-clutch-rich regions as clutch “islands”. The presence of these clutch islands is consistent with recent super-resolution imaging of single chromosomes, showing multiple DNA nanoclusters in close proximity (Fang et al., 2018).

By comparison, when labelling with other fluorophores, we obtained a sparse image with less localizations and less number of clutches. These clutches in turn do not clearly form islands.

The chromatin inside of the nucleus is a dense, non-regular structure. As we have discussed in Chapter 1.5 of the introduction, this particular case demands high density of signal and high localization quality in order for the structure to be resolved. Furthermore, the structure is thick and away from the glass bottom in the plate where the cells are cultured. As such, achieving a high signal-to-noise ratio during raw data acquisition becomes critical. Although the photophysical properties of other photoswitching dyes are enough to label regular structures such as microtubules, they do not reliably report chromatin structure.

4.3 PAINT allows efficient chromatin imaging

To circumvent the problem of sparse localizations, we used a different localization based-imaging modality, DNA-PAINT, referred here simply as PAINT for clarity. As we have introduced on Chapter 1.2.3 of the introduction, PAINT does not rely on the use of imaging buffers and fluorophore photoswitching.

Instead, the on-off blinking of fluorophores is achieved by the transient, reversible binding of fluorophore labelled “imager oligo strands” to the complimentary “docking oligo strands”. The docking strands are conjugated to a secondary antibody (Schnitzbauer et al., 2017), which is used for immunostaining and hence imaging a target protein. Due to the independence from photoswitching, a wide range of fluorophores can be used for PAINT imaging. Our results showed that PAINT gave rendered super-resolution images of H2B that were qualitatively comparable to those obtained by STORM imaging using AlexaFluor647 (**Figure 21**).

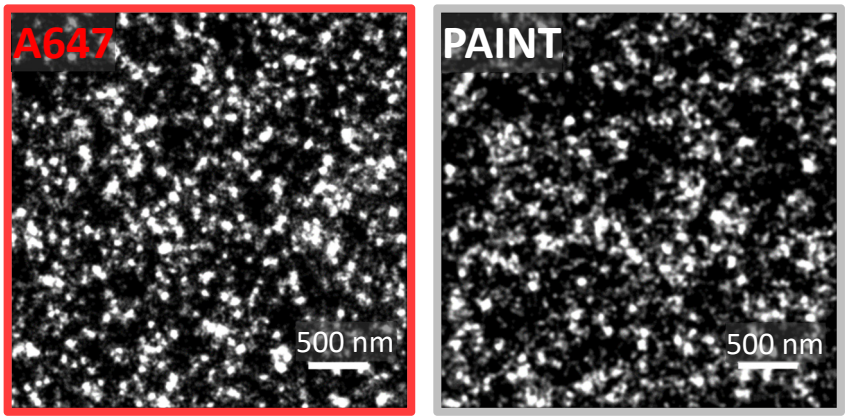

Figure 21. 2D super-resolution imaging of H2B using DNA PAINT. Representative 2D super-resolution images of the histone H2B obtained using fluorophores AlexaFluor647 (left) versus PAINT super-resolution imaging (right). PAINT was performed exclusively using a dye excited by 560 nm laser light

In order to quantitatively compare the super-resolved data, the histone localizations of all the tested dyes were analysed using our previously developed distance-based cluster identification algorithm and the localizations were segmented into nucleosome clutches for comparison (Ricci et al., 2015) (**Figure 20B**).

We found that the nuclear area occupied by fluorophore localizations was significantly lower for Cy3B, AlexaFluor568, Atto488 and AlexaFluor750 compared to AlexaFluor647 (**Figure 22A**). By comparison, the area occupied by localizations for PAINT was significantly higher than Alexa647, probably due to the fact that PAINT localizations do not exhaust due to fluorophore bleaching.

Furthermore, nucleosome clutches imaged with alternative fluorophores were mostly isolated in space, having significantly fewer neighbouring clutches and hence did not form clutch islands (**Figure 22B,C**). In both cases, Cy3B and PAINT exhibited the most similar behaviour to that of Alexa 647.

Ultimately, these results can be attributed to the localization density per frame achieved, which was substantially higher for AlexaFluor647 and PAINT, giving rise to a much higher cumulative number of localizations in the same image acquisition time compared to other fluorophores (**Figure 23A**). Accordingly, the final image resolution computed using the Fourier Ring Correlation (FRC) analysis (Banterle et al., 2013) (**Figure 23B**) was significantly improved for super-resolution images of histones acquired using AlexaFluor647 and PAINT when compared to other fluorophores (**Figure 23C**).

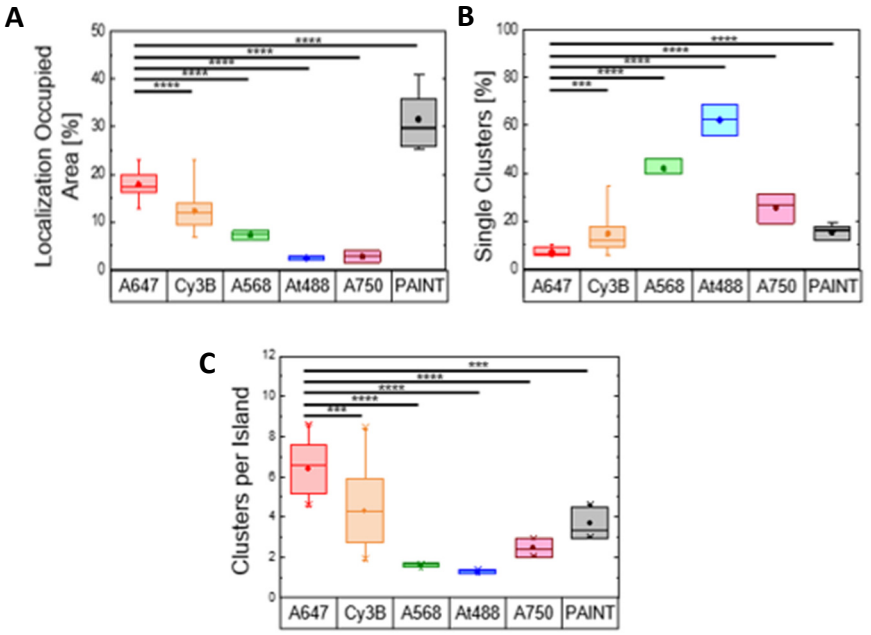

Figure 22. Quantitative comparison of clusters between different super-resolution dyes. **(A)** Percentage of nuclear area occupied by localizations in super-resolution images of H2B recorded using different fluorophores or PAINT super-resolution imaging. The occupancy was calculated by first binning localizations into grids having either a 20 nm super-resolved or a 160 nm diffraction-resolved pixel size. Then the ratio of the summed area occupied with the 20 nm size to the summed area occupied with 160 nm size was calculated and converted to percentage. **(B)** The percentage of isolated, single H2B clusters (i.e. clusters identified to be the only cluster within an "island" relative to the total number of H2B clusters identified following cluster analysis of SMLM image data using different fluorophores or PAINT. **(C)** Number of clusters per "island" (Figure 3B) in super-resolution images of H2B recorded using different fluorophores or PAINT. For box plots in panels A-C, the box indicates the 25-75th interquartile ranges, the horizontal bar shows the median, the central dot indicates the mean and the whiskers are the min/max values. Stars indicate statistical significance according to an unpaired One-way Anova with Multiple comparison test against A647.

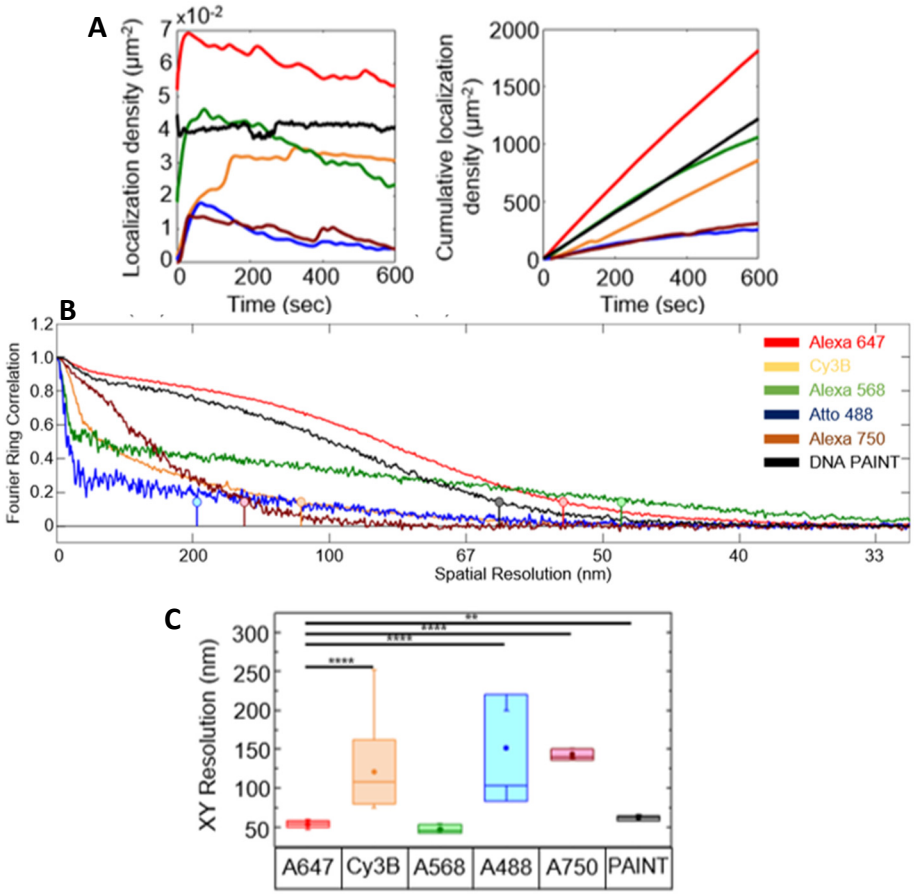

Figure 23. Quantitative comparison of localization density and resolution between different super-resolution dyes. (A) (left) Number of localizations per unit area in each frame or (right) cumulative number of localizations per unit area over time during acquisition of raw SMLM image data. H2B was imaged with different fluorophores in STORM or PAINT techniques and the aforementioned localization densities are plotted for a time duration of 600 s. **(B)** Fourier correlation ring (FRC) analysis (Banterle et al., 2013) of the spatial correlations computed from the H2B super-resolution images obtained using different fluorophores in STORM or PAINT SMLM imaging techniques. **(C)** Box plot showing the final image resolution in nm computed from the FRC analysis for each fluorophore or PAINT imaging. The best resolution was obtained for AlexaFluor647, AlexaFluor568 and PAINT. However, AlexaFluor568 gave rise to sparse images (see Figure 24 above) in agreement with its FRC plot that shows little long-range structural information in contrast with the AlexaFluro647 and PAINT curves.

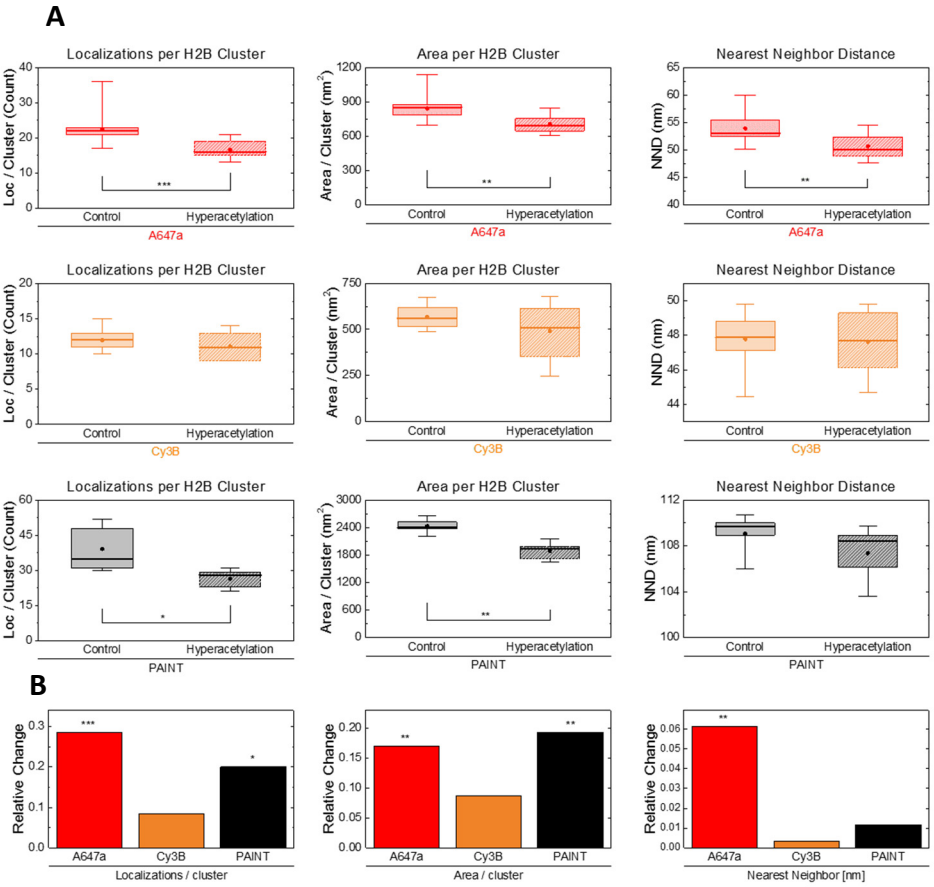

Figure 24. Paint recapitulates changes upon clutch parameters upon hyperacteylation. (A) Number of localizations per cluster, area per cluster and Nearest Neighbor Distance measured from super-resolution images of H2B recorded using AlexaFluor647 (top), Cy3B (middle) and PAINT super-resolution imaging (bottom) in normal and hyperacetylated conditions. **(B)** Comparison of relative change upon hyperacetylation for localizations per cluster, area per cluster and Nearest Neighbor Distance between Alexa647, Cy3B and PAINT super-resolution imaging. Stars indicate statistical significance according to an unpaired t-test.

Importantly, we verified the reliability of the histone nano-structure obtained via PAINT by reproducing our previous biological results obtained using Alexa647-STORM, in which clutch size and the number of localizations per clutch decreased after TSA treatment (**Figure 24**). We also used

Cy3B to try to report those changes, as it was the photoswitching fluorophore from which we obtained the best results. We could recapitulate the trends observed in our previous publication with PAINT microscopy, but were unable to do so when imaging H2B using Cy3B.

Taken together, this results show that PAINT images are quantitatively comparable to those obtained by STORM imaging using AlexaFluor647, demonstrating the equivalency of the two imaging modalities.

4.4 Development of a dual-color super-resolution microscopy method capable of reconstructing the DNA and the chromatin

In order to combine the two-super resolution modalities for multi-color STORM imaging, we had to design an experimental workflow that accounted for the differences in imaging acquisition requirements.

Often, when performing dual color microscopy with spectrally separated dyes, the buffer requirements for optimal fluorophore performing are different, and a compromise has to be reached. Luckily, PAINT does not require a particular oxygen scavenging system or particular concentration of reducing agents such as MEA. Hence, they can be readily combined without any drastic alterations to the imaging buffer.

The main caveat was the different acquisition times necessary for each modality. While STORM frames are taken with an exposition of 9-20ms, PAINT frames are taken with a much higher exposition of 100-300 ms (Blumhardt et al., 2018; Schnitzbauer et al., 2017). This longer exposition is needed in order to obtain a PSF from photon accumulation when the imaging strand is immobilized. Use of shorter exposition times

decreases the amount of photons. As such the threshold for identifying localizations is lower and a significant amount of noise is recognised as false positive localizations (**Figure 25A**).

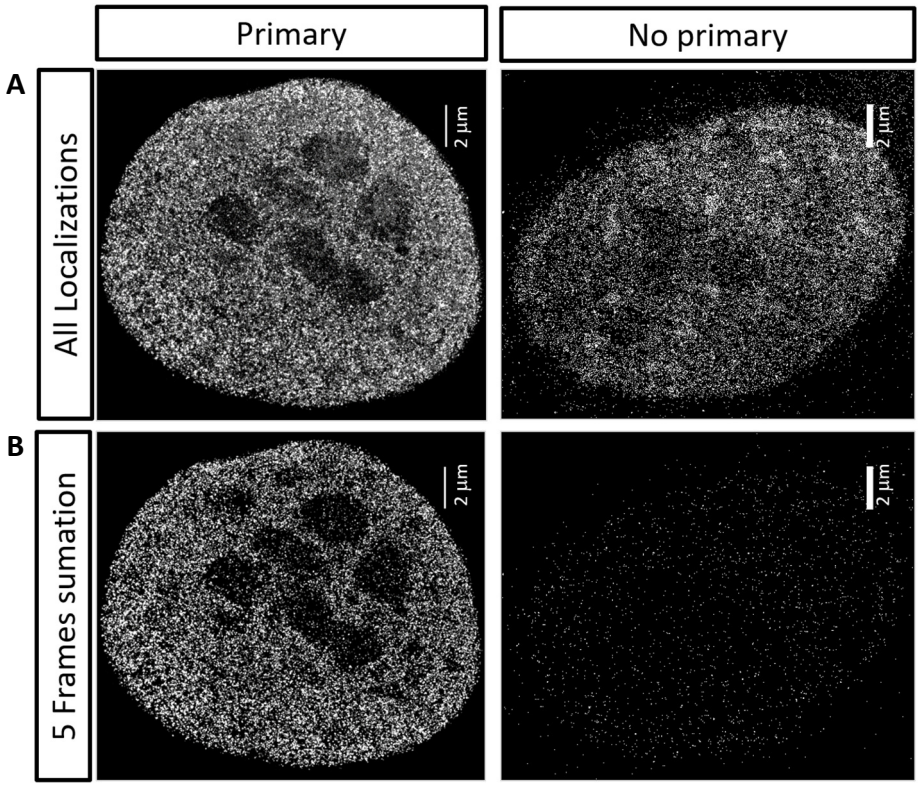

Figure 25. 20ms frame summation of PAINT images allows obtaining high signal to noise ratio super-resolved images. (A) H2B signal (left) and no primary negative control (right) super-resolved PAINT images of human fibroblast nucleus obtained analysing images with a 20ms exposition regime. **(B)** H2B signal (left) and no primary negative control (right) super-resolved images of the same data-set, obtained after summation of each 5 consecutive frames to obtain frames equivalent to 100ms exposure. Although we understandably obtained less localizations in the positive control, the number of localizations in the negative control was drastically reduced.

To account for this difference in acquisition time, we obtained 20ms exposition images of PAINT data. Each five sequential images were summed together to obtain an effective 100ms exposure, from which we obtained our localizations. The number of localizations obtained when performing the summation was reduced in all cases, but it dropped drastically in the negative control **(Figure 25B),** proving that summation was a viable method to obtain PAINT data.

Once proven that the frame summation was a viable approach, we developed a method in order to simultaneously combine PAINT and STORM microscopy **(Figure 26)**. The use of a beam splitter allowed us to split the image on the full chip of the camera based on emission wavelength. 647 nm laser was used to excite the DNA labelled with AlexaFluor 647. Simultaneously, 560 nm laser was used in order to perform PAINT. The 405 laser was used for reactivating AlexaFluor 647 during acquisition. Finally, the 488 laser was used to illuminate fiduciary used for drift correction and chromatic alignment **(Figure 26A).** STORM localizations of DNA structure in the red 647 nm channel were overlaid with PAINT localizations of histone structure in the orange 560 nm channel.

Raw STORM+PAINT image data was obtained, recording frames with 20ms camera exposure. Red-channel STORM localizations were extracted from the 20ms images. For the orange channel PAINT localizations, five sequential image frames were first summed together to obtain an effective 100ms camera exposure, then the localizations were extracted from these summed frame images **(Figure 26B)**. This approach can be combined with a cylindrical lens in order to obtain 3D data.

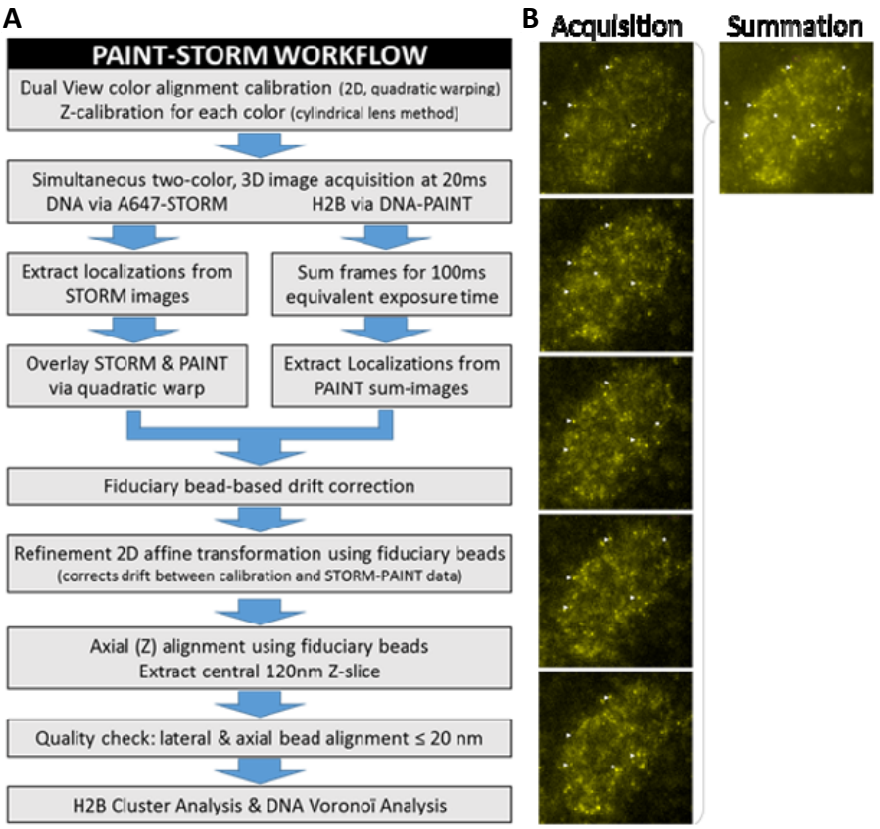

Figure 26. Simultaneous 3D dual-color acquisition of SMLM data combining STORM+PAINT imaging modalities. **(A)** Schematic of acquisition and data overlapping. **(B)** Representative raw data images of PAINT acquisition, before and after summation. Stars: examples of localizations identified in the 20ms movie not identified in the summation. Arrows: examples of localizations identified in the summation frame.

All orange-channel localizations were first overlaid upon the red channel localizations. Next, bead localizations in each color were grouped into bead-clusters and used to extract and correct the drift trajectory for each color throughout data acquisition **(Figure 27A).**

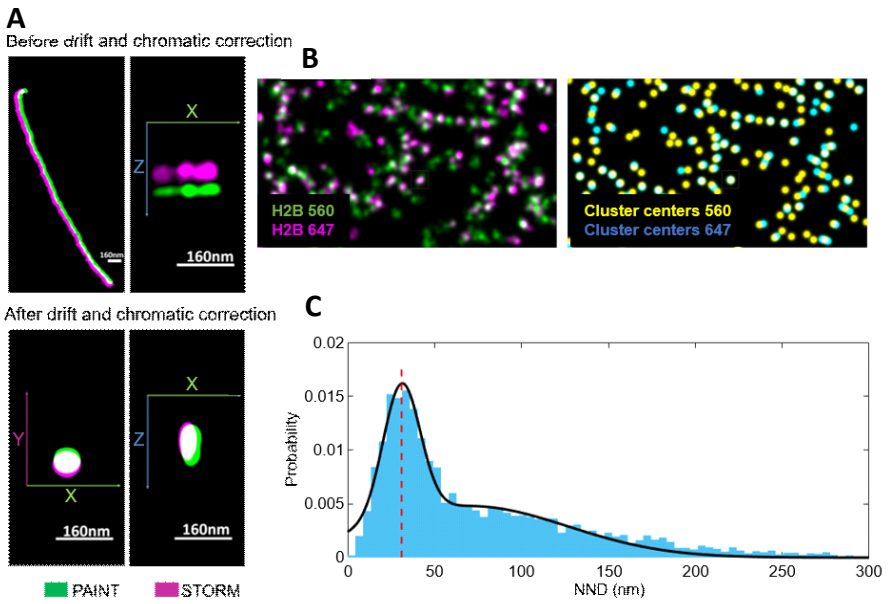

Figure 27. 2-color, 3D DNA, H2B super-resolution imaging workflow and alignment. (A) A rendered image of the localizations corresponding to a fiduciary bead before (upper) and after (lower) drift correction and 3D alignment. **(B)** H2B co-imaged by PAINT with the same secundary antibody but two spectrally separated imager strands. (Left) H2B super resolution signal. A large portion of H2B clusters appeared in both color channels (green for 560 nm excitation and magenta for 647 nm excitation) (Right) Centroid of H2B clutches after cluster identification. Some segmented clusters only appeared in one color channel likely due to competition between the imaging strands for the same docking strand oligo during the finite time of image acquisition. **(C)** The distribution of nearest neighbor distances (NND), calculated between cluster centers in 3D, appeared bi-modal and was fit with a summation of two Gaussian functions (thick, black line). The right-most distribution covering the broad tail corresponds to the clusters appearing in only one color and is centered at 70 nm with a spread of 80 nm. The left-most distribution covering the large peak corresponds to clusters identified in both channels and is centered at 31 nm with a spread of 15 nm. We take this left-most distribution to represent the residual alignment error between DNA and H2B structure in our STORM-PAINT data registration workflow.

Following drift correction of the datasets, the fiduciary bead positions were used to refine the lateral alignment of the two datasets in *x* and *y* using a linear affine transformation **(Figure 27A).**

Once aligned, a 120 nm slice centered near the imaging focal plane (*i.e.* Z=0) was selected for further co-structural analysis. This workflow was automated using functions developed in MATLAB version 2013a and 2016a. For further explanation of the method, see Chapter 10.6 of Materials and Methods.

To measure the residual registration error of the method in order to prove that overlapping with nanometric precision was possible, we imaged H2B via PAINT in two colors simultaneously (560 nm and 647nm laser excitation) to obtain two-color images of the same histone structure **(Figure 27B)**. H2B was labeled with primary antibodies followed by PAINT-compatible secondary antibodies, which were covalently linked to a single docking strand oligo.

Although this technique was developed to co-image DNA and histones, it can potentially be combined to image any two possible species when other, simpler two-color SMLM methodologies prove inefficient or unviable. Particularly, we have also used it to obtain two-color SMLM data from RNA+Pol II and RNA+H2B, as described in Chapter 6.

5. SUPER-RESOLUTION MICROSCOPY REVEALS HOW HISTONE TAIL ACETYLATION AFFECTS DNA COMPACTION WITHIN NUCLEOSOMES IN VIVO

5.1.-Global DNA compaction decreases in cells with histone tail hyperacetylation

Building from our previous work (Ricci et al, 2015) we imaged the DNA distribution of human Fibroblasts (hFB) in order to quantitatively characterize DNA local density distribution and nano-structure within the nucleus with a 20 nm resolution.

Super-resolution microscopy allows us to obtain precise quantitative information of the DNA structure. Based on our approach, described in Chapter 4.1, the fluorophore is covalently linked to the DNA, reducing the physical distance between the species of interest and the fluorophore when compared with other, antibody based approaches. This, coupled with a high label density, allows us to visualize the organization features in the nucleus.

Fixation of the cells and click chemistry with AlexaFluor647 allowed 3D super-resolution imaging of DNA structure (**Figure 28A, upper**). We assessed the localization density in the super-resolution images using a Nyquist sampling (Legant et al., 2016) criterion and selected those having a sampling frequency of 32 nm/localization or lower for analysis (see Methods 10.11 for details). This initial filter ensured that the cells analyzed had a high level of EdC incorporation, high labeling density and hence high spatial resolution of the resulting DNA STORM image.

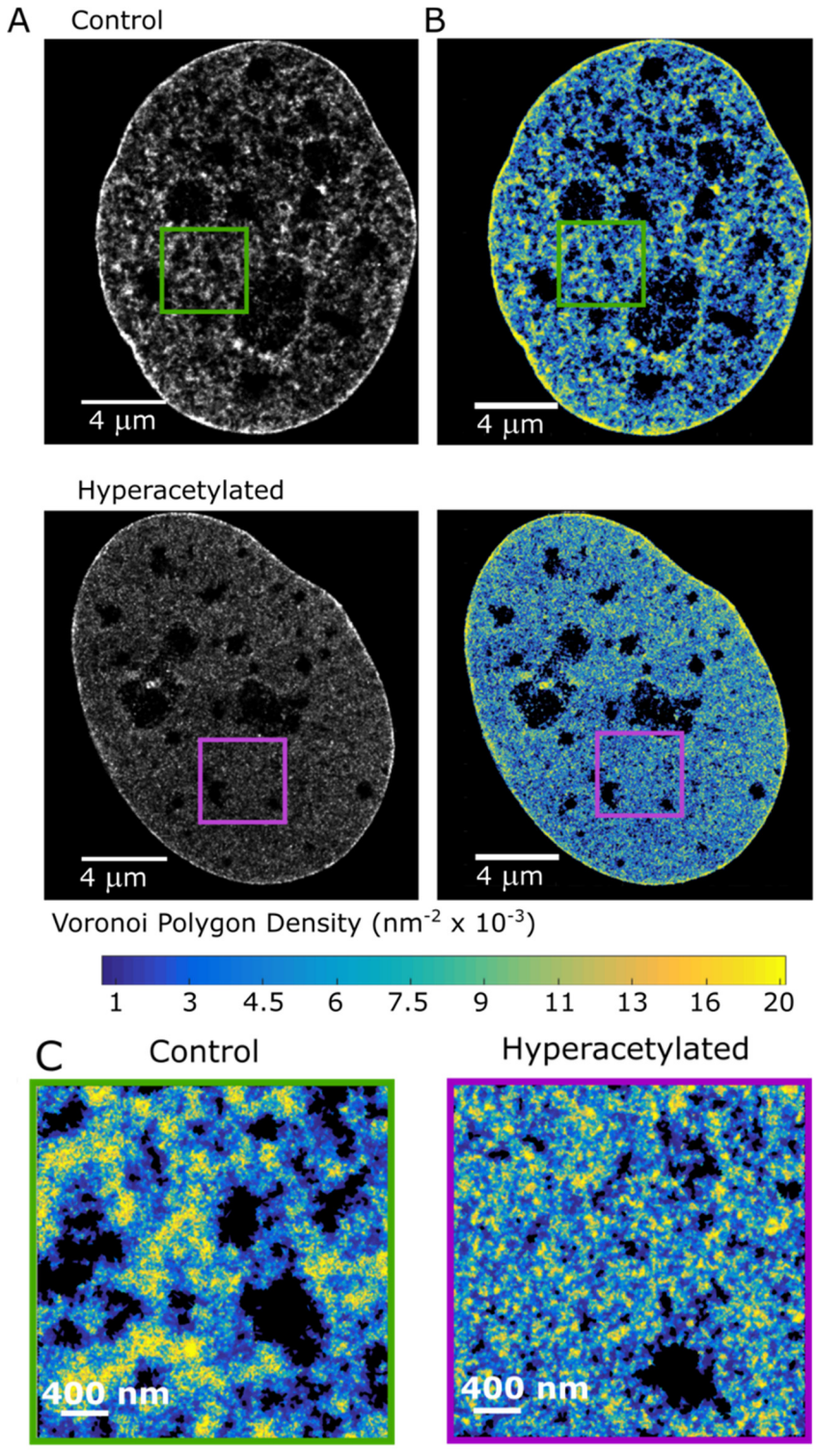
A
Control
B
4 µm
4 µm
Hyperacetylated
4 µm
4 µm
Voronoi Polygon Density (nm-2 x 10-3)
1
3
4.5
6
7.5
9
11
13
16
20
C
Control
Hyperacetylated
400 nm
400 nm

Figure 28. EdC labeling enables super-resolution imaging of DNA structure. (A) Cropped nuclear super-resolution images of EdC labeled DNA in control (upper) and TSA-treated (lower) human BJ fibroblast cells. **(B)** Super-resolution Voronoi tessellation image of DNA in control (upper) and TSA-treated (lower) fibroblasts. Voronoi polygons are color-coded according to the density (inverse of the polygon area) following the color scale bar (from 0.02 nm^2 in yellow to 0.001 nm^2 in blue; the largest 0.5% of the polygons are colored black). **(C)** A zoom up of the region within the squares in (B).

Next, we employed a new quantitative approach based on Voronoi tessellation to analyze DNA spatial organization. Previous methods used for analysis of chromatin structure include statistical analysis methods such as Ripley's K and pair correlation function or segmentation methods such as k-means or density based clustering (Cisse et al., 2013; Endesfelder et al., 2013; Fang et al., 2018; Ricci et al., 2015).

Ripley's K type statistical analysis methods produce only an average estimate of the length scale of spatial correlations in the image without any information on heterogeneity and the local spatial context of the density distribution. Clustering methods, on the other hand, are only suitable for segmenting small nanodomains of roughly uniform size and fail when the image contains a mixture of structures with varying length scales. Moreover, there is no *a priori* reason to limit analysis to clustered DNA structure.

To circumvent the limitation of these previous methods and analyze DNA density distribution within the nucleus in an unbiased manner, we took advantage of Voronoi tessellation (see Materials & Methods, Chapter 10.8) (Andronov et al., 2016; Levet et al., 2015) . Voronoi tessellation can directly determine the local, precise density in the proximity of each localization in the super-resolution image without imposing a

box-size, a search radius or other user-defined parameters (Aurenhammer, 1991; Voronoi, 1908), unlike other methods including Ripley's K function.

To our knowledge, our work is the first example of Voronoi analysis applied to segment and quantitatively characterize DNA local density distribution and nano-structure within the nucleus.

To this end, super-resolution images of DNA were segmented using Voronoi tessellation (Andronov et al., 2016; Levet et al., 2015) and color coded according to the inverse of the area of Voronoi polygons (**Figure 28B and 28C**). The Voronoi polygon area is inversely related to DNA density, with higher density regions corresponding to smaller Voronoi polygons and vice versa.

Although localizations were extracted in 3D **(Figure 29A),** the analysis was performed on a 2D projection of a thin, 120 nm slice through the center of the nucleus, which contained approximately 33% of all localizations (**Figure 29B**). The 120 nm z-thickness was selected so as to include a sufficiently high density of localizations for structural analysis while minimizing 2D projection effects that can arise when imaging over the 600-800 nm range accessible in the STORM technique. This volume is also in a similar range as recent electron tomographic reconstruction of DNA organization (Eltsov et al., 2008; Ou et al., 2017).

Compact, heterochromatic regions typically located at the nuclear edge and surrounding the nucleoli in human fibroblasts were characterized by high DNA density in the super-resolution images (**Figure 28B, upper**), suggesting that DNA density is indeed a quantitative measure of chromatin compaction and presence of heterochromatin.

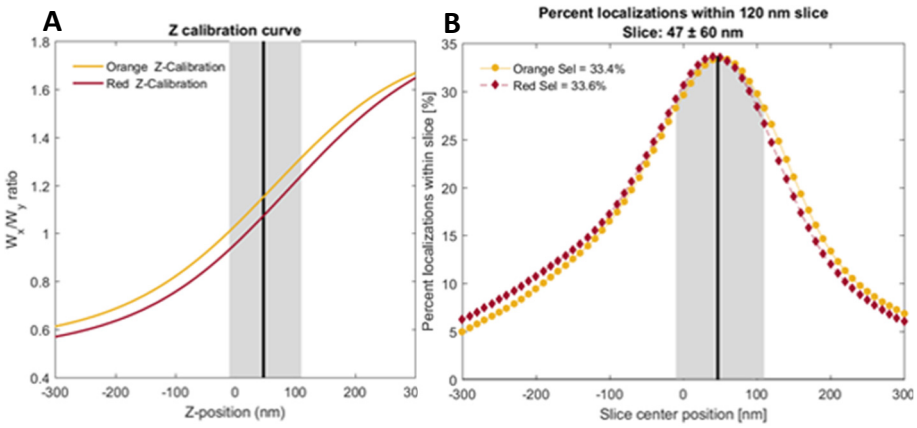

Figure 29. 3D data selection. (A) Calibration curve for PSF elipsicity (measured as width in x/ width in y) versus its relative z-position to the focal plan for both orange and red colors**. (B)** Percentage of localizations as a function of the z-position from the central focal plane (at 0) for two-color datasets following axial registration. The orange and red dots correspond to the two color-channels for H2B and DNA, respectively. The light grey area under the distribution indicates the 120 nm thick z-slice used for the analysis, which encompassed ~33 % of localizations for both color channels across all datasets.

Treatment with the Histone Deacetylase (HDAC) inhibitor Tricostatin A (TSA) has been shown to lead to hyperacetylation of histone tails, chromatin opening and increased transcriptional activity (Toth et al., 2004). We therefore treated cells with TSA during the final 24 hours of EdC incubation and labeled them with click chemistry as before to quantitatively compare global DNA density of control and hyperacetylated cells.

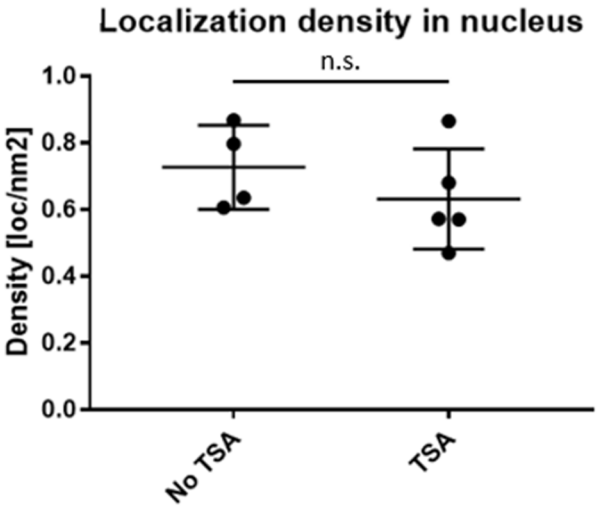

Figure 30. Global DNA density remains unchanged after TSA treatment. Localization density in nucleus measured as total number of localizations in the analyzed nuclear regions per total area of the region. P-value>0.3 according to unpaired t-test.

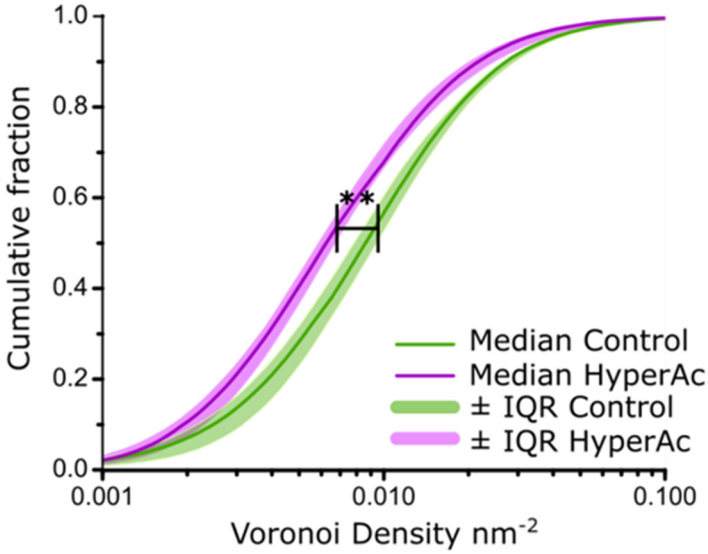

Figure 31. Voronoi tessellation allows quantitative measure of DNA distribution. Cumulative distribution of the Voronoi Polygon densities in control (green) (N=6 cells) and TSA-treated (magenta) (N=9 cells) fibroblasts. The light colors show the interquartile range (25-75 percentiles) and the thick, dark lines show the median values; stars indicate statistical significance of the separation between the median of the medians according to Kolmogorov Smirnoff test with p = 0.0022.

The EdC labeling efficiency, measured as the number of fluorophore localizations detected per unit cell area, was unchanged between control and TSA treated cells **(Figure 30**). Variations on the Voronoi Tesselation distribution should then be attributed to changes on DNA distribution and not changes in the amount of labelled DNA. Voronoi tessellation demonstrated that TSA treatment induced a decrease in the median DNA density (**Figure 31**) consistent with genome wide decompaction of DNA induced by hyperacetylation.

5.2.-Combined PAINT and STORM super-resolution microscopy allows visualization of histone and DNA co-organization at the nanoscale level

Previously, we showed that nucleosomes are organized in heterogeneous groups, which we termed nucleosome clutches, and demonstrated that nucleosome clutch size decreased in TSA-treated human fibroblasts (Ricci et al., 2015).

To gain further quantitative insight into how the DNA is compacted by multiple nucleosomes present within an individual clutch, we aimed to carry out two-color super-resolution imaging of DNA and histone H2B to simultaneously visualize remodeling of nucleosome clutches together with their associated DNA. For that, we combined STORM with PAINT imaging as described in Chapter 4.4.

Two-color super-resolution images of histones and DNA imaged using our developed workflow in control and TSA-treated cells revealed, as expected, a similar pattern of heterogeneous labeling, showing regions enriched in and depleted of chromatin within the nucleus (**Figure 32A,B**), demonstrating that both imaging modalities and labels faithfully represent chromatin structure.

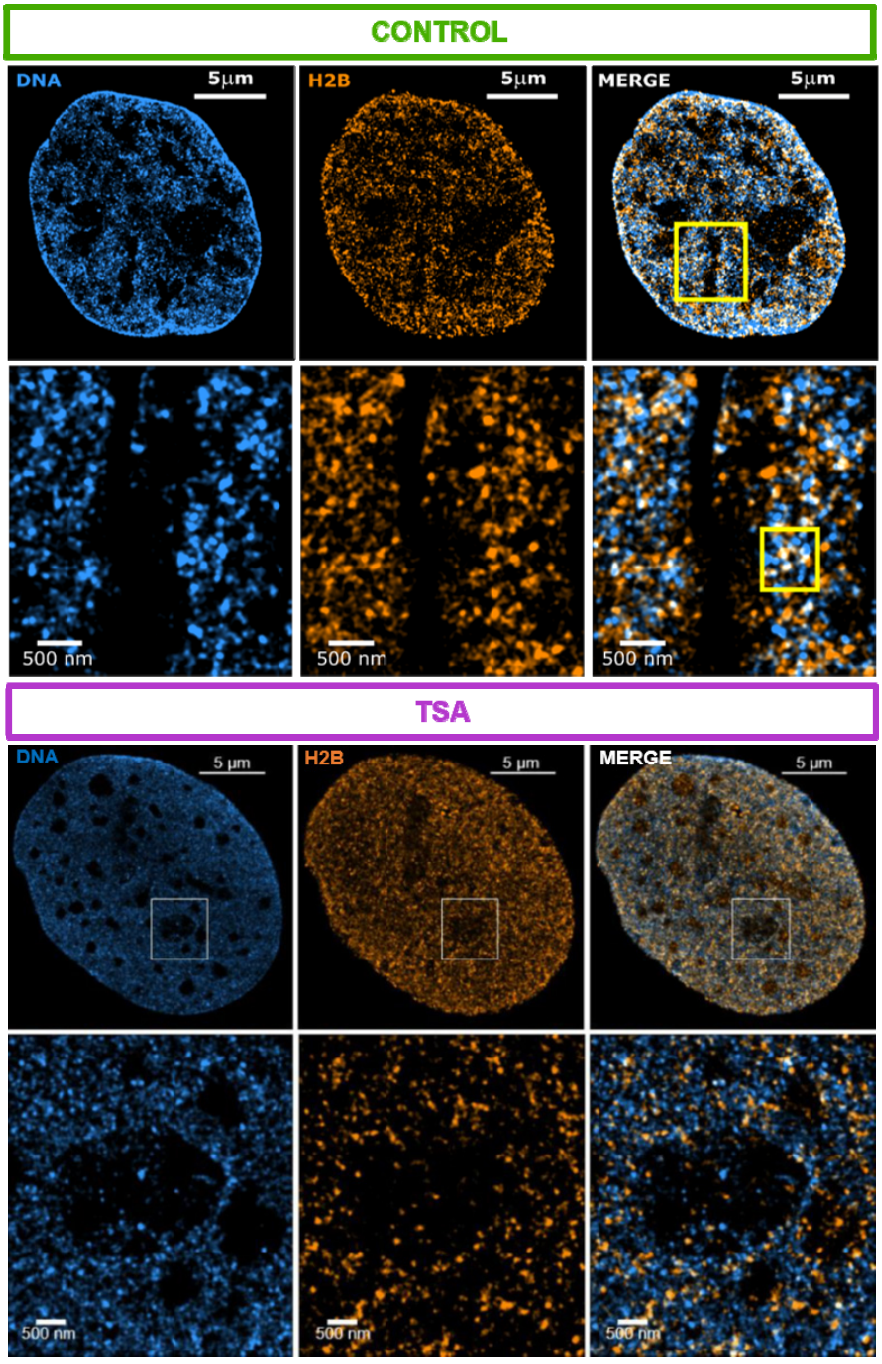

Figure 32. Combined PAINT and STORM super-resolution microscopy allows visualization of histone and DNA co-organization at the nanoscale level. (A) Cropped nuclear super-resolution image in human Fibroblasts of EdC-labeled DNA (cyan)

and PAINT image of H2B labeled with anti-H2B antibodies (orange) and the overlay. A zoom of the region inside the yellow box is shown. **(B)** Cropped nuclear super-resolution image of EdC-labeled DNA (cyan) and PAINT image of H2B labeled with anti-H2B antibodies (orange) and their overlay in TSA treated human fibroblasts. A zoom of the region inside the white box is shown**.**

To further quantify the spatial relationship between histones and DNA, we first segmented the nucleosome clutches using our distance based clustering algorithm (Ricci et al., 2015) and determined their center position. We then once again took advantage of Voronoi analysis by using the center position of each clutch as a seed for the tessellation process. This analysis divided the nuclear space into polygons, each polygon surrounding and belonging to one specific clutch (**Figure 33A,B**).

We next used a circle with a search radius of 120 nm bounded by the Voronoi polygon edges (i.e. if the search radius was larger than the polygon, then the edges of the polygon were used as the boundary) (**Figure 33A,B**) and categorized the DNA localizations falling within the bounded circle as 'clutch-associated' and those falling outside as 'clutch-free' DNA. The 120 nm radius corresponded to about 2.5 times the average standard deviation of the localizations belonging to the H2B clutches, thereby encompassed ~98% of the nucleosome clutch Gaussian-area.

This co-localization analysis, once again, preserves the spatial context and quantitative information about each clutch while defining its area of "influence" in an unbiased way. We found a higher proportion of DNA was nucleosome clutch-associated in control Fibroblasts compared to TSA-treated Fibroblasts (71.7±2.3% in WT Fb and 62.7±2.9% in TSA treated Fb, n=4 and n=5 cells, respectively, (**Figure 34A**) and this trend was consistent and independent of the search radius selected (**Figure 34B**).

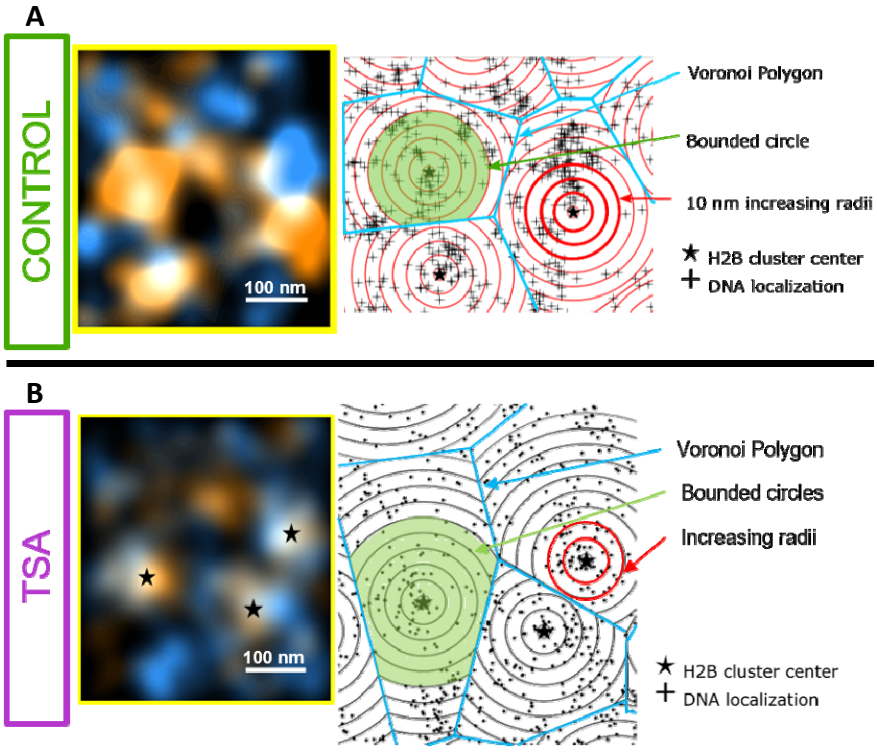

Figure 33. Radial density analysis of DNA localizations according to H2B clutch distribution. (A) (left) Zoom of the region shown inside the yellow square in Figure 16A, **(right)** scheme of the analysis of clutch-bound DNA. The centers of H2B clusters (stars) are the seeds for the Voronoi polygons (blue) inside which the DNA localizations (black dots) are distributed. Overlaid on top are concentric circles whose radii increase by 10 nm steps. **(B) (left)** Representative zoom of a super-resolved region from the cell in Figure 16B, **(right)** scheme of the analysis of clutch-bound DNA. The centers of H2B clusters (stars) are the seeds for the Voronoi polygons (blue) inside which the DNA localizations (black dots) are distributed. Overlaid on top are concentric circles whose radii increase by 10 nm steps

These observations are consistent with the results of our previous polymer based modeling of DNA occupancy from single color images of nucleosome clutches, which predicted a decrease in percentage of DNA occupied by nucleosomes after TSA treatment (Ricci et al., 2015).

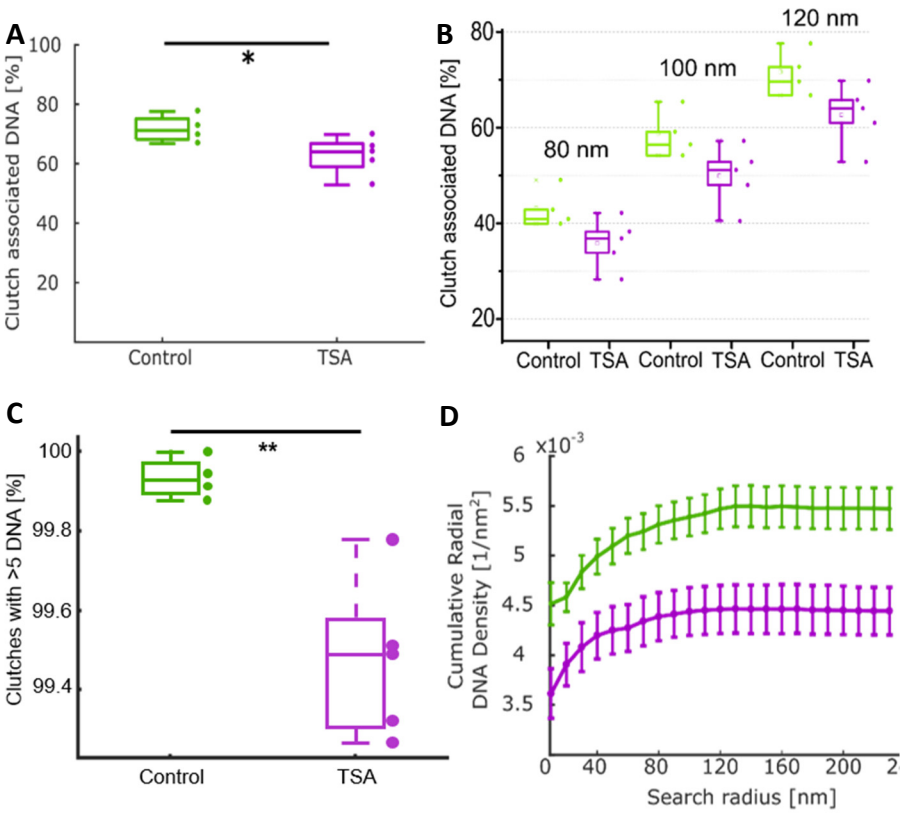

Figure 34. DNA co-localizes with H2B to a lesser extent in TSA-treated cells compared to untreated cells. **(A)** Percentage of DNA localizations associated to clutches in wild-type (N=4, green) and TSA-treated (N=5, magenta) fibroblasts for a circle of radius 120 nm bounded by Voronoi polygons (p-value 0.0441). **(B)** Percentage of DNA associated to nucleosome clutches in control and TSA-treated cells using bound circles with varying search radii. **(C)** Percentage of H2B clutches associated to DNA in wild type (green) and TSA-treated (magenta) cells (p-value 0.0168). **(D)** Cumulative DNA density inside circles of increasing search radii in untreated (green) and TSA-treated (magenta) cells. The dots correspond to the mean, the bars correspond to the standard deviations: the lines connect sequential points and are guides to the eye. Stars indicate statistical significance according to an unpaired two-tailed t-test with Welch correction.

On the other hand, a large percentage of clutches co-localized with DNA in both conditions, 99.9% in control and 99.5% in TSA-treated cells (p-value 0.0168) **(Figure 34C)**. This suggests that most histones within clutches are chromatin associated as expected.

To extract a detailed understanding of how the nucleosome clutches compact DNA associated to them, we next determined the DNA localization density within bounded circles having a range of search radii from the clutch center. Nucleosome clutches in TSA treated cells had a lower DNA density around them compared to control cells over the full range of search radii utilized, indicating decompaction of clutch associated DNA after hyperacetylation (**Figure 34D**).

Since clutches in TSA treated cells are smaller than those in control cells **(Figure 24, Figure 32 and Figure 33**), we questioned whether DNA packs more loosely around small clutches in general. To this end, we quantified DNA density as a function of clutch size in both control and TSA treated cells for bounded circles with a search radius ranging between 30-100 nm (**Figure 35**). This analysis revealed no correlation between clutch size and DNA packing density for both treated and control cells. Therefore, clutches contain an amount of DNA proportional to the number of nucleosomes they contain, and hence the packing density of the total DNA associated with nucleosome clutches is independent of the number of nucleosomes present within them.

Interestingly, the DNA density of clutches at all sizes was lower in TSA treated cells compared to untreated cells (**Figure 34D and Figure 35)**. Therefore, it is the acetylation state of the histones and not the number of nucleosomes within the clutch that determines how tightly clutch-associated DNA is compacted. Acetylation leads to a looser packing of DNA within clutches.

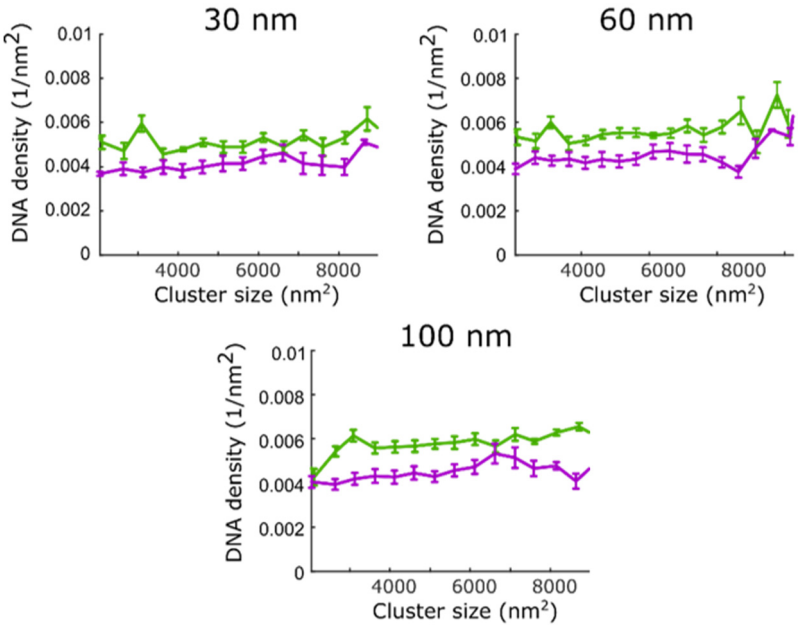

Figure 35. Clutches contain an amount of DNA proportional to the number of nucleosomes they contain. DNA density in a bound circle of increasing size (30-100 nm) versus clutch size measured as area in nm^2. TSA treated clutches (magenta) have lower density than control clutches (green) independently of clutch size**.** The line corresponds to the mean of clusters; the bars correspond to the standard deviations.

To determine the spatial scale where a nucleosome clutch stops influencing the compaction of DNA surrounding it, we set out to quantify the change in local DNA density around the center of nucleosome clutches. We hence determined a "similarity matrix" by comparing DNA density at increasing distances from the clutch center (**Figure 36**). To this end, we first determined the DNA density within 10 nm thick rings of increasing radii (**Figure 33**). The ring radius was increased iteratively by 10 nm intervals while keeping the thickness constant, hence moving the ring away from the clutch center stepwise (**Figure 33**).

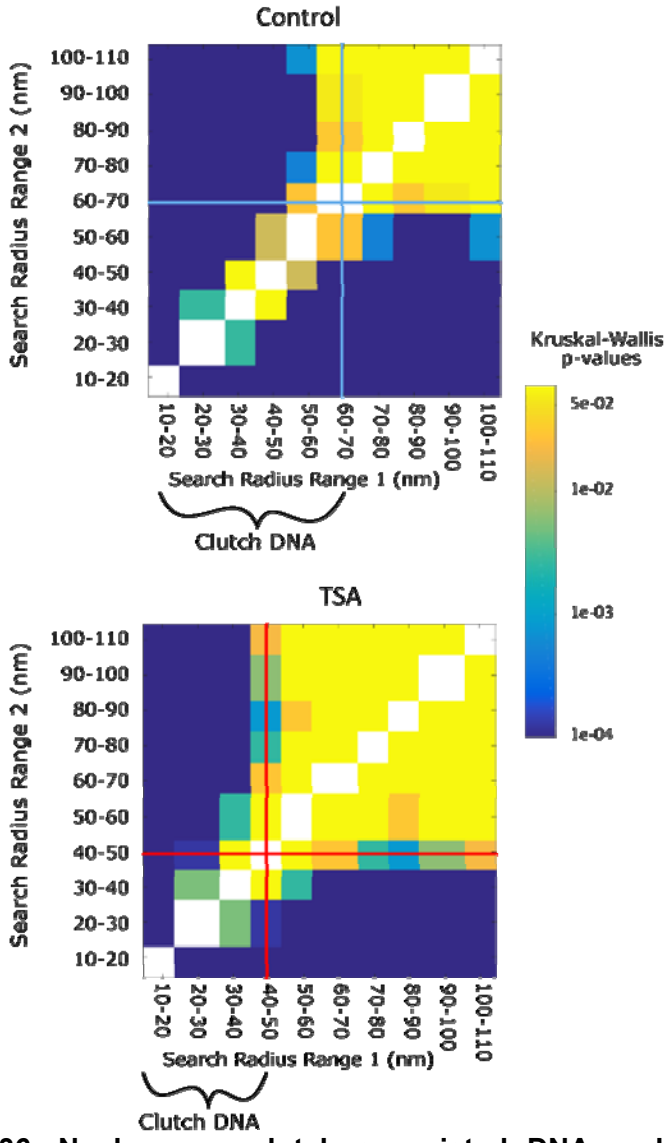

Figure 36. Nucleosome clutch associated DNA undergoes decompaction in TSA-treated cells. Similarity matrix for untreated (left) and TSA-treated (right) cells showing the level of similarity in DNA density within 10 nm discs of increasing radii. The similarity was calculated as a p-value from Kruskalwallis test and is shown as a color coding corresponding to the color scale bar (from p=0.0001 in blue to p=0.05 in yellow). The diagonal was set to white and not calculated. Cyan and red lines show the boundary of a switch from low to high similarity in untreated and TSA treated cells, respectively

We calculated the DNA density within each 10 nm ring from the DNA localizations falling within the ring area and compared it among rings of increasing radii. Similar to pair-correlation analysis, in which correlation drops to random at large distances, we expect high similarity in DNA density at large radii from the clutch center. Our intention was thus to analyze the transition point from low to high similarity at short distances and compare this range between control and treated cells to determine any differences in the scale of DNA packing under these two conditions.

In untreated cells, there was low similarity in DNA densities of rings with radii ranging from 10-70 nm (**Figure 36, left, cyan bars**), suggestive of variation in DNA compaction over this length scale. Search radii above 70 nm, on the other hand, showed high similarity in their DNA density. Therefore, within a 70 nm distance from the clutch center there is large heterogeneity in DNA compaction whereas at larger distances, DNA compaction is unchanged.

These results suggest that nucleosome clutches compact DNA within a 70 nm radius from their center in untreated cells. We call the DNA that falls within the low similarity (high variability) region of the matrix "clutch" DNA: *i.e.* DNA associated to a clutch, which includes both the DNA wrapped around individual nucleosomes as well as the linker DNA in between neighboring nucleosomes. Interestingly, in TSA-treated cells the clutch DNA radius decreased to ~40 nm (**Figure 36,** right, red bars, also compare (**Figure 32A** and **33A** versus **32B** and **33B)**

While the spatial scale of the difference between control and TSA-treated clutch DNA is small (~30 nm) and comparable to our localization precision, this difference is meaningful as our analysis averages over tens of thousands of nucleosome clutches. Such spatial averaging, as also previously

demonstrated (Ou et al., 2017; Szymborska et al., 2013), improves the effective resolution at which we can detect differences in the spatial length scale of clutch DNA in control and TSA-treated cells. Indeed, repeating this analysis with subsets of data points from individual nucleosome clutches clearly demonstrated that the spatial scales of clutch DNA in treated and untreated cells become apparent only when sufficiently large number of clutches are used in the analysis (**Figure 37)**.

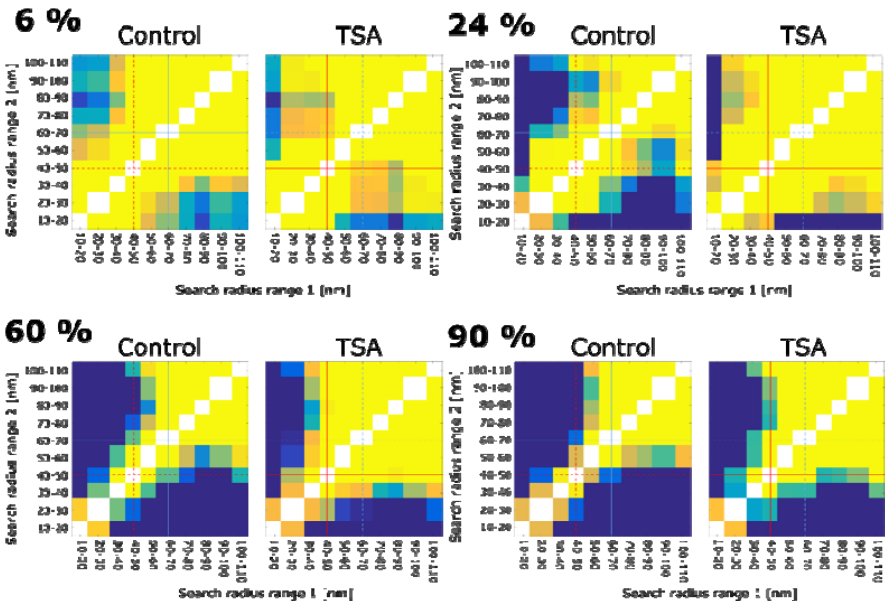

Figure 37. Similarity matrixes generated from sub-sets of data. Similarity matrix for untreated (left) and TSA-treated (right) cells generated by randomly including different percentages of the available clutch data. The matrices show the level of similarity in DNA density within 10 nm discs of increasing radii. The similarity was calculated as a p-value from Kruskalwallis test and is shown as a color coding corresponding to the color scale bar (from p=0.0001 in blue to p=0.05 in yellow). The diagonal was set to white and not calculated. Cyan and red lines show the boundary of a switch from low to high similarity in untreated and TSA treated cells when calculating the similarity using 100% of data, respectively. The proper trend showing the difference between treated and control cells is apparent only when 60% (corresponding to 1079 clutches/cell in control cells and 904 clutches/cell in TSA-treated cells) or more of the clutch data is included in the analysis.

Our combined results suggest that the opening of DNA upon histone hyperacetylation is due to decreased nucleosomal occupancy, as revealed by reduced co-localization between DNA and histones as well as more loose packing of clutch DNA. These results are consistent with previous *in vitro* results, which demonstrated a disruption of histone-DNA interactions in nucleosomes having acetylated tails.

5.3 Clutches in spatial proximity influence each other's DNA packing

In human fibroblasts, clutches are clustered in close spatial proximity of one another, forming "islands" containing several clutches organized into higher order structures, which were hundreds of nanometers in size (**Figure 20B**). We reasoned that these regions might correspond to the higher order folding of the chromatin fiber, bringing multiple clutches into close proximity to further compact DNA.

We next wondered how the DNA packing changes upon hyperacetylation in relation to these folded regions of the chromatin. We compared the DNA density falling within a radius of 70 nm from the clutch center (the clutch DNA for control cells) as a function of the nearest neighbor distances (NNDs) between clutches (**Figure 38**). Surprisingly, the largest difference in DNA density between control and TSA treated cells was observed for clutches having an NND of ~50 nm or smaller (**Figure 38**).

These results suggest that the largest decompaction due to hyperacetylation happens in folded chromatin regions containing high-order structures, where decompacted DNA from one nucleosome clutch may influence the DNA packing of a nearby, neighboring clutch, thus changing the DNA density of multiple clutches. This decompaction might be due to the

presence of a high density of nucleosome tails that become hyperacetylated in these regions, thus generating a large amount of repulsive charges that more strongly disrupt DNA-histone interactions leading to higher DNA decompaction. On the other hand, the more unfolded regions corresponding to more isolated clutches do not undergo major modifications, likely since chromatin in these regions is already in an open state.

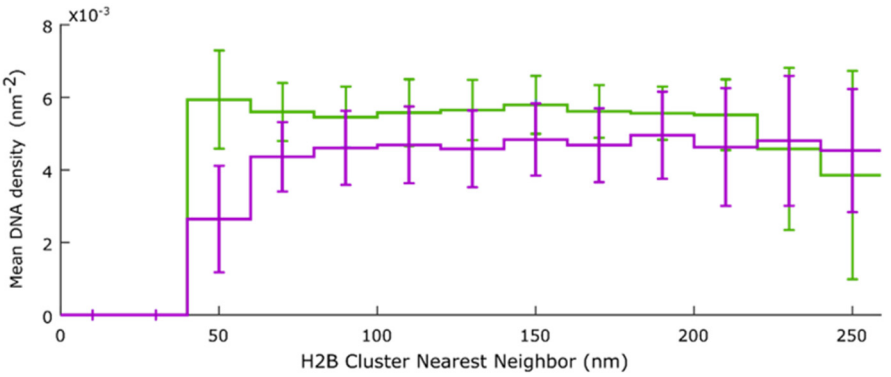

Figure 38. Largest decompaction happens in chromatin regions with closed together clutches. Mean DNA density ± standard deviation as a function of clutch nearest neighbor distance (NND) for untreated (green) and TSA-treated (magenta) cells calculated for a circle of radius 70 nm. The bars show the standard deviation.

6. SUPER RESOLUTION MICROSCOPY REVEALS THE INTERPLAY BETWEEN CHROMATIN AND NASCENT NUCLEAR RNA

6.1 Super-resolved distribution of nascent RNA in the nucleus

As we have discussed in the introduction, there is an interplay between chromatin distribution and transcription. We aimed to study the nuclear distribution of nascent RNA, and how this is related to chromatin nanostructure.

Super-resolution microscopy allows us to obtain precise quantitative information of the RNA distribution. In order to label the nascent transcriptome in an unbiased way, we fed the cells Ethynil-Uridine (EU), a modified nucleotide with an ethynil handle. The EU is intaken by the cell and used by the RNA Polymerases in order to synthetize the new RNA strands (Jao and Salic, 2008).

Thanks to this, by linking a Storm Compatible fluorophore (Alexa 647) to the EU using click chemistry, we are able to obtain single molecule localization information for the RNA positions.

In our images it can be appreciated how the nascent RNA is non-homogenously distributed in all the nucleus (**Figure 39**), with the localizations accumulating in small nanodomains and being excluded in other regions of the nucleus. Both actively transcribed nucleoplasmic and nucleolar regions can be observed, with drastically different RNA distributions **(Figures 39 and 40).** As expected, cells that are not fed EU display a negligible number of localizations (**Figure 39**), ensuring the specificity of our approach.

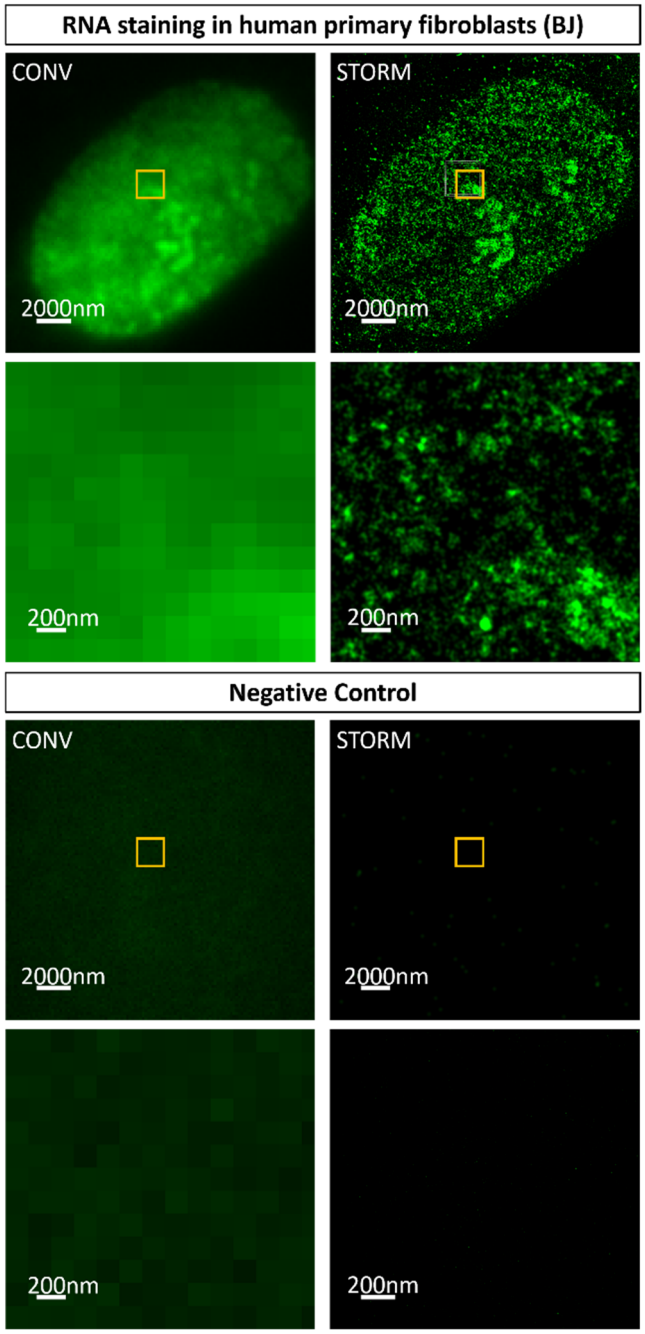

Figure 39. EU labeling enables super-resolution imaging of RNA structure. Nuclear conventional and super-resolution images of click-labeled RNA fibroblasts with a 20 min EU pulse (Upper) and without EU (Lower). Conventional and Super-Resolution zooms of the regions selected in the yellow squares are shown.

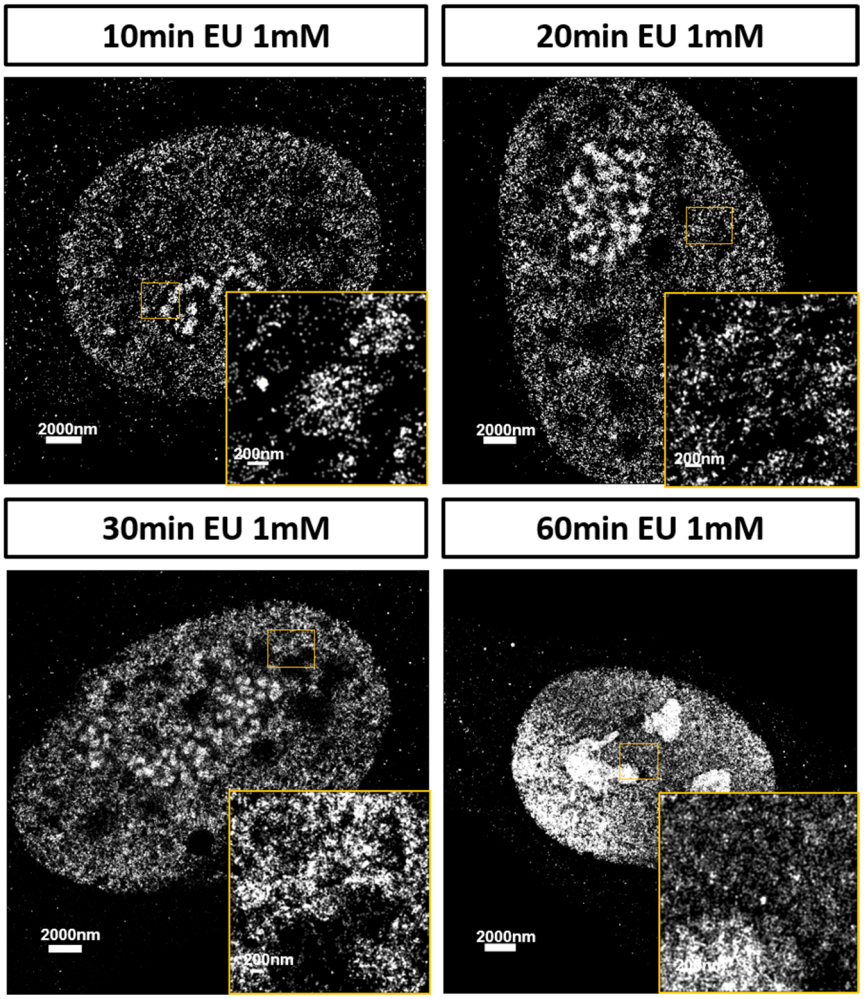

Figure 40. Pulse and chase experiments allows us to label the RNA produced by the cell at different intervals. Super-Resolution images of nascent RNA with 10, 20, 30 and 60 min of EU incubation in human fibroblasts. Zooms of the yellow square regions are shown.

In order to visualize the RNA distribution during the transcription process, we incubated our cells with EU for different times **(Figure 40).** The treatment with EU had no effect on nuclear morphology **(Figure 41C)**. With longer EU incubation times, both the number and the density of localizations increases (**Figure 41A-B**).

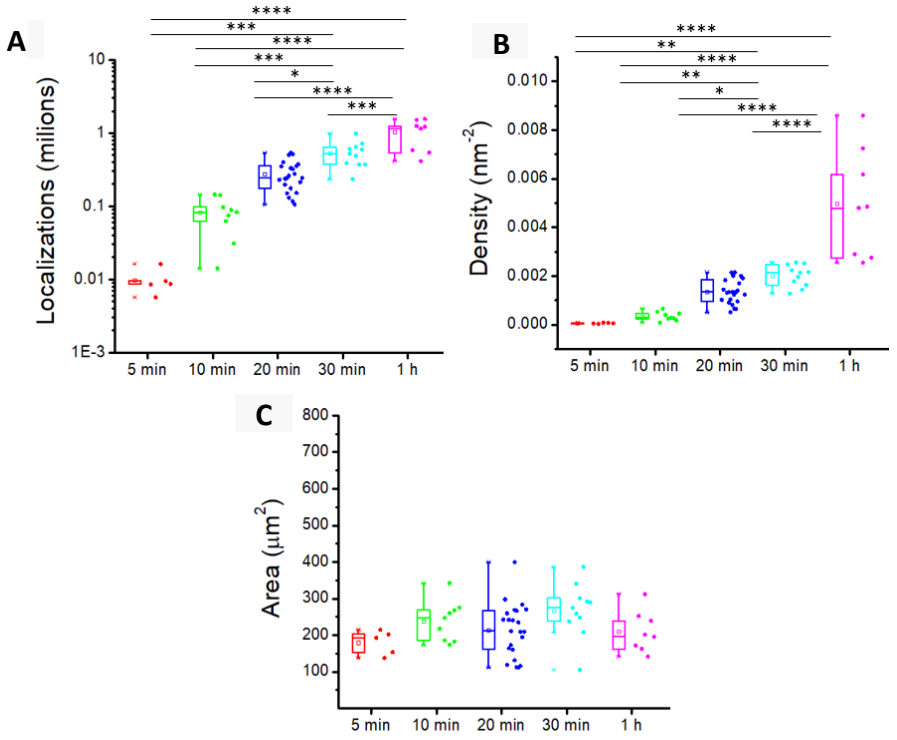

Figure 41. Global RNA quantification. **(A)** Localizations of RNA inside the nucleus of labeled fibroblasts at different times of EU pulse. **(B)** Density in RNA localizations/nm^2 inside the nucleus of fibroblasts at different times of EU pulse. **(C)** Area of the labelled fibroblast nuclei measured in µm^2 at different times of EU pulse. Points represent individual cells. Statistic: Two-tailed One-way Anova with Tukey's multiple comparison test. P-value: *<0.05 , **<0.01 ,***<0.001, ****<0.0001.

Once we determined that we could resolve the distribution of the nascent RNA with nanometric resolution, and that we could see global changes with different transcription time frames, we aimed to quantitatively study it. To this end, super-resolution images of RNA were segmented using Voronoi tessellation **(Figure 42)** (Andronov et al., 2016; Levet et al., 2015). We plotted the inverse of the Voronoi tessels area as a measurement of local density, since the area of the polygons is inversely correlated to the density of the signal. Although we

saw a major difference in the RNA distribution between 10 and 20 min of transcription, there was not a major difference between 30 and 60 min **(Figure 42),** suggesting that after 30 min all the active transcription sites were already fully labelled.

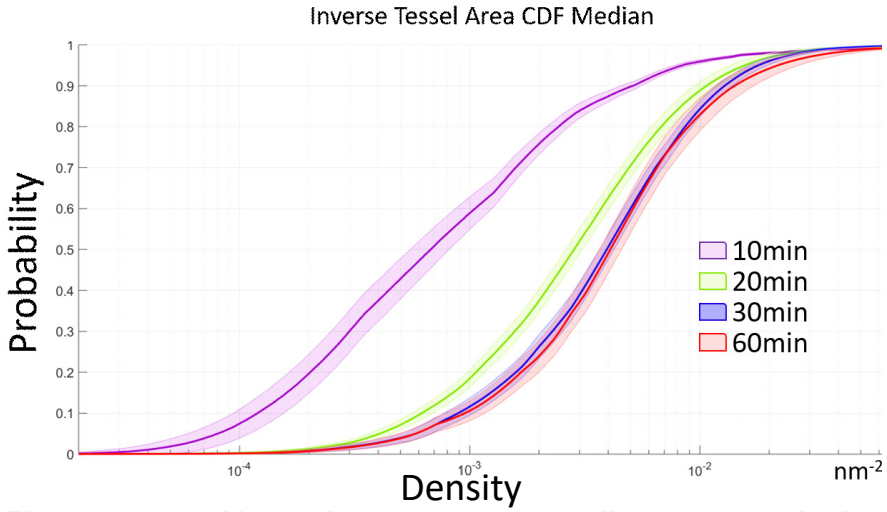

Figure 42. Voronoi tessellation allows quantitative measurement of RNA distribution. Cumulative distribution of the Voronoi Polygon densities with 10 min (purple), 20 min (green), 30 min (blue) and 60 min (red) pulses of EU in fibroblasts . The light colors show the interquartile range (25-75 percentiles) and the thick, dark lines show the median values.

In order to idenfity the nanodomains of active transcription, we performed a density-based clustering based on our Voronoi tessellation analysis, derived from the one described by (Andronov et al., 2016). We defined a treshold of density by intersecting the data with a Monte-Carlo simulation of the same number of localizations homogeneously distributed. All the tessels that had a density higher than the treshold value, together with the neighboring tessels, were defined as clusters **(Figure 43)**. This approach does not impose any constrictions in shape or size to our clusters, allowing to identify a wide variety of domains with drastically different characteristics.

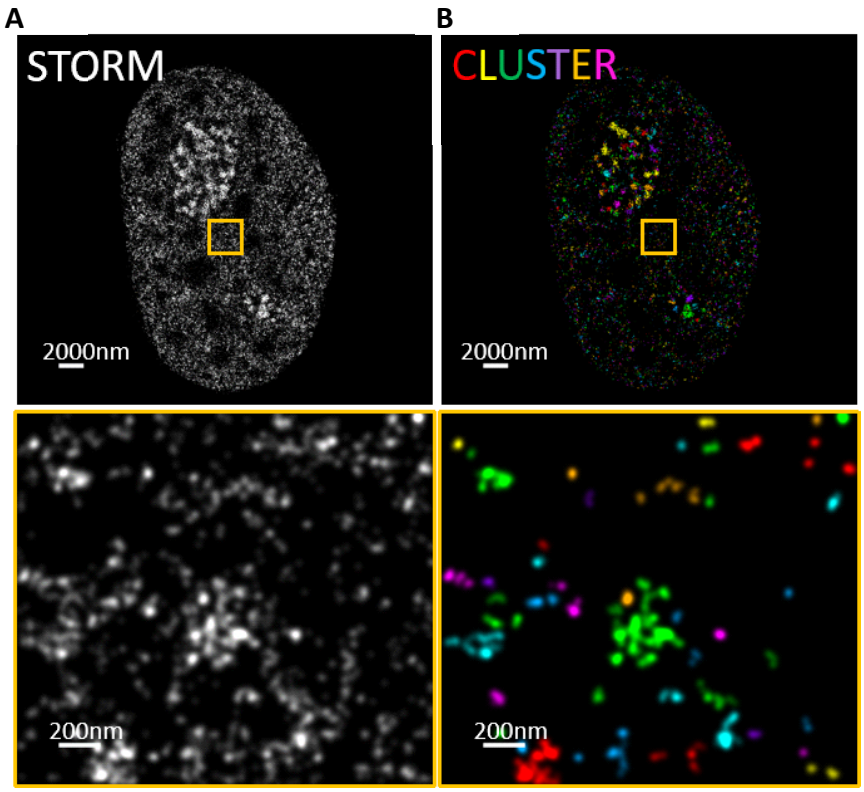

Figure 43.Voronoi-tesselation-based clustering allows us to identify clusters of RNA in fibroblasts. **(A)** (Up) Super resolution imaging of nascent RNA in fibroblast nucleus, (Down) Zoom up of the region inside the yellow square. **(B)** (Up) Rendering of voronoi density cluster analysis; each cluster identified is color-coded with a different color. In some cases, colors repeat such that distinct clusters may by chance have the same color. (Down) zoom up of the region inside the yellow square.

When we quantitatively analyzed the distribution of nanodomains, we saw a drastical increse in the nanodomain density between 10 minutes and longer time points. We found an average of 15.96 clusters/μm^2) in human fibroblasts **(Figure 44A),** in agreement with previous reports (Pombo et al., 1999).

For longer EU pulses, the median cluster area did not change **(Figure 44)**, probably because the vast majority of

transcriptionally active areas had fully incorporated EU. Taking advantage of this, we could measure the median size of the transcription nanodomains. In fibroblasts nanodomains are about 0.13256791 μm^2 and have approximately 14 localizations per cluster **(Figure 44B-C)**.

To our knowledge, our work is the first example of Voronoi analysis applied to segment and quantitatively characterize RNA local density distribution and nano-structure domain characteristics within the nucleus.

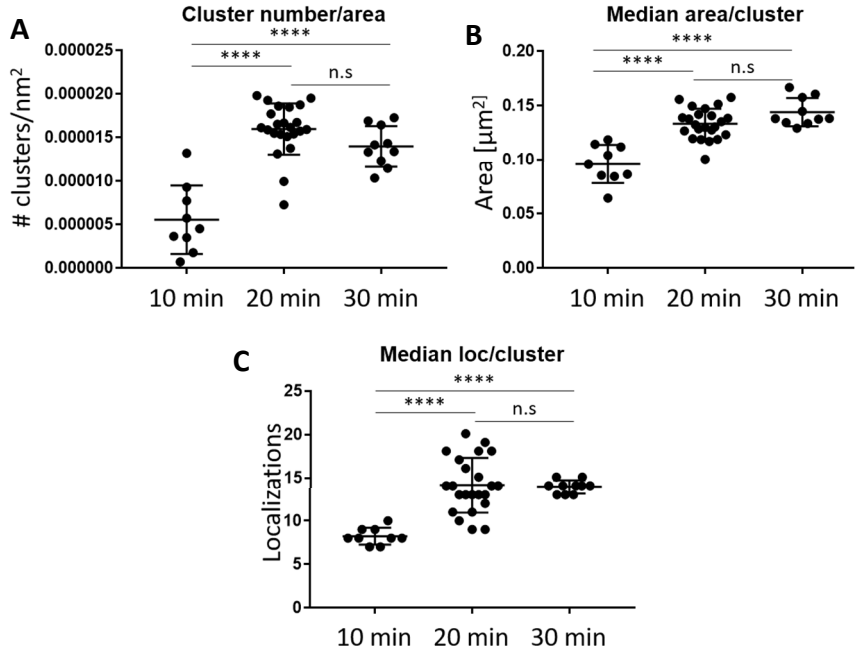

Figure 44. Voronoi clustering allows quantitative measurment of RNA cluster characteristics. **(A)** Number of clusters/μm^2 in the cell nucleus at different time of EU pulse. **(B)** Median size measured in μm^2 of the clusters identified by voronoi clustering **(C)** Median number of localizations per cluster identified by voronoi clustering. Points respresent individual cells. Statistic: Two tailed Unpaired One-way anova with Tukey's multiple comparison test. P-value: n.s=non significant, *<0.05 , **<0.01 ,***<0.001, ****<0.0001.

6.2 Nascent RNA nanodomains are associated with H2B clutches and fall inside the “clutch DNA” radius

In the previous chapter we have discussed the interplay between the nucleosomes, organized in clutches, and the DNA which they compact. To inquire how the nucleosome compaction plays a role in the transcription process, we aimed to carry out two-color super-resolution imaging of RNA and histone H2B, in order to correlate the size and position of the clutches with the amount of RNA produced in that region of the genome.

For this, we applied our previously developed workflow, combining STORM and PAINT in order to obtain two-color super-resolution images.

When we combined the RNA and H2B images **(Figure 45)**, we found that RNA nanodomains tend not to overlap with H2B clutches, but they appear nearby, in association or enveloping them.

To further quantify the spatial relationship between histones and RNA, we segmented the nucleosome clutches using our distance based clustering algorithm (Ricci et al., 2015), determining their centre position. We applied Voronoi analysis using the centre of the clusters as seed for the tessellation.

Dividing the nuclear space into polygons, we were able to assign the RNA localizations as belonging to one specific clutch, and, in that way, study the relation between clutches and RNA.

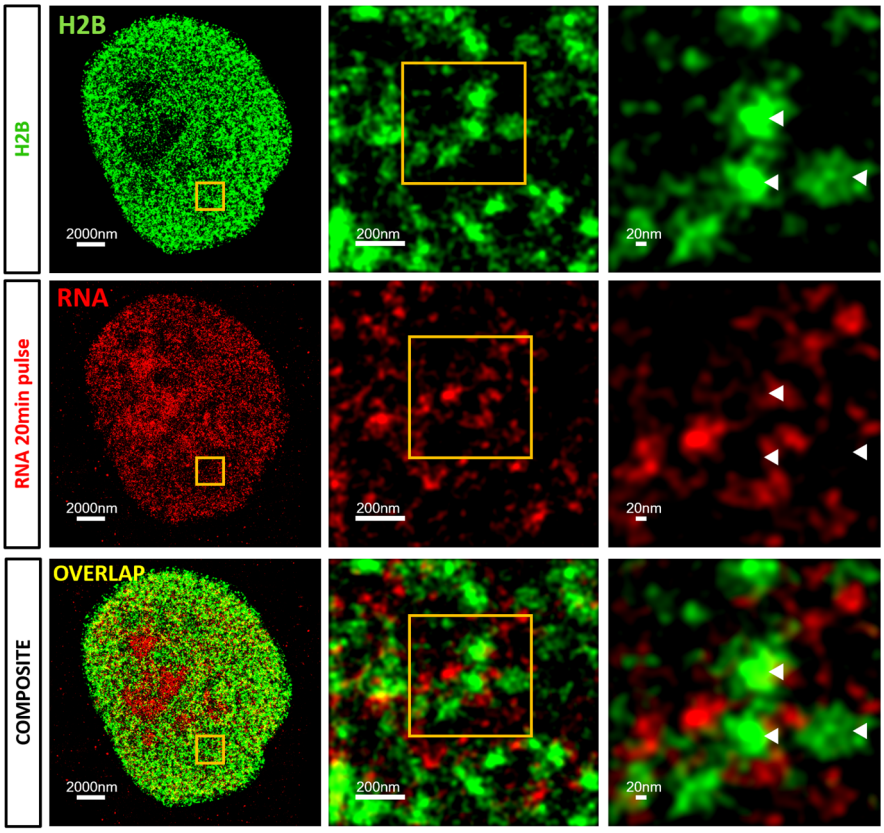

Figure 45. RNA nanodomains interact with H2B clutches. Representative image showing H2B (green), RNA (red) and the overlap between the two. Cells were incubated with 20 min EU prior to fixation. Zoom of the yellow squares are shown. White arrows. H2B clutches.

We found that the highest RNA density is near the clutch centers (Figure 46A), with an area of high variation between the 60 and 120 nm. In every cell (N=6) there are up to tens of thousands of clusters which are binned in this graphic, so the variation should be understood as biological variation. Further away from that distance, the localizations drop drastically. With this, we concluded that the RNA transcription is physically tied to the clutches.

When we look at the cumulative density of DNA **(Figure 46B)** it shows a big increase up until 60 nm away from the clutch

centre, at which moment it becomes fairly homogeneous. This results point towards the nanodomains of RNA being at a distance to the clutch cetre simmilar to that of the “clutch DNA”.

Altough this analysis offers us information about the physical relationship between the clutches and the RNA, it does not take into account the inherent clutch variability. Median clutch size has been correlated with cell state (Ricci et al., 2015), but each cell type has a population of clutches of varying size.

As the size of the clutch could be tied to the transcriptional activity of the cell, we considered it interesting to see the relation between the clutch size and the RNA density around the clutch. For that, we looked at the relation between cumulative amount of localizations and clutch size (measured as clutch area) at fixed radius of density. As we were expecting, we found that the RNA density steadily decreases as the clutches get bigger, showing a relation between chromatin nanostructure and transcriptional capability **(Figure 47)**.

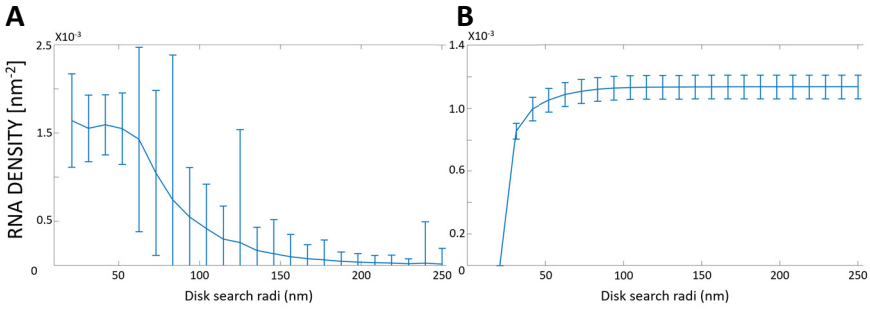

Figure 46. Quantification of association between RNA and H2B **(A)** RNA density as a function of the distance to the clutch center inside rings of increasing search radii. **(B)** Cumulative RNA density inside circles of increasing search radii. The dots correspond to the mean, the bars correspond to the standard deviations: the lines connect sequential points and are guides to the eye.

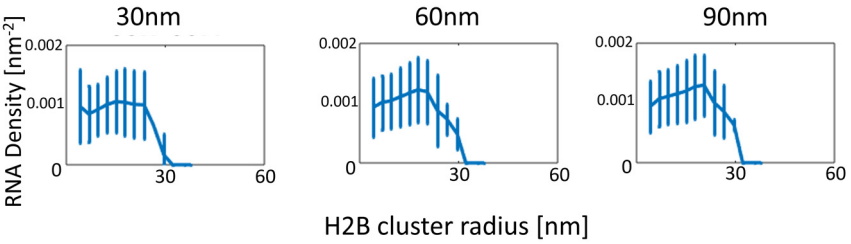

Figure 47. RNA transcription is inversely associated with clutch size. RNA density in a bound circle of increasing size (30-60-90 nm) versus clutch size measured as the cluster radius in nm^2. At bigger clutches, there is less RNA density, showing a lessened transcriptional activity. The dots corresponds to the mean of clusters in that bin; the bars correspond to the standard deviations; the lines connect sequential points and are guides to the eye.

6.3 RNA distribution changes upon chromatin acetylation

Once we established a link between clutches and RNA nanodomains, we explored the role of chromatin structure in RNA nanodomain density and distribution. Our aim was to explore if alterations on the chromatin state would be reflected on the nanodomain structure.

For that, we treated the cells with the HDAC inhibitor Trychostatin-A (TSA) in order to produce a hyperacetylation of histone tails, akin to the experiments performed in Chapter 5. As we have reported, TSA-derived acetylation changes the organization of chromatin. The potential easier accessibility of the transcription machine to the promoters may increase the amount of total RNA, or the characteristics of the RNA nanodomains.

In order to analyze this, we decided to exclude the nucleolus area from our analysis. The nucleolus has a high concentration of RNA, and the amount of localizations that we obtain from it

vary wildly from cell to cell and it is dependent on the relative position of the nucleolus inside the nucleus with respect to the focal plane. As the changes we expected that the changes in distribution were subtler, we excluded these areas in order to avoid any bias that they may introduce to the analysis.

We treated human fibroblasts with increasing concentrations of TSA (75,150 and 300 nM), and incubated them for the last 20 min and 30 min with EU **(Figure 48).** 20 and 30 min were chosen as two representative points of the RNA distribution process, before saturation and with saturated nanodomains.

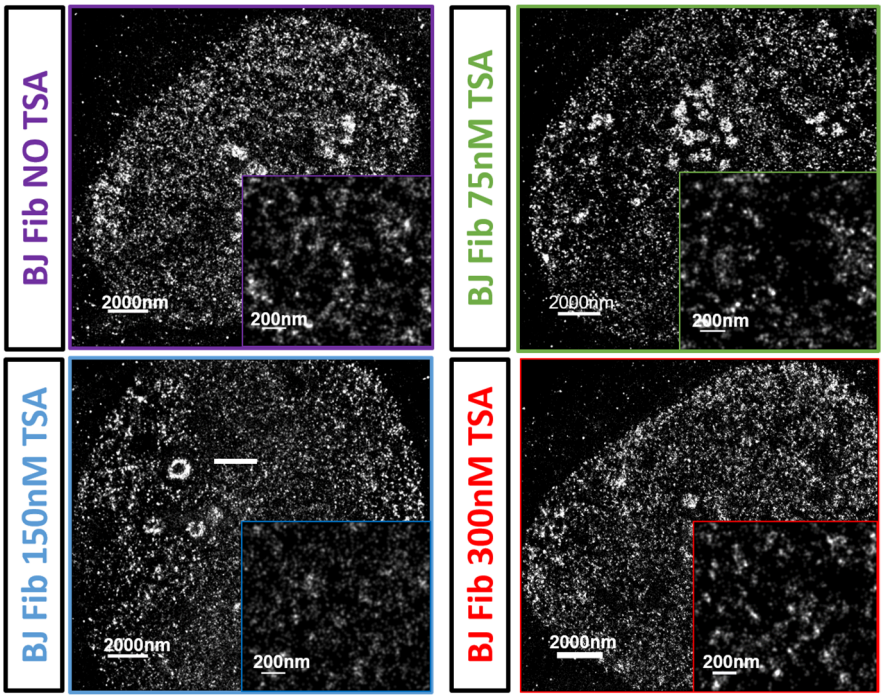

Figure 48. Imaging RNA after chromatin alteration. Representative images of human fibroblasts incubated with 24h with TSA and 20 min with EU prior to fixation. Zooms from each cell are shown.

Surprisingly, at 20 min of EU pulse the overall morphology of the nanodomains remains unchanged after the treatment with TSA **(Figure 49)**. When we analyzed the cells with 30 min EU pulse, we were also unable to find any significant change between all the different TSA concentration conditions.

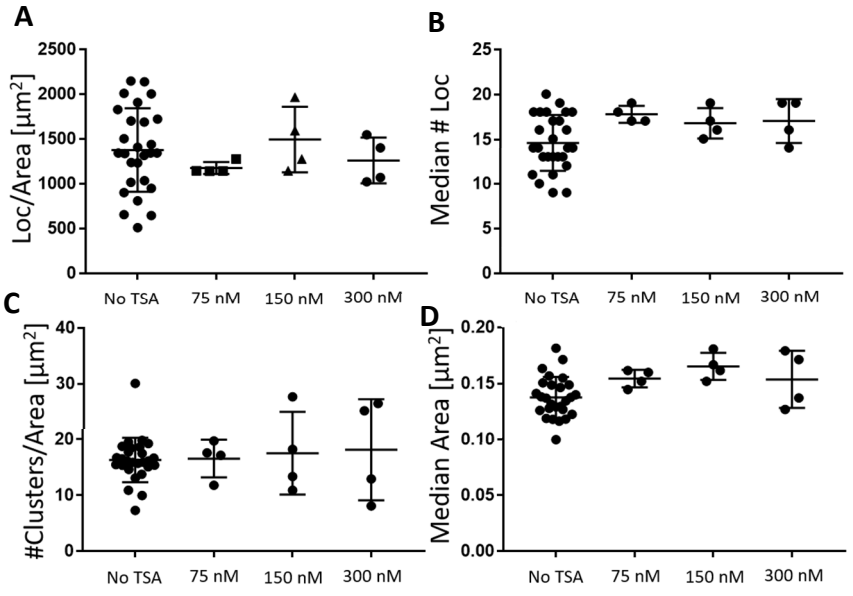

Figure 49. TSA does not affect the localization density and the nanodomain characteristics of RNA. (A) Quantification of density of localizations of RNA inside the nucleus after a 20 min EU pulse, measured as total amount of localizations divided by total area of the nucleus, in micrometres. **(B)** Quantification of the median number of localization per cluster identified using voronoi tessellation after a 20 min EU pulse. **(C)** Quantification of the median area of clusters of RNA identified by Voronoi tesselation after a 20 min EU pulse. **(D)** RNA cluster density inside the 20 min EU pulsed cells measured as number of clusters identified by Voronoi tessellation divided by the total area of the nucleus. Points respresent individual cells. Statistics: two tailed, unpaired one-way ANOVA with Tukey's multiple comparison test. All the comparisons are n.s.

Interestingly, although both the amount of localizations and the characteristics of the nanodomains remain unchanged, quantitative study of the global RNA distribution by means of voronoi tessel distribution show that the tessels are bigger and, accordingly, less dense when we treated the cells with TSA **(Figure 50)**. This effect is mildly seen with the 20 min pulse treatment **(Figure 50A)**, in which the non-tsa treated cells seem to have a higher proportion of more densely distributed localizations when compared with the other conditions.

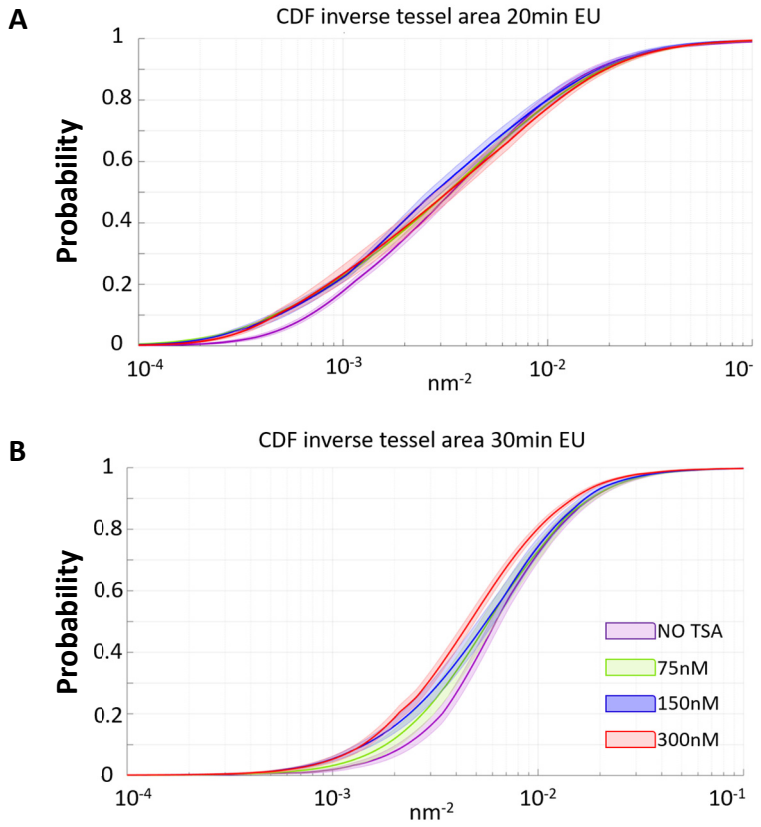

Figure 50. TSA affects the global density distribution of RNA signal. (A) Cumulative Density Fraction plot showing the density of the RNA signal in fibroblasts treated with TSA after 20 min EU pulse. **(B)** Cumulative Density Fraction plot showing the density of the RNA signal in fibroblasts treated with TSA after 30 min EU pulse . Density is measured as the inverse of the tessel area. Scale is logaritmic

The effect becomes more pronounced with the 30 min pulse **(Figure 50B),** with the 300 nM TSA treated cells being even less dense than the 75 and 150 nM TSA treated cells.

The effect of TSA on the rates of transcription is still controversial. There has been reports of TSA both inhibiting or activating gene expression (Görisch et al., 2005; Inoue et al., 2015; Lopez-Atalaya et al., 2013; Moore et al., 2004; Toth et al., 2004). Several studies of global effect of TSA in gene expression exist, showing that there is an increased and decreased expression of several genes (Lopez-Atalaya et al., 2013; Moore et al., 2004).

The difference seen in the tessel distribution is not due to difference in the global amount of localizations, whose change is statistically not siginificant **(Figure 49A)**. As such, we attribute the difference in the CDF distribution to the signal being more concentrated in different regions of the nucleus. If the hyperacetylation produces histone tail acetylation and relaxation of the chromatin, the RNA signal will be more evenly and homogeneously distributed in the nucleus, giving rise to the observed distribution.

6.4. RNA nanodomains are associated with the active form of Pol II

In order to categorize the RNA nanodomains, and see what it is their interplay with the active forms of the Pol II, we performed dual color super-resolution microscopy using the method we developed.

For that, we did pulses of 20 min of EU in human fibroblasts, and labelled them together with Pol II **(Figure 51).** We targeted

RNA Pol ser II, as it is the predominant phosphorilated form during elongation.

We did observe that Pol II ser2 appeared in a clustered conformation **(Figure 51, middle row),** distributing itself along the whole nucleus except for the nucleolus. Aside from the nucleolus, big areas with higher cluster density or cluster exclusion were not observed.

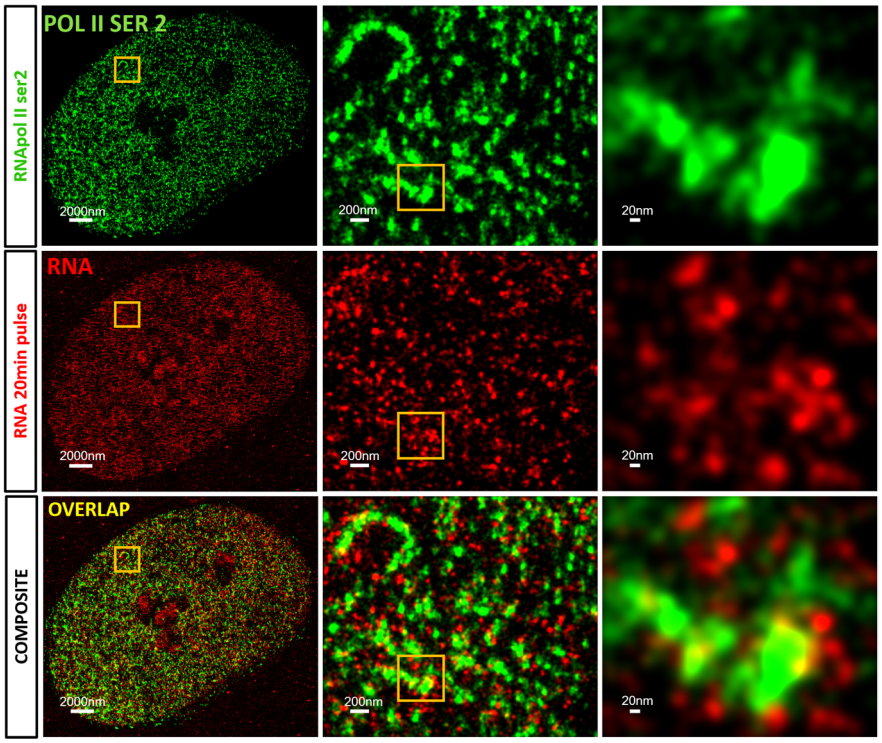

Figure 51. RNA nanodomains are associated with RNA pol II clusters. Representative image showing RNA Pol II ser 2 (green), RNA (red) and the overlap between the two. Cells were incubated for 20 min with EU prior to fixation. Zoom of the yellow squares are shown.

In the image renderings, RNA and Pol II appear mainly colocalizing, or with close spatial association. Nearly all the RNA nanodomains appear close to the clusters, further correlating this areas of high RNA density with active transcription sites.

As the Pol II appears as clusters, we were able to use the same spatial radial analysis which we have previously used for H2B **(Figure 52).** In it, we see a clear association between Pol II clusters and RNA signal, with a peak of density between 0 and 70 nm, at which point the RNA density progressively goes down in a steady way. When we look at the cumulative RNA density, we see that there is a huge increase in the first nanometers away from the Pol II cluster center and then it remains fairly uniform.

Next, we measured the relationship between RNA cluster size and RNA density **(Figure 53)**. It appears to be fairly lineal, indicating a proportionality between the amount of Pol II and the amount of RNA being produced.

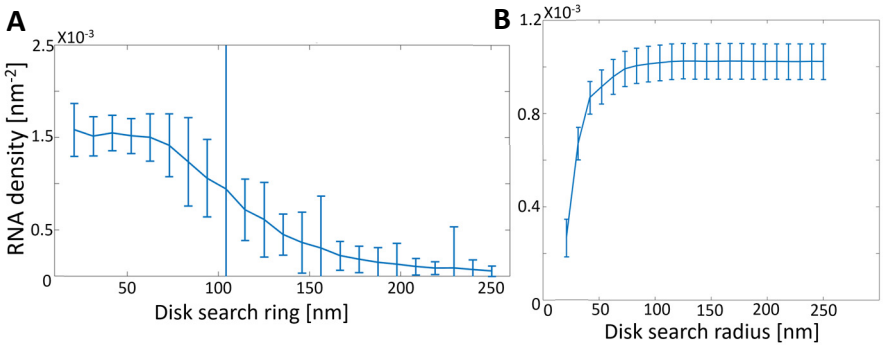

Fig 52. Quantification of association between RNA and Pol II ser2. (A) RNA density as a function of the distance to the Pol II cluster center inside rings of increasing search radii. **(B)** Cumulative RNA density inside circles of increasing search radii. The dots correspond to the mean, the bars correspond to the standard deviations: the lines connect sequential points and are guides to the eye.

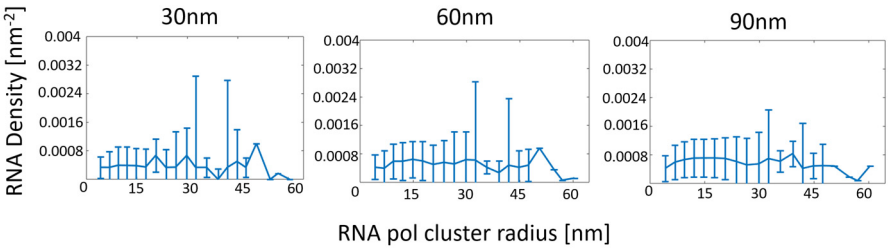

Fig 53. Relation versus Pol II clusters and RNA density. RNA density in a bound circle of increasing size (30-60-90 nm) versus clutch size measured as cluster radius. The RNA density remains uniform as the cluster size increases, indicating a proportionality between the number of Pol II present and the amount of RNA being produced.

6.5. Labelling single gene locus in different states of gene transcription

Once we have seen the distribution of RNA nanodomains and how it changes based on the different chromatin clutch sizes, we asked ourselves if, using super-resolution microscopy, we would be able to detect changes on the transcriptional state of a gene.

For that, we used a cell line in which we can specifically induce the expression of an endogenous gene. GP220 is a gastric cancer cell line whose *MUC4* expression has been reported to increase upon Interleukine 6 (IL-6) treatment (Mejias-Luque et al., 2008).

The pro-inflammatory cytokine Interleukine 6 (IL-6), trough activation of the gp130/STAT3 pathway, has been reported to increase the RNA levels of GP200 by qPCR, which also tranlated to an increased protein level (Mejias-Luque et al., 2008).

Using this gastric cancer cell line as a tool, we wanted to examine changes on active Pol II and RNA distribution density at the *MUC4* locus in order to correlate them to changes in transcription density. We also wanted to see if the locus of *MUC4* would change the relative position inside the nucleus. Finally, we aimed to see if we could detect differences in gene expression between different *MUC4* alleles.

In order to label the *MUC4* locus, we used STAC (SunTAg modified CRISPR), a protein-tagging system for signal amplification based on a SunTag scaffold fused to a CRISPR protein (Neguembor et al., 2018; Tanenbaum et al., 2014). The cognate scFV antibody fused to a GFP, which is expressed in a separate plasmid, recognizes this scaffold. This signal amplification allows us to endogenously tag the *MUC4* locus in genes transfected with the STAC system.

As such, we transfected the cells with the STAC system 48h before imaging. 20 hours before fixation, we added 20ng/ml IL-6 to the cell media. For the last 10 or 20 min, we fed the cells EU in order to label the RNA **(Figure 54)**.

Altough the *MUC4* locus can be seen **(Figure 54, left)**, we are only obtaining a conventional image, making it difficult to correlate it with a particular RNA nanodomain. We solved this problem by taking one image of *MUC4* every 100 frames during the super-resolution imaging acquisition, and treating the *MUC4* locus point as a PSF. With this, we had a cloud of points from which we could extract the center of mass of *MUC4* with nanometric precision.

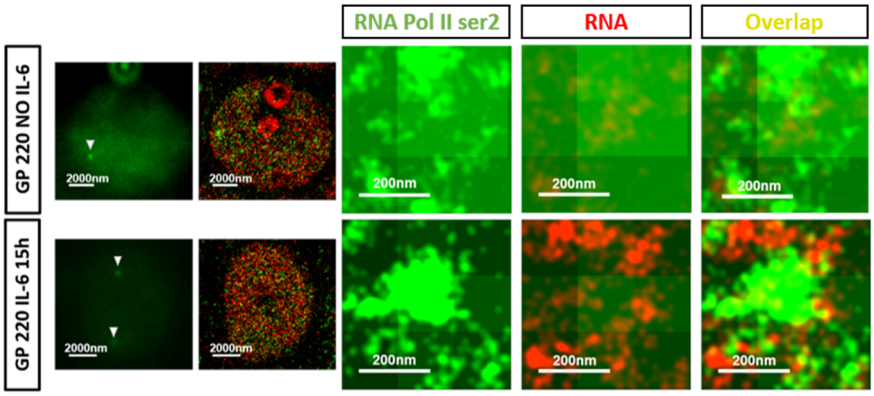

Figure 54. Activation of RNA transcription can be visualized using SMLM. (Left) SunTAg modified CRISPR was used to tag the *MUC4* gene locus with GFP in GP22O cells. The locus are seen as bright nuclear spots (white arrows). (Middle) Super resolution imaging of RNA and Pol II ser2 in *MUC4*-GFP positive cells. (Right) Zoom of Pol II ser2 and RNA signal around the *MUC4* locus.

In order to further quantify the interplay between RNA nanodomains and transcription, we took advantage of our developed SMLM technique in order to obtain images of both RNA and Pol II ser2. Consequently, the cells were labelled against *MUC4* locus, Pol II ser2 and RNA **(Figure 54).**

Our results visually show a clear association between the *MUC4* locus and RNA signals in IL-6 treated cells, and an exclusion of these signals in the untreated condition **(Figure 54)**. The effect of association between the *MUC4* locus and Pol II ser2 signals in IL-6 treated cells is even clearer.

MUC4 locus in the untreated condition were preferentially seen near the nuclear membrane of the perinucleolar heterochromatinized areas, moving towards more nuclear-centric position after IL-6 treatment. It should be noted that our results are an average of all the locus found in the cells. There is an inherent variability, and in occasions, when two locus

could be imaged at the same time (as they were in the same z-plane) a major difference on the pressence and size of overlapping RNA nanodomains could be seen between them.

In order to quantify our results, we measured the cumulative density of RNA as a function of the distance to the *MUC4* locus, showing that there is a clear increase in RNA density in the IL-6 treated cells when compared with the non treated cells. This difference is reduced progressively as we go further away from the *MUC4* locus, moving away from the transcriptionally active site **(Figure 55)**

These results further corroborate the perception of the RNA domains described in this work as active transcription domains, highly variable in size and density but physically tied to active transcription areas of the genome

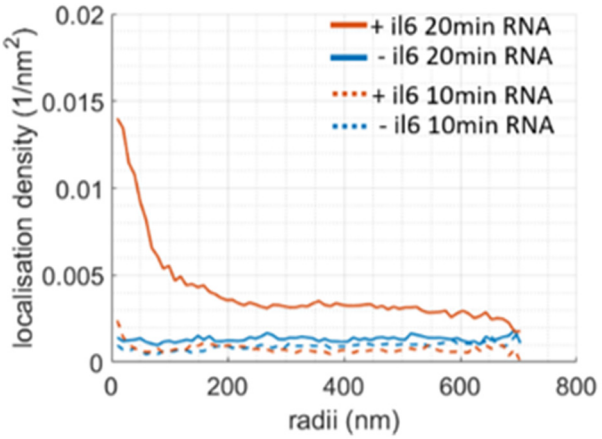

Figure 55. Quantification of RNA density in a transcription active area of the genome. Measurement of the RNA density as a function of the distance to the *MUC4* locus, for both cells treated with a 10 min pulse of EU (dashed line) and a 20 min pulse of EU (straight line).

PART III: Discussion and conclusions

7. DISCUSSION AND CONCLUSIONS OF "COMBINED PAINT AND STORM SUPER-RESOLUTION MICROSCOPY ALLOWS VISUALIZATION OF TWO COLOR 3D DATA OF THE NUCLEUS AT THE NANOSCALE LEVEL"

7.1-Discussion

Nowadays, the toolbox of the biologist has expanded with the advent of single molecule localization microscopy. SMLM allows for the visualization of structures inside the nucleus with a level of detail previously believed not possible to be achieved using light microscopy.

Although relatively new (STORM and PALM were discovered in 2006. PAINT, in 2014) these techniques have already proved their utility in a wide variety of biology topics, such as cytoskeleton dynamics (Balint et al., 2013; Huang et al., 2008; Zhang et al., 2017), neurology (Ladépêche et al., 2018; Xu et al., 2013; Zhang et al., 2016), cardiology (Agullo-Pascual et al., 2014; Soeller and Baddeley, 2013) and, more important for this work, nuclear architecture (Beliveau et al., 2015; Boettiger et al., 2016; Ricci et al., 2015; Xu et al., 2018).

But although these powerful technologies have significant advantages from their conventional counterparts, they also have significant caveats. One of them is the added difficulty of labelling several cellular components at the same time in SMLM. Several approaches have been used to solve this conundrum. The most widely used is the combination of two pairs of antibodies with the same reporter with different activators (Bates et al., 2007), because this allows for the use of A647, the best present dye for super-resolution imaging, as the exclusive reporter.

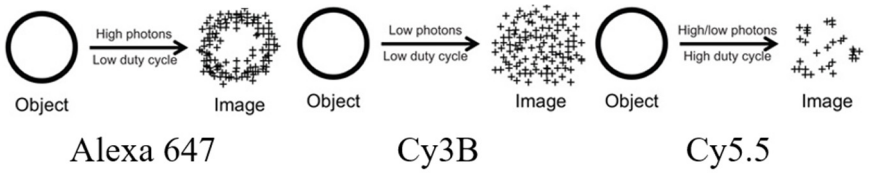

Figure 56. Cy3B does not reliably report the underlying structure. Effect of the amount of photons per localization and the duty cycle (fraction of time in the ON state) on STORM quality. (Left) Alexa 647 has a high photon number and low duty cycle, so is able to reliably report the structure being imaged. (Middle) a fluorophore with low photon number and low duty cycle, such as Cy3B, will obtain a comparable number of localizations to Alexa647, but it will suffer reduced localization accuracy, obscuring the structure imaged. (Right) a fluorophore with a high duty cycle (here Cy5.5 used as an example) drastically reduces the number of localizations obtained when imaging the desired structure, resulting in difficulty imaging the desired structure. Adapted from (Dempsey et al., 2011)

Combinations of spectrally separated photoswtichable dyes have been used since STORM was invented, but they have either been used to solve regular structures (Xu et al., 2013) or together with general quantitative analysis in which a deep localization density and precision was not required (Xu et al., 2018).

In this work, we have demonstrated the inability of a battery of commercially available dyes of labelling chromatin with a density, precision and signal to noise ratio good enough to reliable report nanometric changes in its features.

Of all this set of dyes, Cy3B in particular has been used in several SMLM-based studies (Jaworek et al., 2013; Sunwoo et al., 2015; Xu et al., 2018). In our hands, although it offered the best results, and even some qualitatively similar-looking images, it was incapable of reliably reporting changes on the clutch distribution upon TSA-dependent hyperacetylation.

If we look at the photophysical characteristics of Cy3B **(Table 4)**, we can observe that it has a low duty cycle, but also a low number of photons per duty cycle when compared with A647. A fluorophore with low duty cycles will give a large number of localizations **(Figure 23A)**, but the low photon number will create a reduced localization accuracy **(Figure 23BC, Figure 56)**. This loss of localization density is crucial when recovering non-regular structures in a dense environment. The use of Cy3B as a SMLM fluorophore in chromatin image is thus discouraged.

In this work, a combined super-resolution method for simultaneous imaging of DNA and chromatin in 3D has been developed. This method has been thoroughly tested and has been shown to have a localization precision of 31±15 nm in XY.

The existence of a streamlined workflow opens the door to easily and reliably co-label DNA with several fundamental elements of chromatin organization. Future work in which DNA is labelled together with proteins such as Pol II, Cohesin or Lamin will surely offer interesting results to increase our knowledge of nuclear architecture.

7.2-Conclusions

>Cy3B does not reliably report changes on chromatin structure.

>A DNA-PAINT/STORM combination method which allows for simultaneous, dual-color 3D super-resolution imaging has been developed.

> Combined PAINT and STORM super-resolution microscopy allows visualization of individual histone clusters (clutches) and quantify associated DNA at the nanoscale level.

>The overlapping precision of this method is of 31±15 nm.

8. DISCUSSION AND CONCLUSION OF "SUPER-RESOLUTION MICROSCOPY REVEALS HOW HISTONE TAIL ACETYLATION AFFECTS DNA COMPACTION WITHIN NUCLEOSOMES IN VIVO"

8.1 Discussion

Visualization of DNA fibres at nanoscale resolution within an intact nucleus can potentially reveal details about how chromatin organization relates to gene activation, information that biochemical or genetic approaches can only indirectly infer (Rowley and Corces, 2018). Super-resolution microscopy has recently revealed the spatial organization of chromatin and transcriptional machinery in mammalian and bacterial cells at length scales of individual genes that were previously inaccessible to light microscopy (Beliveau et al., 2015; Boettiger et al., 2016; Cho et al., 2018; Cisse et al., 2013; Ricci et al., 2015; Wang et al., 2016; Weng and Xiao, 2014). Labeling of specific genomic regions using Oligopaint technology and imaging with super-resolution (OligoSTORM) uncovered the higher order packing of genomic regions having different epigenetic states (Beliveau et al., 2015; Bintu et al., 2018; Boettiger et al., 2016; Nir et al., 2018; Wang et al., 2016).

By using super-resolution microscopy, we previously revealed the organization of the chromatin fibers by visualizing nucleosome clutches (Ricci et al., 2015). More recently, pulse-chase EdU labeling and click chemistry followed by super-resolution microscopy was used to label the DNA of individual chromosomes (Fang et al., 2018). These images showed that DNA formed nanodomains, which were further clustered in close spatial proximity, an organization similar to nucleosome clutches that also cluster in close proximity forming "islands".

In addition, multi-color imaging of DNA and histone modifications revealed that active histone marks formed small, disperse nanodomains whereas silencing marks formed large clusters that pack DNA more tightly (Xu et al., 2018). These semi-quantitative and correlative observations suggested that the size of the nucleosome domains may be a determinant of the packing density of DNA and hence the activation/silencing of genes. However, thus far, there had been no quantitative structural analysis probing how DNA packs around multiple nucleosomes within a nanodomain (i.e. clutch), and directly measuring the independent contributions of the nanodomain size and epigenetic state of nucleosomes within a nanodomain to DNA packing.

Here, we carried out multi-color super-resolution imaging of histones together with DNA and highly quantitative spatial analysis to describe i) how the DNA is compacted by the nucleosome clutches and ii) how this compaction changes after histone acetylation.

Our results showed that the percentage of DNA co-localizing with nucleosomes decreased after TSA treatment. Previously, it was modelled chromatin organization using a simple polymer model in which nucleosome occupancy was varied (Ricci et al., 2015). This model predicted that the experimentally observed decrease in nucleosome clutch size after TSA treatment could be recapitulated through a nucleosome removal mechanism leading to lower nucleosome occupancy. Consistent with this synthetic model, our two-color imaging data showed a decrease in the percentage of DNA co-localizing with nucleosome clutches **(Figure 34C)**.

Disruption of both histone-DNA and inter-nucleosome interactions (Eberharter and Becker, 2002; Verdone et al., 2005) may lead to destabilization, sliding and eviction of

nucleosomes, resulting in a lower DNA occupancy. Alternatively, disruption of inter-nucleosome interactions (Collepardo-Guevara et al., 2015) may lead to splitting apart of large nucleosome clutches, leading to opening up and release of previously undetectable nucleosome-free linker DNA.

Further, in the super-resolution image data, we discriminate DNA associated to nucleosome clutches and term it “clutch” DNA. Our results demonstrate that the density and length-scale of clutch DNA, and hence its level of compaction, is dependent on histone tail acetylation but not on the size of the clutch. Hence, our results are in line with recent multi-color super-resolution imaging of DNA and histone modifications, which showed a correlation between abundance of H3K9ac histone with regions having more sparse DNA localizations (Xu et al., 2018). However, our results go further to show that the decreased DNA density in these regions is not due to the smaller size of the domains containing H3K9ac histones but rather to the epigenetic state of these domains.

We found DNA decompaction due to acetylation to be most prominent in highly folded regions of the chromatin, where clutches influence the DNA compaction of other neighbouring clutches in close vicinity **(Figure 57)**. It is likely that many histone tails of groups of clutches within large domains undergo hyperacetylation and hence the DNA compaction is perturbed to the highest level in these regions. This would be caused by the presence of a high-density of interacting nucleosome tails within a clutch, whose hyperacetylation and consequential large amount of repulsive charges would disrupt DNA-histone interactions more strongly. This would in turn lead to a higher DNA decompaction in these regions.

Ultimately, this acetylation-dependent DNA decompaction regulates accessibility of Pol II and transcription factors to DNA

regulatory sequences that may lie in these highly folded and compacted regions of the chromatin. Indeed, in fibroblasts it was previously shown that Pol II is associated to the small and less dense clutches, similar to the ones generated after TSA treatment (Ricci et al., 2015). A gene likely contains multiple clutches and it would be interesting in the future to investigate if Pol II associates mostly with the decompacted DNA generated between the neighbouring nucleosome clutches and within islands encapsulating coding genes. Such visualization could ultimately be informative to study transcriptional activation.

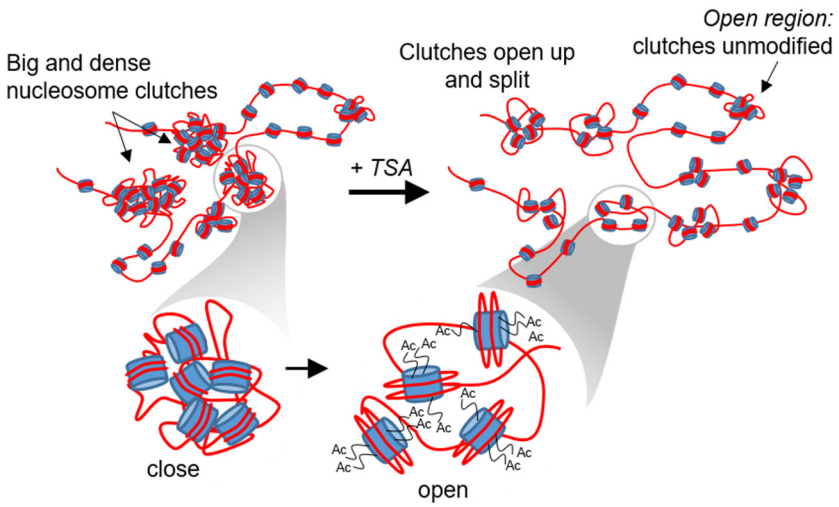

Figure 57. Acetylation changes clutch size and the packing density of clutch DNA. Cartoon model of nucleosomal DNA decompaction upon hyperacetylation. Nucleosome clutches become smaller (see **Figure 24, Figure 28** and **Figure 32**), likely due to a combination of large clutches opening and splitting and nucleosome loss. Clutches also compact "clutch" DNA to a lesser extend in hyperacetylated cells (see **Figure 34D** and **Figure 36**). These changes are particularly prominent in highly folded regions of the chromatin containing multiple nucleosome clutches in close proximity **(**see **Figure 38),** suggesting that clutches may influence DNA compaction of neighboring clutches.

We and others (Chen et al., 2018; Chen et al., 2013; Fang et al., 2018; Kraus et al., 2017; Neguembor et al., 2018) have developed methods to image specific genomic sites. In combination with the highly quantitative analysis methods we developed here, including Voronoi based density and similarity matrix analysis of DNA compaction, these new tools pave the way to study DNA packing at clutches located in specific regulatory regions with nanometric resolution, in order to correlate function with the structure of DNA.

8.2 Conclusions

> Histone hyperacetylation leads to DNA decompaction through decreased nucleosomal occupancy and looser packing of DNA in nucleosome clutches.

> DNA packing density within nucleosome clutches is independent of clutch size, rather it depends on the clutch acetylation level.

> Clutches have a radius of influence in which they affect the packing of the DNA. In human primary fibroblasts, it is of 70 nm from the centre of the clutch.

9. DISCUSSION AND CONCLUSIONS OF SUPER RESOLUTION MICROSCOPY REVEALS THE INTERPLAY BETWEEN CHROMATIN AND NASCENT NUCLEAR RNA

9.1 Discussion

Visualization of RNA transcriptome at nanoscale resolution in an intact nucleus can potentially reveal how transcription is physically organized with a previously unachieved resolution. Currently, the widely accepted model of transcription involves specialized compartments in the nucleus, called transcription factories, which contain proteins directly and indirectly involved in transcription.

The first major evidences for these factories came with the labelling of transcribing RNA with Biotin-UTP in HeLa cells permeabilized with a “physiological buffer” (Iborra et al., 1996). From there, many studies have characterized these compartments.

Two main approaches are used to image the active transcription regions: labelling of transcribing RNA or labelling of active Pol II. As we mentioned in the introduction, different methods of labelling and methodologies of imaging give rise to highly variable number of transcriptionally active areas in the nucleus, ranging from 100 factories (Osborne et al., 2004) to more than 8000 (Pombo et al., 1999). It is generally agreed that these active transcription areas have a sub-diffraction limit size. As such, the use of conventional microscopy for its imaging may give rise to “transcription factories” which are actually aggregates of several active transcription areas that are closer than 200 nm between them. Alternatively, electronic microscopy together with colloidal gold immunolabeling has

been used, but in this case the several fixation procedures may disrupt the underlying structure.

As such, the newly appeared SMLM techniques are ideally suited to study the localization of RNA and RNA polymerase molecules in the nucleus, properly resolving its structure and size. One such study (Zhao et al., 2014) imaged two differentially labelled populations of Pol II using STORM microscopy coupled with light sheet microscopy, showing no overlap between them. From these results, this study challenged the existence of transcription factories. Regrettably, the active Pol II fraction was not specifically targetted, and the estimate of the number of polymerase molecules per cluster seemed much lower than in previous studies.

Other works where transcription was tackled using Super Resolution microscopy were the ones done by the Ibrahim Cissé group (Cho et al., 2016; Cho et al., 2018). They used the Crisp/cas9 system in order to image endogenous Pol II-Dendra2, performing PALM microscopy to obtain super-resolved images. From it they measured the kinetics of Pol II clusters, defining them as very transient aggregations of protein. They measured the interaction kinetics between Pol II-Denra2 clusters and the locus of tagged β-actin after serum stimulation in order to see the interplay between the locus and the transient clusters.

Surprisingly, the super-resolved images showed really sparse localizations forming a small amount of clusters when compared with the images of Pol II- ser2 obtained with PAINT in this work **(Figure 51)**. This results stems probably from differences between PALM and PAINT, as well as the inherent technical difficulties of performing SMLM imaging in live cell nucleus. As such, they could be measuring only a small sub-

set of the total population of Pol II, obtaining in that way smaller, shorter-lived clusters.

We aimed to build upon these studies, labelling not only β-actin but all the nascent RNA, and looking at the characteristics of active transcription areas and its changes upon different labelling times. We also applied our developed method for dual-colour SMLM imaging in order to obtain precisely overlapped images which allowed us to study the interplay between active Pol II and RNA.

We have shown that the RNA is associated in small, dense nanodomains of variable shape that can be identified using Voronoi-based density clustering. The distribution of RNA is nor composed of big, clearly defined clusters, neither an homogeneously distributed population. We established the median size of these clusters as 0.13256791 μm^2, although they appeared to have a considerable population variation.

Interestingly, although we saw regions in which there was a clear exclusion of RNA, the perinuclear region seemed not to be one of those. The classical correlation of peripheral gene position and silencing has been tested by tethering genes to the nuclear edge (Kumaran and Spector, 2008; Reddy et al., 2008). We saw correlation between active Pol II and RNA in all the nucleus regardless of position respect to the nuclear membrane, so our results also are able to identify perinuclear transcription.

The diameter of nucleoplasmic active transcription regions has been previously measured indirectly using RNA FISH and probes targeting different regions of transcripts generated in a factory (Larkin et al., 2013; Papantonis et al., 2010). The distribution of distances offers a mean diameter size of 62 nm. Other, more direct approaches such as the visualization of

nascent transcripts labelled with Biotin-CTP indicate clusters of approximately 87 nm of diameter (Eskiw et al., 2008). In concordance with these described values, our Radial Analysis results showed a region of approximately 70 nm around the Pol II cluster nucleus in which the majority of the RNA appeared, after which there was a steady decline of Pol II density. We have also quantified the amount of RNA as a function of cluster size, seeing a linear relationship between the two of them.

The alteration of the chromatin state of the cell did not result in big changes on the cluster density and size. Consistent with this, it has been observed that when mouse ES cells differentiate, the density of transcription sites remains relatively constant (Faro-Trindade and Cook, 2006). Regardless of this, our Voronoi analysis was capable of identifying small changes on RNA population distribution.

Nowadays, it is largely accepted that the RNA polymerase remains immobilized, and it is the DNA which moves along. However, this should not be necessarily linked to transcription factories. Small, transient aggregations of Pol II could quickly form and desegregate according to the transcriptional status of the cell. Further experiments using Single Particle Tracking of active Pol II dynamics could improve our characterization of the active transcriptional areas.

Continuing our characterization of the super-resolved transcriptome, we investigated the relation between transcription and the previously described nucleosome “clutches” (Ricci et al., 2015). We found RNA nanodomains to be physically associated to the periphery of chromatin clutches. The transcription could then either be of the nucleosome-depleted “linker” regions; or come from DNA that falls under the previously defined “clutch DNA” radius of 70nm. As the RNA density is highest at distances to the clutch centre

closer than these 70 nm, and then it steadily falls, it would seem that the “Clutch DNA” is the one which is being transcribed.

The methods developed to image RNA distribution and structure on the nucleus have allowed us to obtain highly quantitative analysis of the interplay between RNA, Pol II and chromatin. These tools pave the way to study how transcription shapes the chromatin architecture with nanometric resolution, in order to correlate function with RNA structure and distribution.

9.2 Conclusions

>Nascent RNA is unevenly distributed in the cell nucleus, forming discrete nanodomains with a median size of 0.13 μm^2

>Nascent RNA is associated with H2B clutches and falls inside the “clutch DNA” radius

>Nascent RNA is associated within 70 nm of clusters of active Pol II. The amount of RNA is proportional to the amount of polymerase on the cluster.

PART IV: Methods and Bibliography

10. MATERIAL AND METHODS

10.1 Cell Culture and Sample Preparation

Human Fibroblasts (hFb) (BJ, Skin Fibroblast, American Type Culture Collection, ATCC CRL-2522) and GP220 cells (RRID:CVCL_S968, kind gift from Bolo's lab) were cultured in DMEM (#41965062, Gibco) supplemented with 10% FBS (#10270106, Gibco), 1X Non-Essential Amino Acids (#11140050, Gibco), 1X Penicilin/Streptomycin (#15140122, Gibco) and 1x GlutaMax (#35050061, Gibco).

For DNA labeling experiments, cells were cultured with 5μM Ethynil-deoxy-Cytdine (EdC) (#T511307, Sigma-Aldrich) for 96h previous to fixation. For RNA labeling experiments, cells were cultured with 1mM Ethynil-Uridine (EU) (#E10345, Thermo Fisher) for 10-20-30-60 min prior to fixation. Due to the short time of the EU pulses, 2mM EU on pre-heated media was added 1:1 to the cells without media change.

For hyperacetylation experiments, hFb were treated with 75-150-300 nM of TrychostatinA (TSA) (#T8552 Sigma-Aldrich) in complete growth medium supplemented with either i) TSA during the final 24h of the 96h 5μM EdC incubation before fixation or ii) 1mM EU during the final 20-30 min of the 24h TSA incubation.

When using fiduciary markers for drift correction and 3D overlap, growth media was supplemented with 1:800 dilution of 160nm amino yellow beads (#AFP-0252-2, Spherotech) for 1 hour prior to fixation to allow internalization of the beads into the cells prior to fixation.

10.2 Cell cycle analysis

hFb were grown in growth media supplemented with EdC for 96h. The cells were collected and were resuspended gently with ethanol 70% at -20C. The cells were pelleted, washed and resuspended in Propidium Iodide (Molecular Probes, #P-1304) 0.03 mg/ml, Sodium Citrate 1.1mM and RNAse A (Sigma, #R-5503) 0.3mg/mL in PBS at 4C overnight. Flow cytometry analysis was performed in a FACSCalibur (BD Biosciences). Cell cycle analysis was performed using the ModFit program.

10.3 Staining for STORM

For imaging experiments, cells were plated on 8-well Lab-tek #1 borosilicate chambers (#155411, Nunc) at a seeding density of 20000-30000 per well for immunostaining and RNA labeling experiments; and at a seeding density of 5000-10000 cells per well for DNA labeling experiment to allow cell proliferation and hence EdC incorporation to the genome.

The cells were fixed with 4% PFA (#43368, Alfa Aesar) diluted in PBS for 15min at room temperature (RT). Then, they were permeabilized with 0.3% v/v Triton X-100 (#327371000, AcrosOrganics) in PBS for 15 min at room temperature. Cells were then blocked using 10% BSA (#9048468 Fisher Scientific) (w/v), 0.01% v/v Triton X-100 in PBS.

Cells were incubated overnight with the rabbit polyclonal anti-H2B (Abcam, #1790) diluted 1:50 in blocking buffer or with mouse mono-clonal anti-RNA Pol ser 2 (Mbl, #MABI0602) primary antibody diluted 1:50 in blocking buffer, at 4C with gentle rocking. Finally, cells were washed three times with blocking buffer, then incubated with 1:50 secondary antibody for STORM Imaging (see below) for 1h at room temperature.

For PAINT labeling, we used the Ultivue Paint Kit (Ultivue-2). Cells were incubated for 2 h at room temperature with 1:100 of Goat-anti-Rabbit (D2) antibody diluted in Antibody Dilution Buffer. Lastly, click chemistry was performed.

For click chemistry, we prepared a reaction consisting of Hepes pH8.2 150mM, Amino Guanidine 50mM (#396494, Sigma), Ascorbic Acid 100 mM (#A92902, Sigma), CuSO4 1mM, Glucose 2% (#G8270, Sigma), Glox (described in STORM imaging) 1:1000 and Alexa647 azide 10nM (#A10277, Thermo). The sample was incubated in this reaction for 30min at RT. Repeated washing was done at every step.

The secondary antibody used was donkey-anti rabbit NHS ester (Jackson ImmunoResearch) custom labeled with AF405/AF647 activator reporter dyes as previously described (Bates et al., 2007).

10.4 Confocal imaging and analysis

Cells were incubated with EdC and stained according to the protocol described in 10.1 and 10.3. Cells were incubated for 5min with DAPI 1µg/mL and washed with PBS before imaging acquisition.

Images were acquired in a Leica TCS SP5 II confocal microscope, with a 63.0 × 1.4 NA HCX PL APO lambda blue oil immersion objective. To quantify the overlapping, “coloc2” plugin from FIJI was used, selecting as a ROI the nucleus of the cells.

10.5 STORM imaging and analysis

Imaging of H2B single color images with spectrally different dyes and DNA sigle color images was performed on a custom-built inverted microscope based on Nikon Eclipse Ti frame (Nikon Instruments). The excitation module was equipped with five excitation laser lines: 405 nm (100 mW, OBIS Coherent, CA), 488 nm (200 mW, Coherent Sapphire, CA), 561 nm (500 mW MPB Communications, Canada), 647 nm (500 mW MPB Communications, Canada) and 750nm (500 mW MPB Communications, Canada).

Each laser beam power was regulated through AOMs (AA Opto Electonics MT80 A1,5 Vis) and different wavelengths were coupled into an oil immersion 1.49 NA objective (Nikon). An inclined illumination mode (Tokunaga et al., 2008) was used to obtain the images. The focus was locked through the Perfect Focus System (Nikon). The fluorescence signal was collected by the same objective and imaged onto an EMCCD camera (Andor iXon X3 DU-897, Andor Technologies). Fluorescence emitted signal was spectrally filtered by either a Quad Band beamsplitter (ZT405/488/561/647rpc-UF2, Chroma Technology) with Quad Band emission filter (ZET405/488/561/647m-TRF, Chroma), or a custom Penta Band beamsplitter (ZT405/488/561/647/752rpc-UF2) with a Penta Band Emission filter (ZET405/488/561/647-656/752m) as in (Boettiger et al., 2016).

STORM and STORM+PAINT raw image data were acquired at 20 ms per frame. 488nm, 560nm, 647nm or 750nm lasers were used for exciting the reporter dye and switching it to the dark state, and a 405nm laser was used for reactivating the reporter dye. An imaging cycle was used in which one frame belonging to the activating pulse laser (405) was alternated with three frames belonging to the reporter dye. Single color

imaging was performed using a previously described imaging buffer (Bates et al, 2007): 100mM Cysteamine MEA (#30070, Sigma-Aldrich), 5% Glucose (#G8270, Sigma-Aldrich, 1% Glox (0.5 mg/ml glucose oxidase, 40 mg/ml catalase (#G2133 and #C100, Sigma-Aldrich)) in PBS. A minimum of 45000 frames were obtained for every image.

For single color RNA images and all dual color images, 3D SMLM images were acquired with a commercial N-STORM microscope (Nikon) equipped with a CFI HP Apochromat TIRF 100 × 1.49 oil objective, an iXon Ultra 897 camera (Andor) and a Dual View system (Photometrics DV2 housing with a T647lpxr dichroic beamsplitter from Chroma). The dual view allowed us to split the image on the full chip of the camera based on emission wavelength. 647nm laser was used to excite the DNA labelled with AlexaFluor 647 using a power density of ~3 kW/cm^2. Simultaneously, in order to perform PAINT, the 560nm laser was used with ~0.8 kW/cm^2 power density to excite the dye attached to the imager strand. The 405 laser was used for reactivating AlexaFluor 647 via dSTORM during acquisition. The 488 laser at ~0.1 kW/cm^2 power density was used to illuminate the fiduciary beads, which were used for drift correction and chromatic alignment.

The imaging cycle was composed by 19/100 frames of simultaneous 405 nm, 560 nm and 647 nm activation interspersed with one frame of 488 nm illumination. The yellow beads imaged with the 488nm laser were visible in both the red and orange channel, albeit dimly in the red channel. In all cases, Alexa 647 was progressively reactivated with increasing 405 nm laser power during acquisition up to a maximal power density of 0.020 kW/cm2. The imaging buffer was composed of 100mM Cysteamine MEA, 5% Glucose, 1% Glox and 0.75 nM Imager strand (I2-560 Ultivue) in Ultivue Imaging Buffer. Localizations were extracted from raw images

of bead calibration, STORM and STORM+PAINT data using Insight 3 standalone software (kind gift of Bo Huang, UCSF).

The N-STORM cylindrical lens adaptor was used for STORM+PAINT data acquisition to obtain 3D localization data, as previously described (Huang et al., 2008). Briefly, calibration data was first acquired by imaging subdiffraction limit size beads (100nm Tetraspeck, ThermoScientific, T7279) in PBS adsorbed to clean glass at low enough dilution to enable single bead visualization.

Using the NIS software STORM module, Z-calibration data was recorded as the microscope stage was moved in 10nm steps over a 1.6 μm range and through the objective focal plane to image the elliptically shaped beads as they first elongated vertically, then horizontally. Bead localizations were extracted using the aforementioned Insight3 software through elliptical Gaussian fitting to extract horizontal and vertical width values (Wx and Wy, respectively). These widths were plotted versus the distance of the localization from the imaging focal plane, then fit with a 3rd order polynomial, as previously established (Huang et al., 2008) . The coefficients of the polynomial function were input into the Insight3 software to enable assignment of an axial, *z*, position to elliptical localizations from STORM+PAINT data in addition to their lateral, *x* and *y*, positions. Rendering of DNA and histone images was performed using a summation of uniform Gaussian peaks having a fixed width of 20nm.

10.6 STORM-PAINT Workflow

STORM localizations of DNA structure in the red 647nm channel were overlaid with PAINT localizations of histone structure in the orange 560nm channel through a defined,

multistep data workflow. Firstly, the same Tetraspeck beads used for Z-calibration were utilized to define a single, 2nd order polynomial surface transfer function to overlay the two colors in *x* and *y* when imaged with the dual view. To this end, beads in 10-15 separate fields of view were imaged for 100 frames. The localizations were grouped into bead-clusters and their center identified. The bead centers from all fields of view were combined to create a pseudo-high density image map to define the registration between the orange and red channel and remove residual chromatic aberrations.

Raw STORM+PAINT image data was obtained using the aforementioned microscope hardware, including the dual view and NSTORM cylindrical lens, to record a minimum of 200,000 frames with 20ms camera exposure. Red-channel STORM localizations were extracted in 3D from the 20ms images. For the orange channel PAINT localizations, five sequential image frames were first summed together to obtain an effective 100ms camera exposure, then the 2D/3D localizations were extracted from these summed frame images. The 5-frame summed images were used also to extract red-channel fiduciary bead localizations, and thereby improve the bead's signal-to-background ratio, while the orange-channel fiduciary bead localizations were extracted from the raw 20ms images.

All orange-channel localizations were first overlaid upon the red channel localizations in *x* and *y* using the 2nd order polynomial surface transfer function. Next, bead localizations in each color were grouped into bead-clusters and used to extract and correct the drift trajectory for each color throughout data acquisition. Following drift correction of the datasets, the fiduciary bead positions were used to refine the lateral alignment of the two datasets in *x* and *y* using a linear affine transformation.

Finally, for 3D regime, the axial positions of the fiduciary beads were used to apply a rigid Z-translation to the orange dataset and fully overlay the 3D DNA and histone datasets. Once aligned, a 120nm slice centered near the imaging focal plane (*i.e.* Z=0) was selected for further co-structural analysis. This workflow was automated using functions developed in MATLAB version 2013a and 2016a.

10.7 Localization quantification

For **(Figure 30 and 41)**, ROIs defining the nucleus were manually drawn. Based on this ROI, the area for each individual nucelus was calculated and the amount of localizations were extracted. Density was calculated dividing the amount of localizations on the nucleus by the nucleus area.

10.8 Voronoi Tesselation Analysis

Voronoi Tesselation Analysis was performed in MATLAB 2016a in a fashion similar to (Andronov et al., 2016). First, the lateral *x,*y localizations were input into the 'delaunayTriangulation' function, and then used to construct Voronoi polygons using the 'Voronoidiagram' function. Areas of the Voronoi polygons were determined from the vertices with the function 'polyarea'. The local density in each data point was defined as the inverse value of the area of the corresponding Voronoi polygon.

Voronoi polygons were visualized using the 'patch' function, wherein the look up table was mapped to cover 99% of the polygons; the smallest polygons being yellow (high density, greater than 0.02 nm^2), larger polygons set to blue, (low

density, lower than 0.001 nm^2), and the largest 0.5% of polygons set to black.

Voronoi clusters were obtained following the method defined by (Andronov et al., 2016). After voronoi tesselation, the experimental data is intersected with the Monte Carlo simulation of the mean Voronoi polygon distribution of a random dataset generated from the area and number of localizations from the experimental data. The point of intersection is the treshold of tessel area below which the localizations are considered clustered. A minimum number of 5 localizations per cluser was used. The area of clusters was obtained by summation of the tessels of the localizations that comprise a cluster.

Voronoi distributions were plotted used a Matlab custom made software. DNA Voronoi density data in **(Figure 42 and 47)** was obtained by binning the Voronoi density distributions for the control cells and TSA-treated cells into 300 logarithmically spaced bins. Density of clusters was obtained dividing the number of clusters by the nucleus area derived from the ROI selection.

10.9 Radial density analysis

Radial density analysis was performed using a custom-written script in Python, version 2.7. The script takes as input the localizations of DNA, as directly obtained by dual-color STORM imaging, and the centroids of the H2B clusters, extracted by a previously developed Matlab script (Ricci et al., 2015).

The coordinates of H2B or RNA Pol clusters' centroids were used as center for Voronoi tessellation. Voronoi polygons

exceeding the nuclear periphery or in within the nucleoli regions were clipped to a hand-drawn mask (*voronoi_finite_polygons_2d.py function*). The DNA or RNA localizations falling within the clipped Voronoi polygon area of a particular clutch center were considered for further analysis.

This procedure assigns every DNA localization to a single H2B cluster, preventing the over counting of DNA localizations during the computation. Starting from the H2B clusters' centroid, circles of increasing radii (steps of 10 nm) were drawn and eventually bounded to the Voronoi polygon (i.e. for circles larger than the polygon, the edges of the polygon were used to clip the circle). The DNA density in within each clipped circle was calculated as the ratio between the number of DNA localizations falling within the clipped circle and the area of the disk (**Figure 33**).

For cluster size versus density analysis, the output of the cluster size was used together with the output of the radial density analysis, in order to match the radial density with the size of each cluster using a custom-written script in Matlab. The output was then binned according to cluster size, measured as cluster radius, and the median of the densities for each bin was plotted.

To quantify the percentage of DNA localizations associated to nucleosome clutches, a clipped circle of 120 nm radius was drawn and the percentage of DNA localizations inside the disk over the total DNA localization in the polygon was calculated. From this analysis we also quantified the percentage of H2B clusters that have more the 5 DNA localizations inside the clipped circle of 120 nm radius (**Figure 33**).

For *MUC4*, the center of mass of localizations belonging to *MUC4*-GFP was treated as the centroid of the cluster, and the

localizations were measured in concentric, unbound rings in 10nm steps, divided by the area of those rings.

10.10 Statistical analysis

Graphpad Prism (v5.04) and Matlab 2016a were used for Statistical analysis.

DNA Voronoi density data in **(Figure 31)** was obtained by binning the Voronoi density distributions for the six control cells and nine TSA-treated cells into 300 logarithmically spaced bins ranging from 0.1x10-9 to 0.94 nm2, which encompassed the maximal range of the 15 datasets. The median value and interquartile range for each bin was calculated and used to create **(Figure 31)**; p-value for two-sample Kolmogorov-Smirnov test between median value distributions is 0.0022.

The similarity matrix of **(Figure 36-37)** is calculated in MATLAB 2016a using the 'kruskalwallis' function to calculate p-value resulting from the Kruskal-Wallis test. This non-parametric version of ANOVA is applicable to the non-Normally distributed data we encounter and calculates the likelihood that rank means from two groups are drawn from the same distribution.

To this end, the density of DNA localizations falling within pairs of search discs around H2B clusters is input into the function and the resulting p-value matrix comparing all off-diagonal search discs is shown in (**Figure 36)**. The diagonal elements were not calculated because the resulting p-value would indicate experimental reproducibility rather than provide information regarding changes in DNA density over a distance. Search discs having highly similar DNA densities give rise to larger p-values and are color-coded in yellow, whereas discs

having low similarity give rise to small p-values and are color-coded in blue.

The nearest neighbor distance (NND) analysis of **(Figure 38)** was performed by first grouping NND distances between H2B clusters within the same island (see **Figure 20D**) into bins of 20nm spacing. For each bin, the mean cumulative DNA density (i.e. sum of DNA localizations within a search radius divided by the bounded search area) within a search radius of 70nm from the H2B clutch centroid was calculated for each dataset, four control nuclei and five TSA treated nuclei. **(Figure 38**) was generated by plotting the average of the means across datasets within each bin ±standard deviation.

Statistical significances in **(Figures 22 and 23C)** were calculated using an unpaired two-sample t-test against A647. Statistical significance in **(Figure 24)** was calculated using a two-sample Kolmogorov-Smirnov test.

Unpaired two way Anova with Bonferroni multiple comparison test against not treated was used for Cell Cycle experiments **(Figure 18)**. Un-paired two-sample t-test was used for **(Figure 30).** Un-paired two-sample t-test with Welchs's correction (due to low number of points) was used for **(Figure 34A,C).**

Unpaired two-tailed One-way Anova with Tukey's multiple comparison test was used for **(Figure 41, 44 and 49).**

For all tests: ns $P > 0.05$, *$P \leq 0.05$, **$P \leq 0.01$, ***$P \leq 0.001$, ****$P \leq 0.0001$.

10.11 Dataset selection & H2B cluster analysis

The inclined illumination utilized on our microscope systems often gave rise to illumination inhomogeneity that was visualized as long, straight areas of a nucleus having sparse localizations. Sub-regions having a more uniform illumination for both 560nm and 647nm laser lines were selected manually and used for H2B and DNA data analysis. A single sub-region was selected for each dataset.

We measured the median lateral localization precision for visualizing H2B *in situ* via DNA-PAINT (Schnitzbauer et al., 2017) methodology to be 20.6 nm (16.4, 25.0 interquartile range). The precision was determined by calculating lateral localization precision as the 2D width of a point cloud for localizations visualized in five or more sequential imaging frames (Olivier et al., 2013). H2B cluster segmentation analysis was performed using the same algorithm previously published (Ricci et al., 2015).

STORM-DNA and PAINT-H2B images were subjected to a quality test as described next and only those images that passed the quality test were accepted for further analysis. DNA datasets were selected according to an estimate for their Nyquist sampling frequency as described previously (Legant et al., 2016). To this end, two localization densities were calculated for each dataset relative to the nuclear area measured by 1) a diffraction-limited image, and 2) binning localizations into boxes 20nm on each side. Dividing the 120nm slice thickness by this density value, and then taking the cube-root provided an estimate for the sampling frequency within a dataset. The mean ± error value across all datasets was found to be 30±2 nm/localization. Datasets utilized in DNA analysis **(Figure 28,31)** were required be 32 nm/localization or lower for both densities (1) and (2).

For H2B, thresholds were applied following cluster analysis of an H2B-PAINT dataset using the resulting cluster metrics to determine the quality of a dataset. The three cluster metrics used to select datasets were: (i) localization occupied nuclear area **(Figure 22A)**, (ii) clusters per island **(Figure 22C)** and (iii) the nuclear area comprising clusters. This latter metric is a ratio of the area covered by clusters compared to the area covered by localizations, where datasets having low ratios were found to be visually sparser than datasets having a higher ratio. Because the TSA treatment led to H2B reorganization, separate thresholds had to be set for control vs. treated cells. For control Cells, PAINT datasets used for analysis of H2B clusters **(Figures 32-37)** were required to have: (i) occupancy > 35%, (ii) clustered area > 15%, (iii) clusters per island > 3; for TSA-treated cells they were required to have: (i) occupancy > 25%, (ii) clustered area > 10%, (iii) clusters per island > 1.5. Dataset selection appeared robust because no datasets were found to have only one or two of the metrics above/below the thresholds. Rather, datasets removed from analysis were found to have all three metrics below the respective thresholds in all cases, while datasets included in the analysis had all three metrics well above the thresholds. Datasets utilized in co-structure analysis were required to pass the selection criteria for both DNA and H2B.

10.12 Muc4 labelling

For transfection, the following plasmids were used:

- pHRdSV40-NLS-dCas9–24xGCN4_v4-NLS-P2A-BFP-dWPRE (Addgene # 60910)
-pHR-scFv-GCN4-sfGFP-GB1-NLS-dWPRE (Addgene # 60906)
-pSLQ1661-sgMUC4-E3(F+E) (Addgene # 51025)

Transfections were performed in suspension with Fugene HD (#E2311, Promega) for GP220 cells under manufacturer's conditions and with equimolar amounts of plasmids. Transfected cells were directly plated on 8-well Lab-Tek I borosilicate chambers (#155411, Nunc) at a density of 3.5 × 10^5 cells/cm^2.

Cells were labelled and imaged following the same protocols for dual color Rna Pol/ RNA imaging. From the bead frames (frames illuminated with 488 laser) , a localization list of the *MUC4* locus was obtained, and the centroid was calculated from the centre of mass of the localization cloud after Drift Correction.

11. REFERENCES.

Agullo-Pascual, E., Lin, X., Leo-Macias, A., Zhang, M., Liang, F.X., Li, Z., Pfenniger, A., Lubkemeier, I., Keegan, S., Fenyo, D., et al. (2014). Super-resolution imaging reveals that loss of the C-terminus of connexin43 limits microtubule plus-end capture and NaV1.5 localization at the intercalated disc. Cardiovascular research 104, 371-381.

Allen, G.D. (1990). Modfit: A pharmacokinetics computer program. Biopharmaceutics & Drug Disposition 11, 477-498.

Andronov, L., Orlov, I., Lutz, Y., Vonesch, J.-L., and Klaholz, B.P. (2016). ClusterViSu, a method for clustering of protein complexes by Voronoi tessellation in super-resolution microscopy. Scientific Reports 6, 24084.

Annibale, P., Scarselli, M., Greco, M., and Radenovic, A. (2012). Identification of the factors affecting co-localization precision for quantitative multicolor localization microscopy. Optical Nanoscopy 1, 9.

Aurenhammer, F. (1991). Voronoi diagrams—a survey of a fundamental geometric data structure. ACM Comput. Surv. 23, 345-405.

Baddeley, D., Jayasinghe, I.D., Cremer, C., Cannell, M.B., and Soeller, C. (2009). Light-induced dark states of organic fluochromes enable 30 nm resolution imaging in standard media. Biophysical journal 96, L22-24.

Balint, S., Verdeny Vilanova, I., Sandoval Alvarez, A., and Lakadamyali, M. (2013). Correlative live-cell and superresolution microscopy reveals cargo transport dynamics at microtubule intersections. Proceedings of the National Academy of Sciences of the United States of America 110, 3375-3380.

Bannister, A.J., and Kouzarides, T. (2011). Regulation of chromatin by histone modifications. Cell Research 21, 381-395.

Banterle, N., Bui, K.H., Lemke, E.A., and Beck, M. (2013). Fourier ring correlation as a resolution criterion for super-resolution microscopy. Journal of Structural Biology 183, 363-367.

Baranello, L., Wojtowicz, D., Cui, K., Devaiah, B.N., Chung, H.-J., Chan-Salis, K.Y., Guha, R., Wilson, K., Zhang, X., Zhang, H., et al. (2016). RNA Polymerase II Regulates Topoisomerase 1 Activity to Favor Efficient Transcription. Cell 165, 357-371.

Bates, M., Blosser, T.R., and Zhuang, X. (2005). Short-range spectroscopic ruler based on a single-molecule optical switch. Phys Rev Lett 94, 108101.

Bates, M., Dempsey, G.T., Chen, K.H., and Zhuang, X. (2012). Multicolor super-resolution fluorescence imaging via multi-parameter fluorophore detection. Chemphyschem : a European journal of chemical physics and physical chemistry 13, 99-107.

Bates, M., Huang, B., Dempsey, G.T., and Zhuang, X. (2007). Multicolor super-resolution imaging with photo-switchable fluorescent probes. Science 317, 1749-1753.

Beliveau, B.J., Apostolopoulos, N., and Wu, C.-t. (2014). Visualizing Genomes with Oligopaint FISH Probes. Current Protocols in Molecular Biology 105, 14.23.11-14.23.20.

Beliveau, B.J., Boettiger, A.N., Avendaño, M.S., Jungmann, R., McCole, R.B., Joyce, E.F., Kim-Kiselak, C., Bantignies, F., Fonseka, C.Y., Erceg, J., et al. (2015). Single-molecule super-resolution imaging of chromosomes and in situ haplotype visualization using Oligopaint FISH probes. Nature Communications 6, 7147.

Beliveau, B.J., Boettiger, A.N., Nir, G., Bintu, B., Yin, P., Zhuang, X., and Wu, C.T. (2017). In Situ Super-Resolution Imaging of Genomic DNA with OligoSTORM and OligoDNA-PAINT. Methods in molecular biology (Clifton, N.J.) 1663, 231-252.

Benke, A., and Manley, S. (2012). Live-cell dSTORM of cellular DNA based on direct DNA labeling. Chembiochem : a European journal of chemical biology 13, 298-301.

Bernecky, C., Herzog, F., Baumeister, W., Plitzko, J.M., and Cramer, P. (2016). Structure of transcribing mammalian RNA polymerase II. Nature 529, 551-554.

Betzig, E., Patterson, G.H., Sougrat, R., Lindwasser, O.W., Olenych, S., Bonifacino, J.S., Davidson, M.W., Lippincott-Schwartz, J., and Hess, H.F. (2006). Imaging intracellular

fluorescent proteins at nanometer resolution. Science 313, 1642-1645.
Betzig, E., Trautman, J.K., Harris, T.D., Weiner, J.S., and Kostelak, R.L. (1991). Breaking the diffraction barrier: optical microscopy on a nanometric scale. Science 251, 1468-1470.
Bintu, B., Mateo, L.J., Su, J.-H., Sinnott-Armstrong, N.A., Parker, M., Kinrot, S., Yamaya, K., Boettiger, A.N., and Zhuang, X. (2018). Super-resolution chromatin tracing reveals domains and cooperative interactions in single cells. Science 362, eaau1783.
Blumhardt, P., Stein, J., Mücksch, J., Stehr, F., Bauer, J., Jungmann, R., and Schwille, P. (2018). Photo-Induced Depletion of Binding Sites in DNA-PAINT Microscopy. Molecules (Basel, Switzerland) 23, 3165.
Boettiger, A.N., Bintu, B., Moffitt, J.R., Wang, S., Beliveau, B.J., Fudenberg, G., Imakaev, M., Mirny, L.A., Wu, C.-t., and Zhuang, X. (2016). Super-resolution imaging reveals distinct chromatin folding for different epigenetic states. Nature 529, 418.
Bouchet-Marquis, C., Dubochet, J., and Fakan, S. (2006). Cryoelectron microscopy of vitrified sections: a new challenge for the analysis of functional nuclear architecture. Histochemistry and cell biology 125, 43-51.
Boveri, T. (1909). Die Blastomerenkerne von Ascaris megalocephala und die Theorie der Chromosomenindividualitat. Archiv fur Zellforschung 3, 181-268.
Bowman, E.A., and Kelly, W.G. (2014). RNA polymerase II transcription elongation and Pol II CTD Ser2 phosphorylation: A tail of two kinases. Nucleus (Austin, Tex.) 5, 224-236.
Brill, S.J., DiNardo, S., Voelkel-Meiman, K., and Sternglanz, R. (1987). Need for DNA topoisomerase activity as a swivel for DNA replication for transcription of ribosomal RNA. Nature 326, 414-416.
Buschbeck, M., and Hake, S.B. (2017). Variants of core histones and their roles in cell fate decisions, development and cancer. Nature Reviews Molecular Cell Biology 18, 299.

Champoux, J.J. (2001). DNA topoisomerases: structure, function, and mechanism. Annual review of biochemistry 70, 369-413.
Chen, B., Zou, W., and Huang, B. (2018). CRISPR-Tag: an Efficient DNA Tagging System in Living Cells. bioRxiv.
Chen, D., and Jin, C. (2017). Histone variants in environmental-stress-induced DNA damage repair. Mutation Research/Reviews in Mutation Research.
Chen, P., Zhao, J., and Li, G. (2013). Histone variants in development and diseases. Journal of genetics and genomics = Yi chuan xue bao 40, 355-365.
Cho, W.-K., Jayanth, N., English, B.P., Inoue, T., Andrews, J.O., Conway, W., Grimm, J.B., Spille, J.-H., Lavis, L.D., Lionnet, T., et al. (2016). RNA Polymerase II cluster dynamics predict mRNA output in living cells. eLife 5, e13617.
Cho, W.K., Spille, J.H., Hecht, M., Lee, C., Li, C., Grube, V., and Cisse, II (2018). Mediator and RNA polymerase II clusters associate in transcription-dependent condensates. Science 361, 412-415.
Cisse, II, Izeddin, I., Causse, S.Z., Boudarene, L., Senecal, A., Muresan, L., Dugast-Darzacq, C., Hajj, B., Dahan, M., and Darzacq, X. (2013). Real-time dynamics of RNA polymerase II clustering in live human cells. Science 341, 664-667.
Collepardo-Guevara, R., Portella, G., Vendruscolo, M., Frenkel, D., Schlick, T., and Orozco, M. (2015). Chromatin Unfolding by Epigenetic Modifications Explained by Dramatic Impairment of Internucleosome Interactions: A Multiscale Computational Study. Journal of the American Chemical Society 137, 10205-10215.
Coltharp, C., Kessler, R.P., and Xiao, J. (2012). Accurate construction of photoactivated localization microscopy (PALM) images for quantitative measurements. PLoS One 7, e51725.
Cook, P.R. (1999). The organization of replication and transcription. Science 284, 1790-1795.
Cook, P.R., and Marenduzzo, D. (2018). Transcription-driven genome organization: a model for chromosome structure and the regulation of gene expression tested through simulations. Nucleic Acids Research 46, 9895-9906.

Coons, A.H., and Kaplan, M.H. (1950). Localization of antigen in tissue cells; improvements in a method for the detection of antigen by means of fluorescent antibody. The Journal of experimental medicine 91, 1-13.
Cramer, P., Bushnell, D.A., Fu, J., Gnatt, A.L., Maier-Davis, B., Thompson, N.E., Burgess, R.R., Edwards, A.M., David, P.R., and Kornberg, R.D. (2000). Architecture of RNA polymerase II and implications for the transcription mechanism. Science 288, 640-649.
Cramer, P., Bushnell, D.A., and Kornberg, R.D. (2001). Structural basis of transcription: RNA polymerase II at 2.8 angstrom resolution. Science 292, 1863-1876.
Cremer, T., and Cremer, M. (2010). Chromosome territories. Cold Spring Harb Perspect Biol 2, a003889.
Darzacq, X., Shav-Tal, Y., de Turris, V., Brody, Y., Shenoy, S.M., Phair, R.D., and Singer, R.H. (2007). In vivo dynamics of RNA polymerase II transcription. Nature structural & molecular biology 14, 796-806.
Dekker, J., and Mirny, L. (2016). The 3D Genome as Moderator of Chromosomal Communication. Cell 164, 1110-1121.
Dekker, J., Rippe, K., Dekker, M., and Kleckner, N. (2002). Capturing Chromosome Conformation. Science 295, 1306-1311.
Dempsey, G.T., Vaughan, J.C., Chen, K.H., Bates, M., and Zhuang, X. (2011). Evaluation of fluorophores for optimal performance in localization-based super-resolution imaging. Nature methods 8, 1027-1036.
Denk, W., Strickler, J.H., and Webb, W.W. (1990). Two-photon laser scanning fluorescence microscopy. Science 248, 73-76.
Dertinger, T., Colyer, R., Iyer, G., Weiss, S., and Enderlein, J. (2009). Fast, background-free, 3D super-resolution optical fluctuation imaging (SOFI). Proceedings of the National Academy of Sciences 106, 22287-22292.
Dixon, J.R., Selvaraj, S., Yue, F., Kim, A., Li, Y., Shen, Y., Hu, M., Liu, J.S., and Ren, B. (2012). Topological domains in mammalian genomes identified by analysis of chromatin interactions. Nature 485, 376-380.
Doksani, Y., Wu, J.Y., de Lange, T., and Zhuang, X. (2013). Super-resolution fluorescence imaging of telomeres

reveals TRF2-dependent T-loop formation. Cell 155, 345-356.
Du, Z., Zheng, H., Huang, B., Ma, R., Wu, J., Zhang, X., He, J., Xiang, Y., Wang, Q., and Li, Y. (2017). Allelic reprogramming of 3D chromatin architecture during early mammalian development. Nature 547, 232.
Dubochet, J., Adrian, M., Chang, J.-J., Homo, J.-C., Lepault, J., McDowall, A.W., and Schultz, P. (2009). Cryo-electron microscopy of vitrified specimens. Quarterly Reviews of Biophysics 21, 129-228.
Eberharter, A., and Becker, P.B. (2002). Histone acetylation: a switch between repressive and permissive chromatin: Second in review series on chromatin dynamics. EMBO Reports 3, 224-229.
Egloff, S., and Murphy, S. (2008). Cracking the RNA polymerase II CTD code. Trends in genetics : TIG 24, 280-288.
Eltsov, M., Maclellan, K.M., Maeshima, K., Frangakis, A.S., and Dubochet, J. (2008). Analysis of cryo-electron microscopy images does not support the existence of 30-nm chromatin fibers in mitotic chromosomes in situ. Proceedings of the National Academy of Sciences of the United States of America 105, 19732-19737.
Endesfelder, U., Finan, K., Holden, S.J., Cook, P.R., Kapanidis, A.N., and Heilemann, M. (2013). Multiscale spatial organization of RNA polymerase in Escherichia coli. Biophysical journal 105, 172-181.
Eskiw, C.H., Rapp, A., Carter, D.R.F., and Cook, P.R. (2008). RNA polymerase II activity is located on the surface of protein-rich transcription factories. Journal of cell science 121, 1999.
Fang, K., Chen, X., Li, X., Shen, Y., Sun, J., Czajkowsky, D.M., and Shao, Z. (2018). Super-resolution Imaging of Individual Human Subchromosomal Regions in Situ Reveals Nanoscopic Building Blocks of Higher-Order Structure. ACS Nano 12, 4909-4918.
Faro-Trindade, I., and Cook, P.R. (2006). A conserved organization of transcription during embryonic stem cell differentiation and in cells with high C value. Molecular biology of the cell 17, 2910-2920.

Finch, J.T., and Klug, A. (1976). Solenoidal model for superstructure in chromatin. Proceedings of the National Academy of Sciences of the United States of America 73, 1897-1901.

Folling, J., Bossi, M., Bock, H., Medda, R., Wurm, C.A., Hein, B., Jakobs, S., Eggeling, C., and Hell, S.W. (2008). Fluorescence nanoscopy by ground-state depletion and single-molecule return. Nature methods 5, 943-945.

Galbraith, C.G., and Galbraith, J.A. (2011). Super-resolution microscopy at a glance. Journal of cell science 124, 1607-1611.

Gavrilov, A.A., Philonenko, E.S., Zukher, I.S., Iarovaia, O.V., and Razin, S.V. (2010). Mapping of the nuclear matrix-bound chromatin hubs by a new M3C experimental procedure. Nucleic Acids Research 38, 8051-8060.

Geisler, C., Hotz, T., Schönle, A., Hell, S.W., Munk, A., and Egner, A. (2012). Drift estimation for single marker switching based imaging schemes. Optics express 20, 7274-7289.

Georgieva, M., Cattoni, D.I., Fiche, J.B., Mutin, T., Chamousset, D., and Nollmann, M. (2016). Nanometer resolved single-molecule colocalization of nuclear factors by two-color super resolution microscopy imaging. Methods (San Diego, Calif.) 105, 44-55.

Gerasimova, N.S., Pestov, N.A., Kulaeva, O.I., Clark, D.J., and Studitsky, V.M. (2016). Transcription-induced DNA supercoiling: New roles of intranucleosomal DNA loops in DNA repair and transcription. Transcription 7, 91-95.

Ginsburg, D.S., Govind, C.K., and Hinnebusch, A.G. (2009). NuA4 lysine acetyltransferase Esa1 is targeted to coding regions and stimulates transcription elongation with Gcn5. Molecular and cellular biology 29, 6473-6487.

Görisch, S.M., Wachsmuth, M., Tóth, K.F., Lichter, P., and Rippe, K. (2005). Histone acetylation increases chromatin accessibility. Journal of cell science 118, 5825-5834.

Govind, C.K., Zhang, F., Qiu, H., Hofmeyer, K., and Hinnebusch, A.G. (2007). Gcn5 promotes acetylation, eviction, and methylation of nucleosomes in transcribed coding regions. Mol Cell 25, 31-42.

Gustafsson, M.G. (2000). Surpassing the lateral resolution limit by a factor of two using structured illumination microscopy. Journal of microscopy 198, 82-87.

Gustafsson, M.G., Shao, L., Carlton, P.M., Wang, C.J., Golubovskaya, I.N., Cande, W.Z., Agard, D.A., and Sedat, J.W. (2008). Three-dimensional resolution doubling in wide-field fluorescence microscopy by structured illumination. Biophysical journal 94, 4957-4970.

Hanafi, D.E., and Bossi, L. (2000). Activation and silencing of leu-500 promoter by transcription-induced DNA supercoiling in the Salmonella chromosome. Molecular Microbiology 37, 583-594.

Hanaichi, T., Sato, T., Iwamoto, T., Malavasi-Yamashiro, J., Hoshino, M., and Mizuno, N. (1986). A stable lead by modification of Sato's method. Journal of electron microscopy 35, 304-306.

Heilemann, M., Margeat, E., Kasper, R., Sauer, M., and Tinnefeld, P. (2005). Carbocyanine dyes as efficient reversible single-molecule optical switch. Journal of the American Chemical Society 127, 3801-3806.

Heilemann, M., van de Linde, S., Schüttpelz, M., Kasper, R., Seefeldt, B., Mukherjee, A., Tinnefeld, P., and Sauer, M. (2008). Subdiffraction-Resolution Fluorescence Imaging with Conventional Fluorescent Probes. Angewandte Chemie International Edition 47, 6172-6176.

Hein, C.D., Liu, X.-M., and Wang, D. (2008). Click chemistry, a powerful tool for pharmaceutical sciences. Pharmaceutical research 25, 2216-2230.

Heintzmann, R., and Cremer, C.G. (1999). Laterally modulated excitation microscopy: improvement of resolution by using a diffraction grating, Vol 3568 (SPIE).

Hell, S., and Stelzer, E.H.K. (1992). Fundamental improvement of resolution with a 4Pi-confocal fluorescence microscope using two-photon excitation. Optics Communications 93, 277-282.

Hell, S.W., and Wichmann, J. (1994). Breaking the diffraction resolution limit by stimulated emission: stimulated-emission-depletion fluorescence microscopy. Opt Lett 19, 780-782.

Henikoff, S., Furuyama, T., and Ahmad, K. (2004). Histone variants, nucleosome assembly and epigenetic inheritance. Trends in genetics : TIG 20, 320-326.
Hennig, B.J., Fielding, K., Broxholme, J., Diatta, M., Mendy, M., Moore, C., Pollard, A.J., Rayco-Solon, P., Sirugo, G., van der Sande, M.A., et al. (2008). Host genetic factors and vaccine-induced immunity to hepatitis B virus infection. PLoS One 3, e1898.
Hess, S.T., Girirajan, T.P., and Mason, M.D. (2006). Ultra-high resolution imaging by fluorescence photoactivation localization microscopy. Biophysical journal 91, 4258-4272.
Hirose, Y., and Manley, J.L. (1998). RNA polymerase II is an essential mRNA polyadenylation factor. Nature 395, 93-96.
Holstege, F.C., Fiedler, U., and Timmers, H.T. (1997). Three transitions in the RNA polymerase II transcription complex during initiation. Embo j 16, 7468-7480.
Huang, B., Jones, S.A., Brandenburg, B., and Zhuang, X. (2008). Whole-cell 3D STORM reveals interactions between cellular structures with nanometer-scale resolution. Nature methods 5, 1047-1052.
Hug, C.B., Grimaldi, A.G., Kruse, K., and Vaquerizas, J.M. (2017). Chromatin architecture emerges during zygotic genome activation independent of transcription. Cell 169, 216-228. e219.
Huisken, J., Swoger, J., Del Bene, F., Wittbrodt, J., and Stelzer, E.H. (2004). Optical sectioning deep inside live embryos by selective plane illumination microscopy. Science 305, 1007-1009.
Huxley, H.E., and Zubay, G. (1961). Preferential staining of nucleic acid-containing structures for electron microscopy. The Journal of biophysical and biochemical cytology 11, 273-296.
Iborra, F.J., Pombo, A., Jackson, D.A., and Cook, P.R. (1996). Active RNA polymerases are localized within discrete transcription "factories' in human nuclei. Journal of cell science 109 (Pt 6), 1427-1436.
Inoue, K., Oikawa, M., Kamimura, S., Ogonuki, N., Nakamura, T., Nakano, T., Abe, K., and Ogura, A. (2015). Trichostatin A specifically improves the aberrant

expression of transcription factor genes in embryos produced by somatic cell nuclear transfer. Scientific Reports 5, 10127.
Jackson, D.A., Hassan, A.B., Errington, R.J., and Cook, P.R. (1993). Visualization of focal sites of transcription within human nuclei. Embo j 12, 1059-1065.
Jackson, D.A., Iborra, F.J., Manders, E.M., and Cook, P.R. (1998). Numbers and organization of RNA polymerases, nascent transcripts, and transcription units in HeLa nuclei. Molecular biology of the cell 9, 1523-1536.
Jackson, D.A., and Pombo, A. (1998). Replicon clusters are stable units of chromosome structure: evidence that nuclear organization contributes to the efficient activation and propagation of S phase in human cells. J Cell Biol 140, 1285-1295.
Jao, C.Y., and Salic, A. (2008). Exploring RNA transcription and turnover in vivo by using click chemistry. Proceedings of the National Academy of Sciences of the United States of America 105, 15779-15784.
Jaworek, T., Richard, E., Ivanova, A., Giese, A., I Choo, D., N Khan, S., Riazuddin, S., Kahn, R., and Riazuddin, S. (2013). An Alteration in ELMOD3, an Arl2 GTPase-Activating Protein, Is Associated with Hearing Impairment in Humans, Vol 9.
Jenuwein, T., and Allis, C.D. (2001). Translating the histone code. Science 293, 1074-1080.
Jonkers, I., and Lis, J.T. (2015). Getting up to speed with transcription elongation by RNA polymerase II. Nature reviews. Molecular cell biology 16, 167-177.
Joti, Y., Hikima, T., Nishino, Y., Kamada, F., Hihara, S., Takata, H., Ishikawa, T., and Maeshima, K. (2012). Chromosomes without a 30-nm chromatin fiber. Nucleus (Austin, Tex.) 3, 404-410.
Jungmann, R., Avendano, M.S., Woehrstein, J.B., Dai, M., Shih, W.M., and Yin, P. (2014). Multiplexed 3D cellular super-resolution imaging with DNA-PAINT and Exchange-PAINT. Nature methods 11, 313-318.
Jungmann, R., Steinhauer, C., Scheible, M., Kuzyk, A., Tinnefeld, P., and Simmel, F.C. (2010). Single-molecule kinetics and super-resolution microscopy by fluorescence

imaging of transient binding on DNA origami. Nano letters 10, 4756-4761.
Ke, Y., Xu, Y., Chen, X., Feng, S., Liu, Z., Sun, Y., Yao, X., Li, F., Zhu, W., and Gao, L. (2017). 3D chromatin structures of mature gametes and structural reprogramming during mammalian embryogenesis. Cell 170, 367-381. e320.
Keogh, M.C., Kurdistani, S.K., Morris, S.A., Ahn, S.H., Podolny, V., Collins, S.R., Schuldiner, M., Chin, K., Punna, T., Thompson, N.J., et al. (2005). Cotranscriptional set2 methylation of histone H3 lysine 36 recruits a repressive Rpd3 complex. Cell 123, 593-605.
Kimura, H., Sugaya, K., and Cook, P.R. (2002). The transcription cycle of RNA polymerase II in living cells. J Cell Biol 159, 777-782.
Kireeva, M.L., Walter, W., Tchernajenko, V., Bondarenko, V., Kashlev, M., and Studitsky, V.M. (2002). Nucleosome remodeling induced by RNA polymerase II: loss of the H2A/H2B dimer during transcription. Mol Cell 9, 541-552.
Klar, T.A., and Hell, S.W. (1999). Subdiffraction resolution in far-field fluorescence microscopy. Opt. Lett. 24, 954-956.
Klar, T.A., Jakobs, S., Dyba, M., Egner, A., and Hell, S.W. (2000). Fluorescence microscopy with diffraction resolution barrier broken by stimulated emission. Proceedings of the National Academy of Sciences of the United States of America 97, 8206-8210.
Kolb, H.C., Finn, M., and Sharpless, K.B. (2001). Click chemistry: diverse chemical function from a few good reactions. Angewandte Chemie International Edition 40, 2004-2021.
Kornberg, R.D. (1974). Chromatin structure: a repeating unit of histones and DNA. Science 184, 868-871.
Kraus, F., Miron, E., Demmerle, J., Chitiashvili, T., Budco, A., Alle, Q., Matsuda, A., Leonhardt, H., Schermelleh, L., and Markaki, Y. (2017). Quantitative 3D structured illumination microscopy of nuclear structures. Nat Protoc 12, 1011-1028.
Kulaeva, O.I., Gaykalova, D.A., Pestov, N.A., Golovastov, V.V., Vassylyev, D.G., Artsimovitch, I., and Studitsky, V.M. (2009). Mechanism of chromatin remodeling and recovery during passage of RNA polymerase II. Nature Structural &Amp; Molecular Biology 16, 1272.

Kumaran, R.I., and Spector, D.L. (2008). A genetic locus targeted to the nuclear periphery in living cells maintains its transcriptional competence. The Journal of cell biology 180, 51-65.

Kuzmichev, A., Nishioka, K., Erdjument-Bromage, H., Tempst, P., and Reinberg, D. (2002). Histone methyltransferase activity associated with a human multiprotein complex containing the Enhancer of Zeste protein. Genes & development 16, 2893-2905.

Ladépêche, L., Planagumà, J., Thakur, S., Suárez, I., Hara, M., Borbely, J.S., Sandoval, A., Laparra-Cuervo, L., Dalmau, J., and Lakadamyali, M. (2018). NMDA Receptor Autoantibodies in Autoimmune Encephalitis Cause a Subunit-Specific Nanoscale Redistribution of NMDA Receptors. Cell reports 23, 3759-3768.

Langer, D., Hain, J., Thuriaux, P., and Zillig, W. (1995). Transcription in archaea: similarity to that in eucarya. Proceedings of the National Academy of Sciences of the United States of America 92, 5768-5772.

Larkin, J.D., Papantonis, A., Cook, P.R., and Marenduzzo, D. (2013). Space exploration by the promoter of a long human gene during one transcription cycle. Nucleic acids research 41, 2216-2227.

Lee, S.H., Baday, M., Tjioe, M., Simonson, P.D., Zhang, R., Cai, E., and Selvin, P.R. (2012). Using fixed fiduciary markers for stage drift correction. Optics express 20, 12177-12183.

Legant, W.R., Shao, L., Grimm, J.B., Brown, T.A., Milkie, D.E., Avants, B.B., Lavis, L.D., and Betzig, E. (2016). High-density three-dimensional localization microscopy across large volumes. Nature methods 13, 359-365.

Lemmer, P., Gunkel, M., Baddeley, D., Kaufmann, R., Urich, A., Weiland, Y., Reymann, J., Müller, P., Hausmann, M., and Cremer, C. (2008). SPDM: light microscopy with single-molecule resolution at the nanoscale. Applied Physics B 93, 1.

Levet, F., Hosy, E., Kechkar, A., Butler, C., Beghin, A., Choquet, D., and Sibarita, J.B. (2015). SR-Tesseler: a method to segment and quantify localization-based super-resolution microscopy data. Nature methods 12, 1065-1071.

Li, B., Carey, M., and Workman, J.L. (2007). The Role of Chromatin during Transcription. Cell 128, 707-719.
Lieberman-Aiden, E., van Berkum, N.L., Williams, L., Imakaev, M., Ragoczy, T., Telling, A., Amit, I., Lajoie, B.R., Sabo, P.J., Dorschner, M.O., et al. (2009). Comprehensive Mapping of Long-Range Interactions Reveals Folding Principles of the Human Genome. Science 326, 289-293.
Liu, J., Lin, D., Yardımcı, G.G., and Noble, W.S. (2018). Unsupervised embedding of single-cell Hi-C data. Bioinformatics 34, i96-i104.
Lopez-Atalaya, J., Ito, S., Valor, L., Benito-Garagorri, E., and Barco, A. (2013). Genomic targets, and histone acetylation and gene expression profiling of neural HDAC inhibition, Vol 41.
Luger, K., Mader, A.W., Richmond, R.K., Sargent, D.F., and Richmond, T.J. (1997). Crystal structure of the nucleosome core particle at 2.8 A resolution. Nature 389, 251-260.
Luse, D.S., and Jacob, G.A. (1987). Abortive initiation by RNA polymerase II in vitro at the adenovirus 2 major late promoter. The Journal of biological chemistry 262, 14990-14997.
Ma, J., and Wang, M. (2014). Interplay between DNA supercoiling and transcription elongation. Transcription 5, e28636.
Maeshima, K., Hihara, S., and Eltsov, M. (2010). Chromatin structure: does the 30-nm fibre exist in vivo? Curr Opin Cell Biol 22, 291-297.
Maeshima, K., Imai, R., Tamura, S., and Nozaki, T. (2014). Chromatin as dynamic 10-nm fibers. Chromosoma 123, 225-237.
McDowall, A.W., Smith, J.M., and Dubochet, J. (1986). Cryo-electron microscopy of vitrified chromosomes in situ. The EMBO journal 5, 1395-1402.
McKinney, S.A., Murphy, C.S., Hazelwood, K.L., Davidson, M.W., and Looger, L.L. (2009). A bright and photostable photoconvertible fluorescent protein. Nature methods 6, 131-133.
Mejias-Luque, R., Peiro, S., Vincent, A., Van Seuningen, I., and de Bolos, C. (2008). IL-6 induces MUC4 expression

through gp130/STAT3 pathway in gastric cancer cell lines. Biochim Biophys Acta 1783, 1728-1736.
Miller, O.L., Jr., and Beatty, B.R. (1969). Visualization of nucleolar genes. Science 164, 955-957.
Mitchell-Jordan, S., Chen, H., Franklin, S., Stefani, E., Bentolila, L.A., and Vondriska, T.M. (2012). Features of endogenous cardiomyocyte chromatin revealed by super-resolution STED microscopy. Journal of Molecular and Cellular Cardiology 53, 552-558.
Mlodzianoski, M.J., Schreiner, J.M., Callahan, S.P., Smolková, K., Dlasková, A., Šantorová, J., Ježek, P., and Bewersdorf, J. (2011). Sample drift correction in 3D fluorescence photoactivation localization microscopy. Optics express 19, 15009-15019.
Moerner, W.E., and Kador, L. (1989). Optical detection and spectroscopy of single molecules in a solid. Physical Review Letters 62, 2535-2538.
Moore, P.S., Barbi, S., Donadelli, M., Costanzo, C., Bassi, C., Palmieri, M., and Scarpa, A. (2004). Gene expression profiling after treatment with the histone deacetylase inhibitor trichostatin A reveals altered expression of both pro- and anti-apoptotic genes in pancreatic adenocarcinoma cells. Biochimica et Biophysica Acta (BBA) - Molecular Cell Research 1693, 167-176.
Nakayama, J., Rice, J.C., Strahl, B.D., Allis, C.D., and Grewal, S.I. (2001). Role of histone H3 lysine 9 methylation in epigenetic control of heterochromatin assembly. Science 292, 110-113.
Neguembor, M.V., Sebastian-Perez, R., Aulicino, F., Gomez-Garcia, P.A., Cosma, M.P., and Lakadamyali, M. (2018). (Po)STAC (Polycistronic SunTAg modified CRISPR) enables live-cell and fixed-cell super-resolution imaging of multiple genes. Nucleic acids research 46, e30-e30.
Nir, G., Farabella, I., Pérez Estrada, C., Ebeling, C.G., Beliveau, B.J., Sasaki, H.M., Lee, S.D., Nguyen, S.C., McCole, R.B., Chattoraj, S., et al. (2018). Walking along chromosomes with super-resolution imaging, contact maps, and integrative modeling. PLOS Genetics 14, e1007872.
Nishino, Y., Eltsov, M., Joti, Y., Ito, K., Takata, H., Takahashi, Y., Hihara, S., Frangakis, A.S., Imamoto, N., Ishikawa, T.,

et al. (2012). Human mitotic chromosomes consist predominantly of irregularly folded nucleosome fibres without a 30-nm chromatin structure. EMBO J 31, 1644-1653.
Nora, E.P., Lajoie, B.R., Schulz, E.G., Giorgetti, L., Okamoto, I., Servant, N., Piolot, T., van Berkum, N.L., Meisig, J., Sedat, J., et al. (2012). Spatial partitioning of the regulatory landscape of the X-inactivation centre. Nature 485, 381-385.
Oddone, A., Vilanova, I.V., Tam, J., and Lakadamyali, M. (2014). Super-resolution imaging with stochastic single-molecule localization: Concepts, technical developments, and biological applications. Microscopy Research and Technique 77, 502-509.
Olins, A.L., Moyer, B.A., Kim, S.H., and Allison, D.P. (1989). Synthesis of a more stable osmium ammine electron-dense DNA stain. The journal of histochemistry and cytochemistry : official journal of the Histochemistry Society 37, 395-398.
Olivier, N., Keller, D., Rajan, V.S., Gönczy, P., and Manley, S. (2013). Simple buffers for 3D STORM microscopy. Biomed. Opt. Express 4, 885-899.
Osborne, C.S., Chakalova, L., Brown, K.E., Carter, D., Horton, A., Debrand, E., Goyenechea, B., Mitchell, J.A., Lopes, S., Reik, W., et al. (2004). Active genes dynamically colocalize to shared sites of ongoing transcription. Nature genetics 36, 1065-1071.
Ou, H.D., Phan, S., Deerinck, T.J., Thor, A., Ellisman, M.H., and O'Shea, C.C. (2017). ChromEMT: Visualizing 3D chromatin structure and compaction in interphase and mitotic cells. Science (New York, N.Y.) 357, eaag0025.
P Hergeth, S., and Schneider, R. (2015). The H1 linker histones: Multifunctional proteins beyond the nucleosomal core particle, Vol 16.
Papantonis, A., and Cook, P.R. (2011). Fixing the model for transcription: the DNA moves, not the polymerase. Transcription 2, 41-44.
Papantonis, A., and Cook, P.R. (2013). Transcription Factories: Genome Organization and Gene Regulation. Chemical Reviews 113, 8683-8705.

Papantonis, A., Larkin, J.D., Wada, Y., Ohta, Y., Ihara, S., Kodama, T., and Cook, P.R. (2010). Active RNA polymerases: mobile or immobile molecular machines? PLoS biology 8, e1000419.

Patterson, G.H., and Lippincott-Schwartz, J. (2002). A photoactivatable GFP for selective photolabeling of proteins and cells. Science 297, 1873-1877.

Pombo, A., Jackson, D.A., Hollinshead, M., Wang, Z., Roeder, R.G., and Cook, P.R. (1999). Regional specialization in human nuclei: visualization of discrete sites of transcription by RNA polymerase III. Embo j 18, 2241-2253.

Qu, D., Wang, G., Wang, Z., Zhou, L., Chi, W., Cong, S., Ren, X., Liang, P., and Zhang, B. (2011). 5-Ethynyl-2'-deoxycytidine as a new agent for DNA labeling: detection of proliferating cells. Analytical biochemistry 417, 112-121.

Rabl, C. (1885). Über Zellteilung//Morphologisches Jahrbuch. B 10, 214-330.

Racko, D., Benedetti, F., Dorier, J., and Stasiak, A. (2018). Transcription-induced supercoiling as the driving force of chromatin loop extrusion during formation of TADs in interphase chromosomes. Nucleic acids research 46, 1648-1660.

Reddy, K.L., Zullo, J.M., Bertolino, E., and Singh, H. (2008). Transcriptional repression mediated by repositioning of genes to the nuclear lamina. Nature 452, 243-247.

Ricci, Maria A., Manzo, C., García-Parajo, M.F., Lakadamyali, M., and Cosma, Maria P. (2015). Chromatin Fibers Are Formed by Heterogeneous Groups of Nucleosomes In Vivo. Cell 160, 1145-1158.

Roth, S.Y., Denu, J.M., and Allis, C.D. (2001). Histone acetyltransferases. Annual review of biochemistry 70, 81-120.

Rothbart, S.B., and Strahl, B.D. (2014). Interpreting the language of histone and DNA modifications. Biochimica et Biophysica Acta (BBA) - Gene Regulatory Mechanisms 1839, 627-643.

Rowley, M.J., and Corces, V.G. (2018). Organizational principles of 3D genome architecture. Nature reviews. Genetics.

Rowley, M.J., Nichols, M.H., Lyu, X., Ando-Kuri, M., Rivera, I.S.M., Hermetz, K., Wang, P., Ruan, Y., and Corces, V.G. (2017). Evolutionarily Conserved Principles Predict 3D Chromatin Organization. Mol Cell 67, 837-852 e837.

Rust, M.J., Bates, M., and Zhuang, X. (2006). Sub-diffraction-limit imaging by stochastic optical reconstruction microscopy (STORM). Nature methods 3, 793-795.

Sarai, N., Nimura, K., Tamura, T., Kanno, T., Patel, M.C., Heightman, T.D., Ura, K., and Ozato, K. (2013). WHSC1 links transcription elongation to HIRA-mediated histone H3.3 deposition. Embo j 32, 2392-2406.

Schermelleh, L., Carlton, P.M., Haase, S., Shao, L., Winoto, L., Kner, P., Burke, B., Cardoso, M.C., Agard, D.A., Gustafsson, M.G.L., et al. (2008). Subdiffraction Multicolor Imaging of the Nuclear Periphery with 3D Structured Illumination Microscopy. Science 320, 1332-1336.

Schermelleh, L., Heintzmann, R., and Leonhardt, H. (2010). A Guide to Super-Resolution Fluorescence Microscopy, Vol 190.

Schnitzbauer, J., Strauss, M.T., Schlichthaerle, T., Schueder, F., and Jungmann, R. (2017). Super-resolution microscopy with DNA-PAINT. Nature Protocols 12, 1198.

Schueder, F., Lara-Gutiérrez, J., Beliveau, B.J., Saka, S.K., Sasaki, H.M., Woehrstein, J.B., Strauss, M.T., Grabmayr, H., Yin, P., and Jungmann, R. (2017). Multiplexed 3D super-resolution imaging of whole cells using spinning disk confocal microscopy and DNA-PAINT. Nature Communications 8, 2090.

Sexton, T., and Cavalli, G. (2015). The role of chromosome domains in shaping the functional genome. Cell 160, 1049-1059.

Shannon, C.E., and Weaver, W. (1949). The mathematical theory of information.

Sharonov, A., and Hochstrasser, R.M. (2006). Wide-field subdiffraction imaging by accumulated binding of diffusing probes. Proceedings of the National Academy of Sciences 103, 18911-18916.

Sigal, Y.M., Speer, C.M., Babcock, H.P., and Zhuang, X. (2015). Mapping Synaptic Input Fields of Neurons with Super-Resolution Imaging. Cell 163, 493-505.

Simon, Jeffrey A., and Kingston, Robert E. (2013). Occupying Chromatin: Polycomb Mechanisms for Getting to Genomic Targets, Stopping Transcriptional Traffic, and Staying Put. Molecular Cell 49, 808-824.

Smale, S.T., and Kadonaga, J.T. (2003). The RNA polymerase II core promoter. Annual review of biochemistry 72, 449-479.

So, L.-H., Ghosh, A., Zong, C., Sepúlveda, L.A., Segev, R., and Golding, I. (2011). General properties of transcriptional time series in Escherichia coli. Nature genetics 43, 554-560.

Soeller, C., and Baddeley, D. (2013). Super-resolution imaging of EC coupling protein distribution in the heart. J Mol Cell Cardiol 58, 32-40.

Stigler, J., Çamdere, G.Ö., Koshland, D.E., and Greene, E.C. (2016). Single-Molecule Imaging Reveals a Collapsed Conformational State for DNA-Bound Cohesin. Cell reports 15, 988-998.

Strack, R. (2015). Death by super-resolution imaging. Nature methods 12, 1111.

Subach, F.V., Patterson, G.H., Manley, S., Gillette, J.M., Lippincott-Schwartz, J., and Verkhusha, V.V. (2009). Photoactivatable mCherry for high-resolution two-color fluorescence microscopy. Nature methods 6, 153-159.

Sunwoo, H., Wu, J.Y., and Lee, J.T. (2015). The Xist RNA-PRC2 complex at 20-nm resolution reveals a low Xist stoichiometry and suggests a hit-and-run mechanism in mouse cells. Proceedings of the National Academy of Sciences of the United States of America 112, E4216-E4225.

Szymborska, A., de Marco, A., Daigle, N., Cordes, V.C., Briggs, J.A.G., and Ellenberg, J. (2013). Nuclear Pore Scaffold Structure Analyzed by Super-Resolution Microscopy and Particle Averaging. Science 341, 655-658.

Tanenbaum, M.E., Gilbert, L.A., Qi, L.S., Weissman, J.S., and Vale, R.D. (2014). A protein-tagging system for signal amplification in gene expression and fluorescence imaging. Cell 159, 635-646.

Thoma, F., Koller, T., and Klug, A. (1979). Involvement of histone H1 in the organization of the nucleosome and of

the salt-dependent superstructures of chromatin. The Journal of Cell Biology 83, 403-427.
Thompson, R.E., Larson, D.R., and Webb, W.W. (2002). Precise nanometer localization analysis for individual fluorescent probes. Biophysical journal 82, 2775-2783.
Thurman, R.E., Rynes, E., Humbert, R., Vierstra, J., Maurano, M.T., Haugen, E., Sheffield, N.C., Stergachis, A.B., Wang, H., Vernot, B., et al. (2012). The accessible chromatin landscape of the human genome. Nature 489, 75-82.
Tokunaga, M., Imamoto, N., and Sakata-Sogawa, K. (2008). Highly inclined thin illumination enables clear single-molecule imaging in cells. Nature methods 5, 159.
Toth, K.F., Knoch, T.A., Wachsmuth, M., Frank-Stohr, M., Stohr, M., Bacher, C.P., Muller, G., and Rippe, K. (2004). Trichostatin A-induced histone acetylation causes decondensation of interphase chromatin. Journal of cell science 117, 4277-4287.
Verdone, L., Caserta, M., and Di Mauro, E. (2005). Role of histone acetylation in the control of gene expression. Biochem Cell Biol 83, 344-353.
Voronoi, G. (1908). Nouvelles applications des paramètres continus à la théorie des formes quadratiques. Premier mémoire. Sur quelques propriétés des formes quadratiques positives parfaites. Journal für die reine und angewandte Mathematik 133, 178.
Wäldchen, S., Lehmann, J., Klein, T., van de Linde, S., and Sauer, M. (2015). Light-induced cell damage in live-cell super-resolution microscopy. Scientific Reports 5, 15348.
Wang, S., Su, J.H., Beliveau, B.J., Bintu, B., Moffitt, J.R., Wu, C.T., and Zhuang, X. (2016). Spatial organization of chromatin domains and compartments in single chromosomes. Science 353, 598-602.
Wang, Y., Schnitzbauer, J., Hu, Z., Li, X., Cheng, Y., Huang, Z.-L., and Huang, B. (2014). Localization events-based sample drift correction for localization microscopy with redundant cross-correlation algorithm. Optics express 22, 15982-15991.
Wansink, D.G., Schul, W., van der Kraan, I., van Steensel, B., van Driel, R., and de Jong, L. (1993). Fluorescent labeling of nascent RNA reveals transcription by RNA polymerase

II in domains scattered throughout the nucleus. J Cell Biol 122, 283-293.
Watson, M.L. (1958). Staining of tissue sections for electron microscopy with heavy metals. II. Application of solutions containing lead and barium. The Journal of biophysical and biochemical cytology 4, 727-730.
Weng, X., and Xiao, J. (2014). Spatial organization of transcription in bacterial cells. Trends in genetics : TIG 30, 287-297.
Wiedenmann, J., Ivanchenko, S., Oswald, F., Schmitt, F., Rocker, C., Salih, A., Spindler, K.D., and Nienhaus, G.U. (2004). EosFP, a fluorescent marker protein with UV-inducible green-to-red fluorescence conversion. Proceedings of the National Academy of Sciences of the United States of America 101, 15905-15910.
Wiles, E.T., and Selker, E.U. (2017). H3K27 methylation: a promiscuous repressive chromatin mark. Current opinion in genetics & development 43, 31-37.
Wittschieben, B.O., Otero, G., de Bizemont, T., Fellows, J., Erdjument-Bromage, H., Ohba, R., Li, Y., Allis, C.D., Tempst, P., and Svejstrup, J.Q. (1999). A novel histone acetyltransferase is an integral subunit of elongating RNA polymerase II holoenzyme. Mol Cell 4, 123-128.
Wolffe, A.P., and Hayes, J.J. (1999). Chromatin disruption and modification. Nucleic acids research 27, 711-720.
Xu, J., Ma, H., Jin, J., Uttam, S., Fu, R., Huang, Y., and Liu, Y. (2018). Super-Resolution Imaging of Higher-Order Chromatin Structures at Different Epigenomic States in Single Mammalian Cells. Cell Rep 24, 873-882.
Xu, K., Zhong, G., and Zhuang, X. (2013). Actin, spectrin, and associated proteins form a periodic cytoskeletal structure in axons. Science 339, 452-456.
Yildiz, A., Park, H., Safer, D., Yang, Z., Chen, L.Q., Selvin, P.R., and Sweeney, H.L. (2004). Myosin VI steps via a hand-over-hand mechanism with its lever arm undergoing fluctuations when attached to actin. The Journal of biological chemistry 279, 37223-37226.
Zadegan, R.M., and Norton, M.L. (2012). Structural DNA nanotechnology: from design to applications. International journal of molecular sciences 13, 7149-7162.

Zhang, J., Carver, C.M., Choveau, F.S., and Shapiro, M.S. (2016). Clustering and Functional Coupling of Diverse Ion Channels and Signaling Proteins Revealed by Super-resolution STORM Microscopy in Neurons. Neuron 92, 461-478.

Zhang, M., Chang, H., Zhang, Y., Yu, J., Wu, L., Ji, W., Chen, J., Liu, B., Lu, J., Liu, Y., et al. (2012). Rational design of true monomeric and bright photoactivatable fluorescent proteins. Nature methods 9, 727-729.

Zhang, Z., Nishimura, Y., and Kanchanawong, P. (2017). Extracting microtubule networks from superresolution single-molecule localization microscopy data. Molecular biology of the cell 28, 333-345.

Zhao, Z.W., Roy, R., Gebhardt, J.C.M., Suter, D.M., Chapman, A.R., and Xie, X.S. (2014). Spatial organization of RNA polymerase II inside a mammalian cell nucleus revealed by reflected light-sheet superresolution microscopy. Proceedings of the National Academy of Sciences of the United States of America 111, 681-686.

Zhou, Q., Li, T., and Price, D.H. (2012). RNA polymerase II elongation control. Annual review of biochemistry 81, 119-143.

Zillig, W., Stetter, K.O., and Tobien, M. (1978). DNA-dependent RNA polymerase from Halobacterium halobium. European journal of biochemistry 91, 193-199.

Annex I: Abbreviation index

A647: Alexa 647
CDF: Cumulative Density Fraction
CTD: Carboxy Terminal Domain
EdC: Ethynyl-2'-deoxycytidine
EU: Ethynyl-Uridine
GLOX: Enzymatic mix composed of Glucose Oxidase + Catalase
HAT: Histone Acetylase
HDAC: Histone Deacetylase
hFB: human Fibroblasts
IL-6: Interleukine 6
MEA: Mercaptoethylamine
NND: Nearest Neighbor Distance
PAINT: Point Accumulation for Imaging in Nanoscale Topography
PALM: Photo-Activated Localization Microscopy
PSF: Point Spread Function
SIM: Structured Illumination Microscopy
SMLM: Single Molecule Localization Microscopy
STAC: SunTAg Modified CRISPR
STED: STimulated Emission Depletion microscopy
STORM: STochastic Optical Reconstruction Microscopy
TSA: Trychostatin-A